DYNAMICS & MAMMATUS CLOUDS IN THE ANVIL OUTFLOW OF DEEP CONVECTION OVER THE TIWI ISLANDS

SHAYA HOWARD

A THESIS SUBMITTED TO THE FACULTY OF GRADUATE STUDIES IN PARTIAL FULFILLMENT OF THE REQUIREMENTS FOR THE DEGREE OF

MASTER OF SCIENCE

GRADUATE PROGRAM IN EARTH AND SPACE SCIENCE

YORK UNIVERSITY

TORONTO, ONTARIO

May, 2022

Abstract

The research that is presented in this thesis is based on data that comes from the EMERALD-2 research campaign. The Egrett and the King Air were the research planes that were used to conduct measurements during the project. EMERALD-2 focused on "Hector" which is a convective system that occurs regularly over the Tiwi Islands just off the coast of Darwin, Northern Territory, Australia. On December 2nd, 2002 mammatus clouds developed on the base of the anvil outflow cirrus clouds produced by the "Hector" thunderstorm. The Egrett carried instruments that measured temperature, pressure, wind velocity and moisture. The King Air flew underneath the Egrett and a LIDAR aboard the plane was used to collect data on the cloud structure. This information was used to analyze the dynamical features and the state of the atmosphere in the anvil outflow of the thunderstorm. The objective was to identify a possible formation mechanism for the mammatus clouds.

It was found that the dynamics in the anvil outflow region included a mixture of isotropic turbulence and coherent structures. The turbulence was considered to be light, according to the dissipation rate values that were observed. Shear instability and convective instability were present in the anvil outflow region; these conditions both lead to the development of turbulence. Some gravity waves in the anvil outflow are breaking; these waves will eventually overturn and break down into turbulence. Kelvin-Helmholtz waves are likely to develop in an environment with shear instability, these waves can break and dissipate into turbulence.

Atmospheric conditions were favourable for cloud base detrainment instability to cause the formation of mammatus clouds. In the vicinity of the anvil cloud base, moist and potentially cold air was sitting on top of dry and potentially warm air. Liquid water static energy decreases with increasing altitude at the base of the anvil cloud; this condition is considered to be quantitative evidence of cloud base detrainment instability. Turbulence can cause dry air to be mixed into the anvil cloud. The mixed air parcel cools as latent heat is transferred from air molecules to the sublimating hydrometeors. The cloudy air parcels sink and form the lobes that make up the mammatus clouds. The potential temperature gradient in the area of the cloud base is negative and this may cause another formation mechanism, cloudy air parcels that are colder than their surrounding environment will sink until they reach the level of neutral buoyancy. The sinking air parcels of cloudy air develop into the mammatus lobes that extend from the base of the anvil cloud.

Acknowledgements

I am very thankful for the help, guidance, and encouragement provided by my supervisor Professor Jim Whiteway. Thank you for helping me to stay on track through the COVID-19 lockdown and the learning curve I encountered while working from home. The work I have done over the last few years would not be possible without your patience and supervision.

I would also like to acknowledge Professor Neil Tandon, thank you for being on my exam committee and providing valuable feedback for the Research Evaluation Course and the final oral exam.

This journey would have been way more difficult if I did not have the love and support of my family at home. I am so thankful for my parents George and Grace, my brother Seyan, and my grandmother Lileth. All of the help and encouragement that I received at home allowed me to get more done than I ever could on my own.

Table of Contents

List of Tables

List of Figures

Chapter 1: Introduction

Deep convection can be described as buoyancy driven vertical motion that causes air parcels to move from the lower troposphere to the upper troposphere. The force of buoyancy is due to differences between the downward force of gravity and the upward pressure gradient force. It is directed upwards when a parcel of air has a greater temperature (lower density) than its environment. The opposite is true when an air parcel cools down and the density of the parcel increases. The force of gravity acting on the parcel increases and the parcel will sink once the force of gravity is larger than the pressure gradient force.

Deep convection begins when the sun warms the earth's surface, first the surface heats up and the surface begins to radiate infrared radiation into the atmosphere. There is also conduction occurring at the interface between the atmosphere and the surface. Eventually the atmosphere heats up and some air parcels become warmer (and less dense) than their environment and will move upwards. These air parcels expand and cool down until they reach the dewpoint temperature which is when water vapour inside of the air parcel condenses into water droplets. The air parcel now contains a cloud and the latent heat released as water condenses warms the air and buoyancy drives further upward motion until the parcel reaches the tropopause. The cloud now has an impressive vertical structure that appears like a large explosion, the cloud flattens out at the top where the air parcels are becoming neutrally buoyant with the environment and vertical motion stops. The large vertical cloud that developed is known as a cumulonimbus cloud, that is capable of producing heavy showers and thunderstorms.

In the case of a thunderstorm one cumulonimbus cloud usually consitutes one thunderstorm cell with an updraft of warm air and a downdraft of cool air that is associated with

precipitation, this is known as a single-cell thunderstorm. A thunderstorm that contains multiple cells (multiple updraft and downdraft regions) is a multi-cell thunderstorm. These thunderstorms develop whenever two or more thunderstorm cells merge together. A multi-cell thunderstorm may develop as a large cluster or it develops into a line of thunderstorms that is more commonly known as a squall line.

Figure 1.1 is an image of a developing cumulonimbus cloud that was seen from Darwin, Australia on December 2nd, 2002. The radar image of the thunderstorm clouds below the picture is evidence that the thunderstorm is a multi-cell system since there appear to be at least two storm cells that are connected.

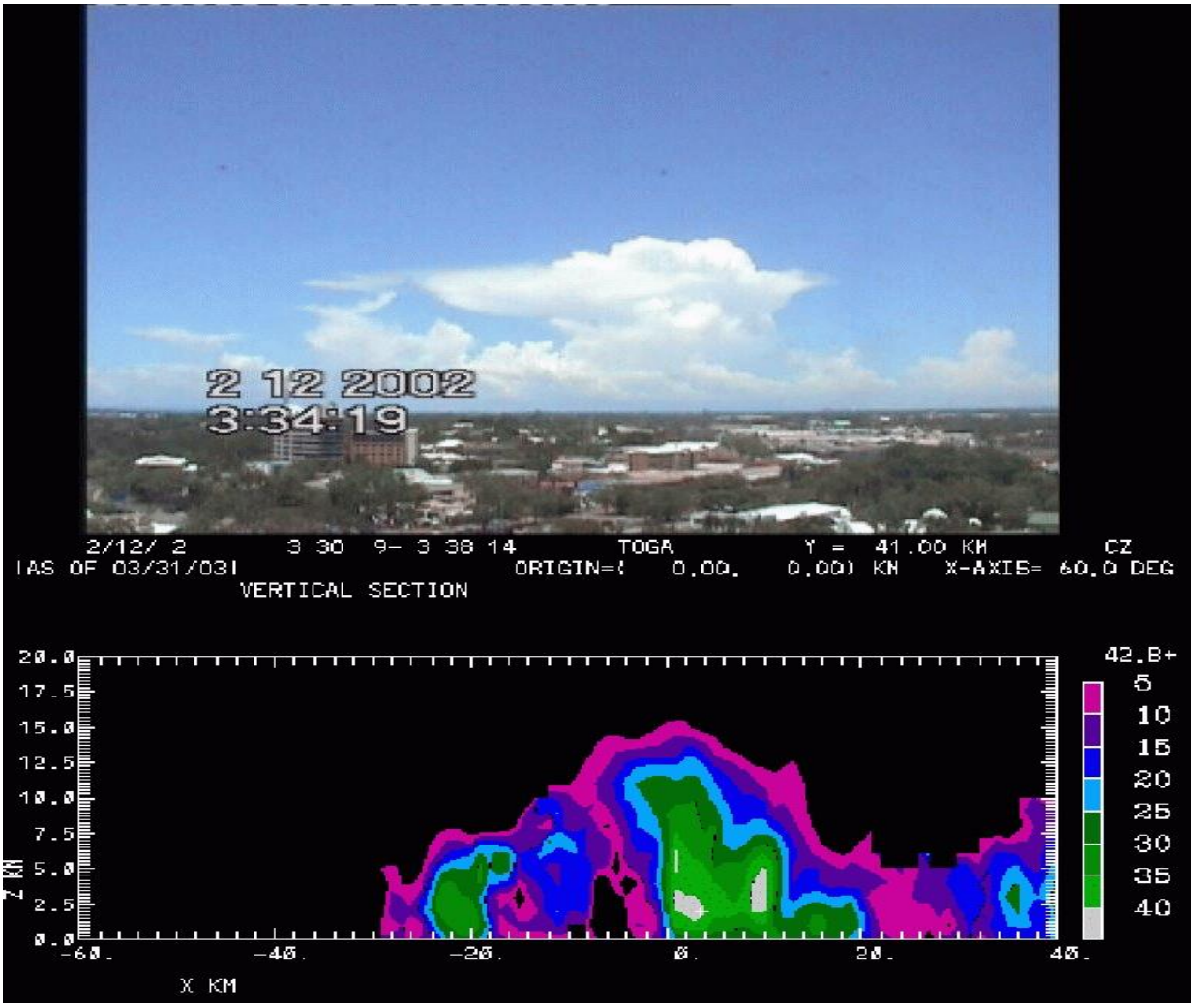

Figure 1.1: The development of cumulonimbus clouds (Hector) over the Tiwi Islands as seen from Darwin, Australia on December 2nd, 2002. Below the image of the cumulonimbus clouds there is a Doppler radar image that shows a vertical cross section of the multicellular convective system.

At the top of the cumulonimbus cloud the background wind blows ice crystals downstream and away from the core of the cloud. These ice crystals create a cirrus cloud that may extend hundreds of kilometers away from the core of the thunderstorm. The cirrus cloud is attached to the cumulonimbus cloud and the shape appears to be anvil-like. This is the reason why the cirrus cloud that develops in the cumulonimbus outflow is called an anvil cloud. If the updraft inside of the core of the thunderstorm is strong relative to the background wind a shorter anvil may develop on the back side of the thunderstorm and this is commonly known as the

back-sheared anvil. There have been various sightings of cloudy bubbles or lobes on the base of the anvil cirrus cloud, sometimes they are seen on the back-sheared anvil. These cloudy lobes that develop are called mammatus clouds. Figure 1.2 is a schematic of a strong multi-cell thunderstorm with an anvil cloud and mammatus on the base of the anvil.

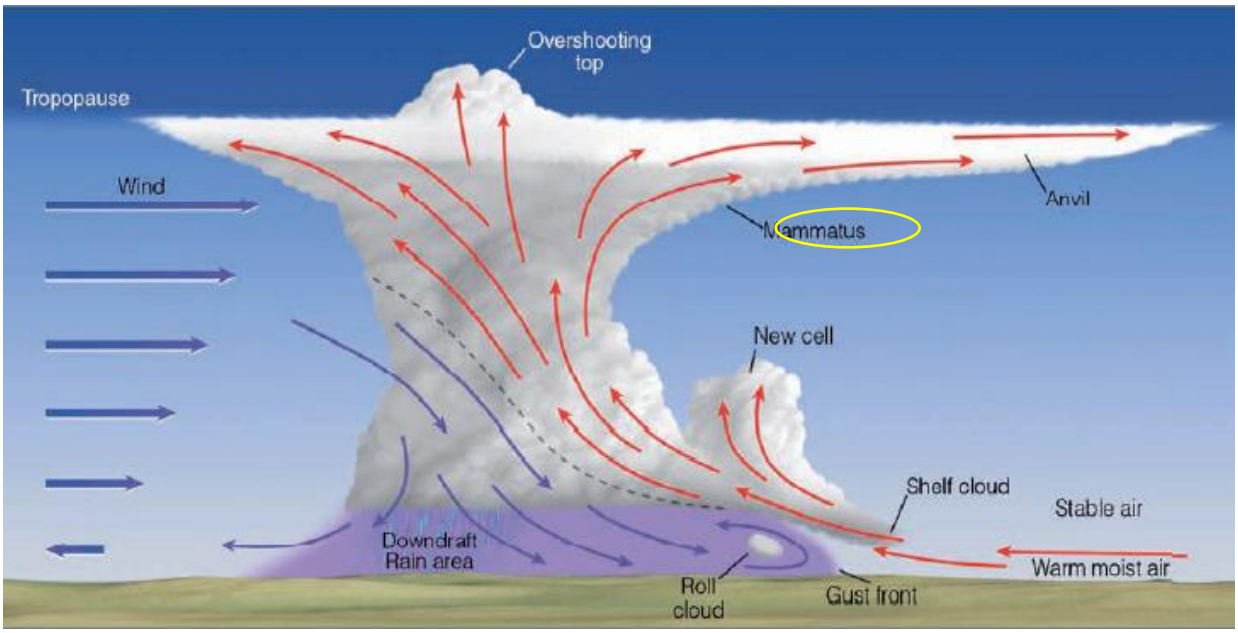

Figure 1.2: A diagram of a strong thunderstorm, mammatus clouds have been included in this diagram underneath the base of the anvil cloud. Taken from Ahrens, 2009.

The word mammatus is Latin for "having breasts." Mammatus clouds are described as smooth pouches on the underside of a cloud. This is often observed on the underside of a Cumulonimbus anvil but this is not the only type of cloud where mammatus have been observed. They have been associated with stratocumulus clouds, altostratus, altocumulus, cirrocumulus, and cirrus. Figure 1.3, (a), (b), (c), and (d) are pictures of mammatus clouds that developed underneath the anvil of cumulonimbus clouds. Notice how the lobes have a slightly different appearance in each of the 4 pictures. Mammatus clouds can vary in smoothness, shape and size depending on the conditions of the atmosphere.

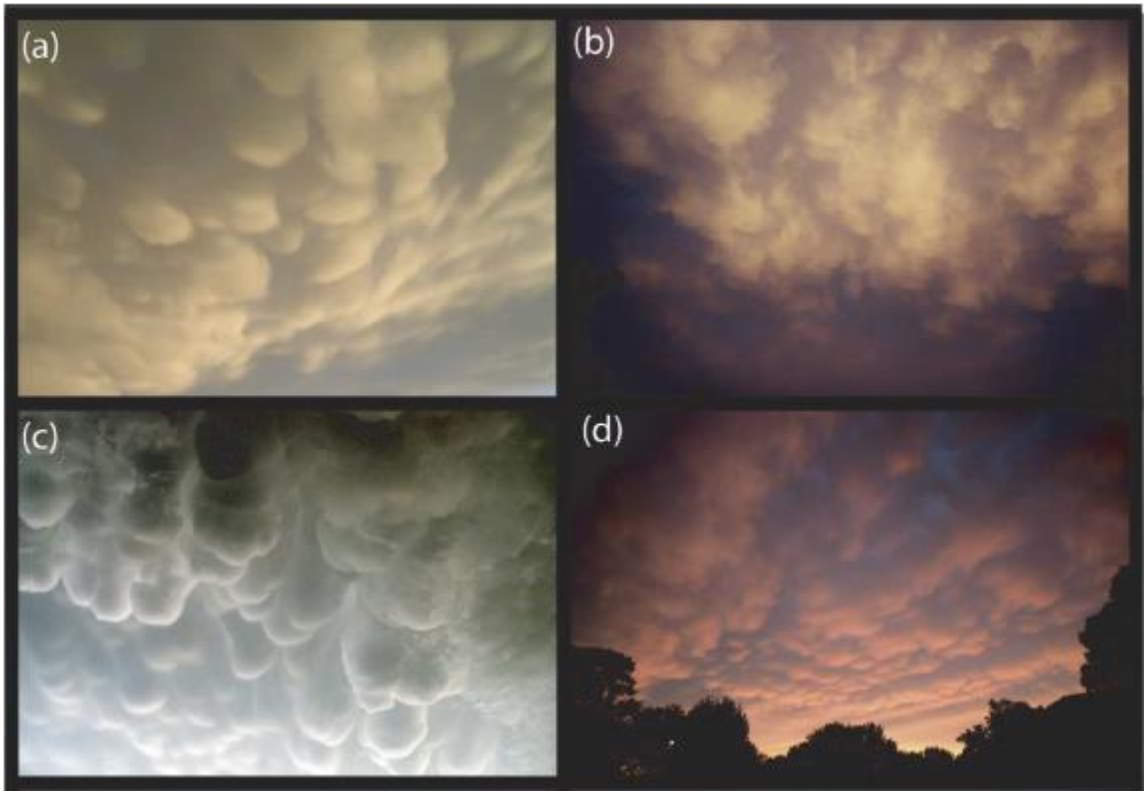

Figure 1.3: Various pictures of mammatus; the mammatus clouds in each of these pictures developed on the anvil of cumulonimbus clouds. Taken from Schultz et al., 2006.

The EMERALD (Egrett Microphysics Experiment with Radiation Lidar and Dynamics) project involved airborne measurement campaigns to study the microphysics, dynamics and IR radiative properties of cirrus clouds. EMERALD-1 was the field campaign to investigate cirrus clouds that were associated with mid-latitude frontal systems. EMERALD-1 took place in Adelaide, South Australia during September, 2001. EMERALD-2 was a field campaign based in Darwin, Australia during November and December of 2002 to investigate the anvil outflow of tropical deep convection. The data that will be analysed in this thesis comes from EMERALD-2.

Darwin was chosen due to its proximity to the Tiwi Islands where one of the world's largest regularly occurring thunderstorms takes place. This thunderstorm occurs almost every day during the pre-monsoon season of November - December in northern Australia. This

thunderstorm has been given the name “Hector” by the local community. Hector, develops when sea breezes generated at the coasts of the islands converge and trigger the development of one or more thunderstorm cells. Downdrafts of cool air from the thunderstorm reach the surface and move away from the thunderstorm in a radial fashion creating a gust front. The gust fronts converge with nearby sea breeze fronts or the gust fronts from neighbouring thunderstorms. This initiates more thunderstorm cells that become connected with the initial thunderstorm cells. This leads to more intense convection and a large convective system develops (Carbone & Wilson, 2000; Connolly et al., 2006). The Tiwi Islands (Figure 1.4) consist of Bathurst Island and Melville Island. These two islands are very close together and are effectively like one large island divided by a channel.

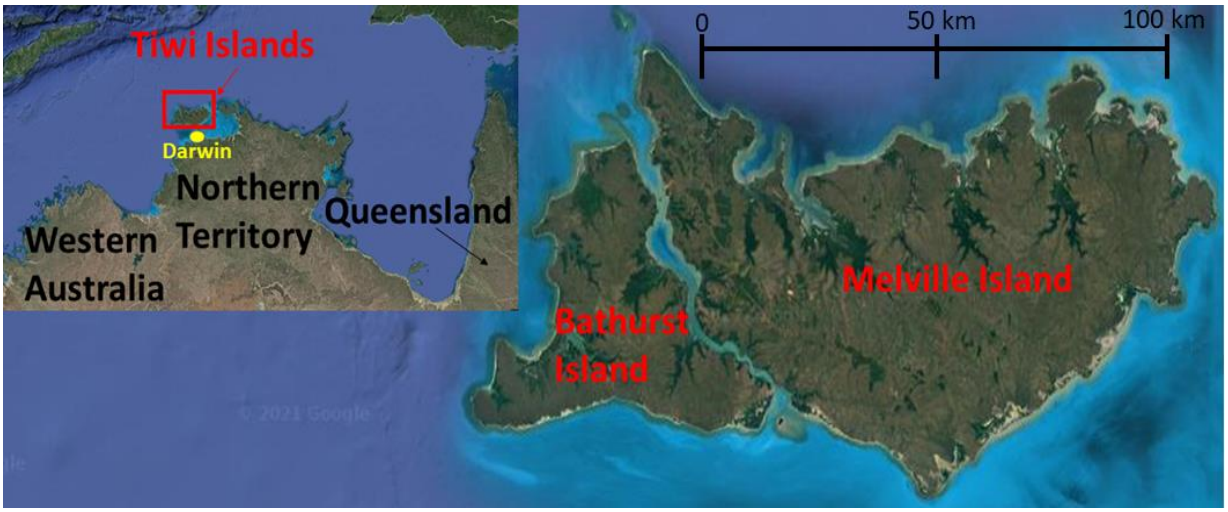

Figure 1.4: The location of the Tiwi Islands in the Northern Territory of Australia. Image generated by Google Maps.

Darwin is very close to the Tiwi Islands making it a very convenient base for the EMERALD-2 campaign. Turbulence probes were installed on the aircraft for measurements of pressure, temperature, and wind at turbulence scales. A frost point hygrometer and a TDL spectrometer were installed on the aircraft to measure the amount of moisture in the atmosphere. Optical scattering and imaging instruments measured the cloud microphysical properties, and the

spectrum of far infrared radiation was measured with a Michelson interferometer. Simultaneous measurements of the cloud structure that the Egrett was flying within were provided by a LIDAR on the King air aircraft, which was flying directly below the Egrett. This project concerns the interaction of atmospheric dynamics and the cloud structure within and around the anvil outflow.

This thesis concerns the analysis of a flight that had focussed on mammatus clouds at the base of the anvil outflow. The observations from December 2nd, 2002 are compared with predictions and assumptions of various mammatus formation theories. This information can be used to gain a better understanding of what caused the mammatus clouds to develop. There are close to a dozen theories that have been proposed but it is still not well understood which theories of mammatus formation are most relevant. The second objective is to determine the role of dynamics in sustaining the cirrus outflow from deep convection. These clouds are known to have a substantial role in climate with their impact on solar and IR radiation.

The information that was gathered from this research contains value for the scientific community. The dynamical processes have a significant impact on the development of the anvil cloud and its transformation from an optically thick cloud into an optically thin cloud. Thick anvil clouds have a net cooling effect on the earth while thin anvil clouds have a net warming effect (Gasparini et al., 2019). These same processes help to sustain the anvil cloud for great distances downwind from the core of the thunderstorm. Insights on the dynamics in the anvil outflow can be useful for the development of weather models or climate models. New findings on the development of mammatus clouds can help to verify the previous results from research on this subject. It can inspire new research on the topic of mammatus cloud formation.

The following is a short summary of the rest of the thesis. Chapter 2 contains background information and theory on concepts that are essential for understanding the experiment and its

results. Chapter 3 provides a description of the measurement and analyses methods which will include information on the research aircraft, the equipment used in the experiment, variables that were measured, experimental design, and the methods that were employed to analyze the data. Chapter 4 is a presentation of the relevant data that was gathered from the research flights and the interpretation of those results in relation to the formation of mammatus clouds. At the end of the chapter these results are compared to the expected observations from the mammatus cloud formation theories. Finally, Chapter 5 is an overview of the findings and it offers suggestions for future studies.

Chapter 2: Background

2.1 - Convection in the Tropics

2.1.1 - Structure of the Atmosphere

The earth's atmosphere is separated into four layers, based on the temperature trend throughout the layer. Starting from the surface and moving upwards the four layers are the troposphere, stratosphere, mesosphere, and thermosphere. Figure 2.1 is a diagram of the temperature structure and depth of the four layers of the atmosphere.

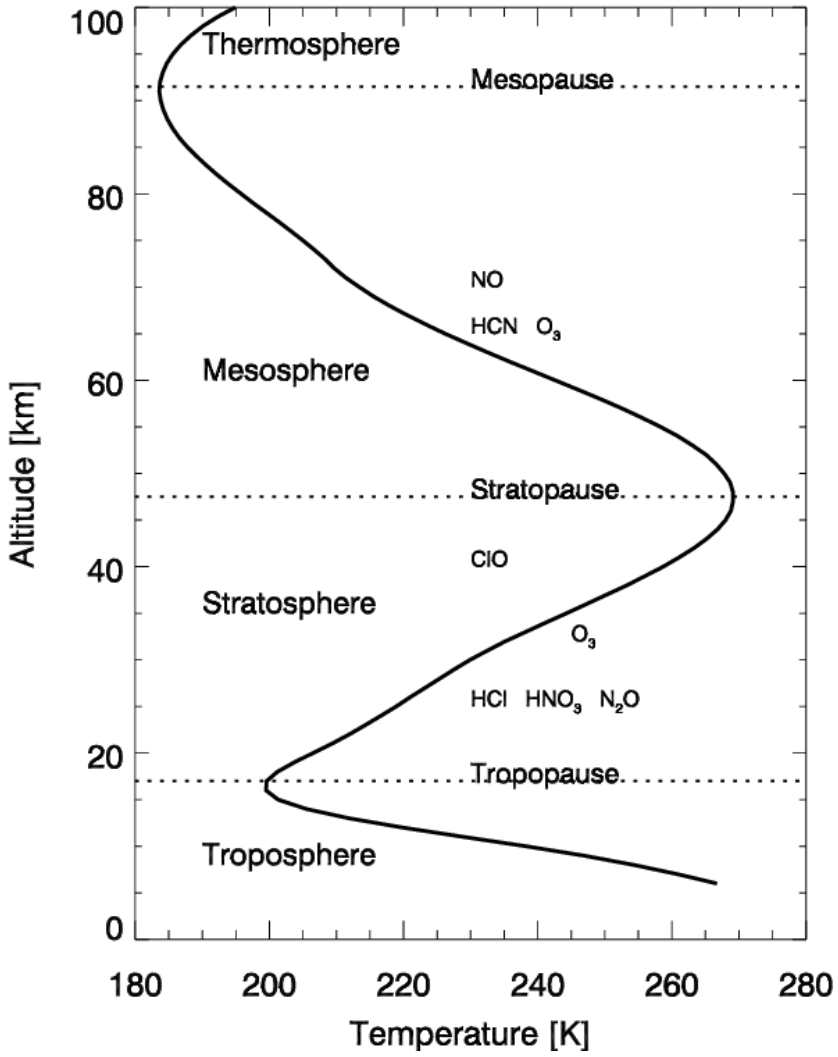

Figure 2.1: The typical structure of the atmosphere over tropical regions. Figure from Kuttippurath, 2005.

Inside of the troposphere the average temperature gradient is negative meaning that the temperature decreases as height above the surface increases. The troposphere's main source of heat is the solar radiation absorbed by the surface. Energy is transported upward from the surface by infrared radiation, conduction, convection, and latent heat. The transport of infrared radiation results in a vertical gradient of temperature that is unstable to vertical motion. As water condenses into clouds the released latent heat warms the air and the force of buoyancy pushes the air further upward (Ahrens, 2009).

Notice how the temperature is constant with height at an altitude of 17 km and then it starts to increase with altitude. This is considered to be the boundary between the troposphere and the stratosphere which is known as the tropopause. The vertical temperature gradient is positive throughout the stratosphere meaning that temperature increases with height. The height of the tropopause varies from approximately 17 km at the equator to just under 10 km at the poles (Birner, 2010). The standard definition of the tropopause is "the lowest level at which the lapse-rate decreases to 2°C/km or less, provided that the average lapse-rate between this level and all higher levels within 2 km does not exceed 2°C/km" (WMO, 1957).

Deep convection usually terminates in the troposphere but sometimes deep convection can temporarily overshoot into the stratosphere if the updraft has enough kinetic energy to pass through the tropopause. The top of the cumulonimbus cloud goes beyond the top of the anvil cloud which usually develops at the level of neutral buoyancy. This creates an overshooting top, a feature that is often associated with strong thunderstorms.

2.1.2 - Atmospheric General Circulation

The general circulation of the atmosphere is defined as the statistical description of large scale atmospheric motion (Hartmann, 2007). It is used to explain the patterns of the synoptic weather systems and winds that are observed around the world. There are 3 circulation cells between the equator and the poles in both hemispheres, there are 6 circulation cells in total between the North Pole and the South Pole. Figure 2.2 is a diagram of the 3 circulation cells that are found between the equator and the pole in either hemisphere. The cell that forms closest to the Equator is known as the Hadley cell, the cell that forms in the mid-latitudes is known as the Ferrel cell and the cell that forms over the poles is known as the Polar cell. Darwin, Australia is located at around 12ºS and falls under the circulation of the southern hemisphere Hadley cell.

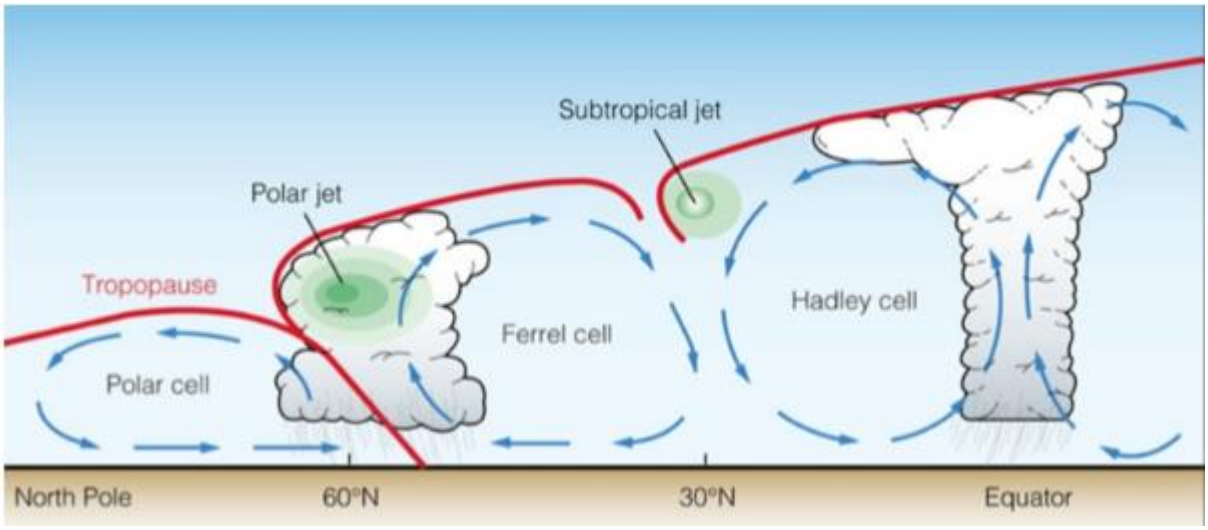

Figure 2.2: A diagram of the Hadley cell, Ferrel cell and Polar cell in the earth's atmospheric circulation model. The intertropical convergence zone is found at the convergence zone between the northern and southern Hadley cells. This model applies in the Southern Hemisphere as well. Figure taken from Levya, S, California State University, Los Angeles.

The Hadley cell circulation begins at the Equator where the sun's energy is most intense and the average surface temperature is warmest. Air rises at the equator creating a low pressure center. The air diverges once it reaches the tropopause and moves poleward until it converges

with air from the Ferrel cell. The air sinks and diverges at the surface creating a high pressure center. One branch of the air moves towards the equator while the other branch moves towards the poles. The branch that moves towards the equator completes the Hadley cell while the other branch that moves towards the poles completes the Ferrel cell.

High pressure systems have a tendency to develop between the intertropical convergence zone and the polar front. These high pressure centers are formed by air that is sinking and diverging at the surface. The high pressure systems develop in the same area where there is downward motion from the subsiding branch of the Hadley and Ferrell cells. (Frierson et al, 2007). The pressure gradient force always acts in the same direction as the pressure gradient, from high pressure to low pressure. As a result winds move away from the high pressure center towards the poles and also towards the equator. The Coriolis force causes the wind to turn towards the right in the northern hemisphere and in the southern hemisphere the wind must turn towards the left. The result on the surface of the Hadley Cells are north-easterly synoptic winds in the northern hemisphere and southeasterly synoptic winds in the southern hemisphere. The synoptic winds patterns are more commonly known as the trade winds. These winds converge at the equator and create a band of deep convection known as the intertropical convergence zone.

The intertropical convergence zone (ITCZ) is not always right on the Equator, it will shift towards the warmer hemisphere. Over the Indian Ocean the position of the ITCZ can reach an average latitude of 20^{o}N during the northern hemisphere summer and it shifts to an average latitude of 8^{o}S during the southern hemisphere summer (Keshtgar et al., 2020). The intertropical convergence zone is close to the Equator during the equinox seasons (Spring & Fall). The position of the ITCZ over the Indian Ocean has a major impact on the seasons in northern Australia.

In Darwin, Australia the intertropical convergence zone moves into the region during the monsoon season which is from December to March. It is the main cause of deep convection in Northern Australia during the Southern Hemisphere summer (Doyle, 2019). The deep convection that is known as Hector occurs before the monsoon arrives so this would be when the Tiwi Islands is under the influence of sinking air immediately outside of the intertropical convergence zone and the high pressure centers near 30°S. The sky is clear and the weather is calm, in the absence of any major synoptic events. Mesoscale events such as sea breezes become the weather makers.

2.1.3 - Sea Breeze Circulation

The convective system which develops over the Tiwi Islands is caused by the convergence of sea breezes. Sea breezes converge over the Tiwi Islands and act as a forcing mechanism for the deep convection that develops regularly over this region during the pre-monsoon season (Carbone & Wilson, 2000). Sea breezes are driven by the temperature gradient between the land and the water (Raifq et al., 2020). Figure 2.3 is a schematic of the sea breeze circulation that typically develops during a warm day.

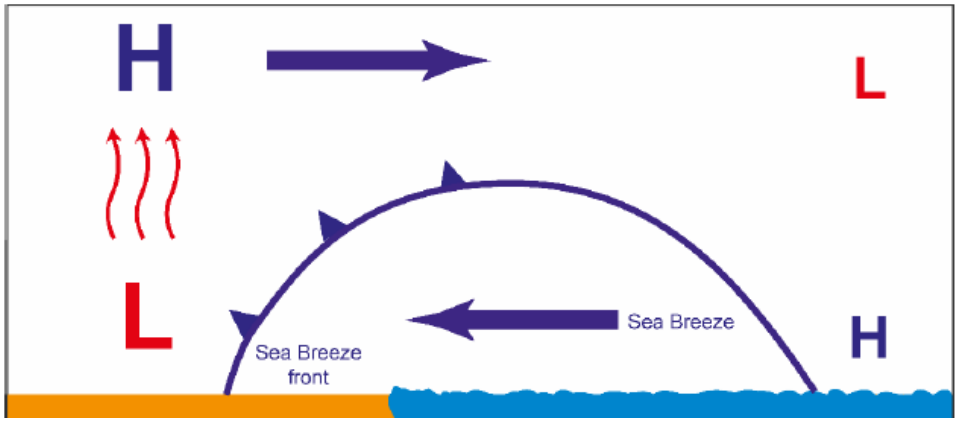

Figure 2.3: The sea breeze (or lake breeze) circulation pattern which develops when the temperature of the land is higher than the temperature of the sea. Figure taken from Rafiq et al., 2020.

First the land is warmed by the sun and air rises over the land creating a thermal low pressure system over the land. A pressure gradient is created between the sea and the land. Air moves from the sea towards the land where the pressure is lower. This creates the sea breeze that can be observed along the coast whenever the land is significantly warmer than the water. Sea breeze convergence is a common trigger for deep convection.

2.2 - Climate of the Tiwi Islands and Northern Australia

The monsoon in northern Australia is what defines the two seasons that are experienced each year: the wet season and the dry season. The dry season occurs when the dominant flow in the lower and middle troposphere is southerly or southeasterly over northern Australia. During the wet season this dominant flow reverses and becomes westerly or northwesterly. Moist air from the Indian Ocean rises over the continent of Australia due to orographic effects and the monsoon trough. This leads to rainy weather over northern Australia. The Hector thunderstorm occurs at the end of the dry season, during this time of the year an easterly flow persists over northern Australia and thunderstorms develop over the islands in the Indian Ocean (Keenan et al., 1990). Figure 2.4 is the map of Australia and the typical synoptic weather pattern that occurs during the dry season.

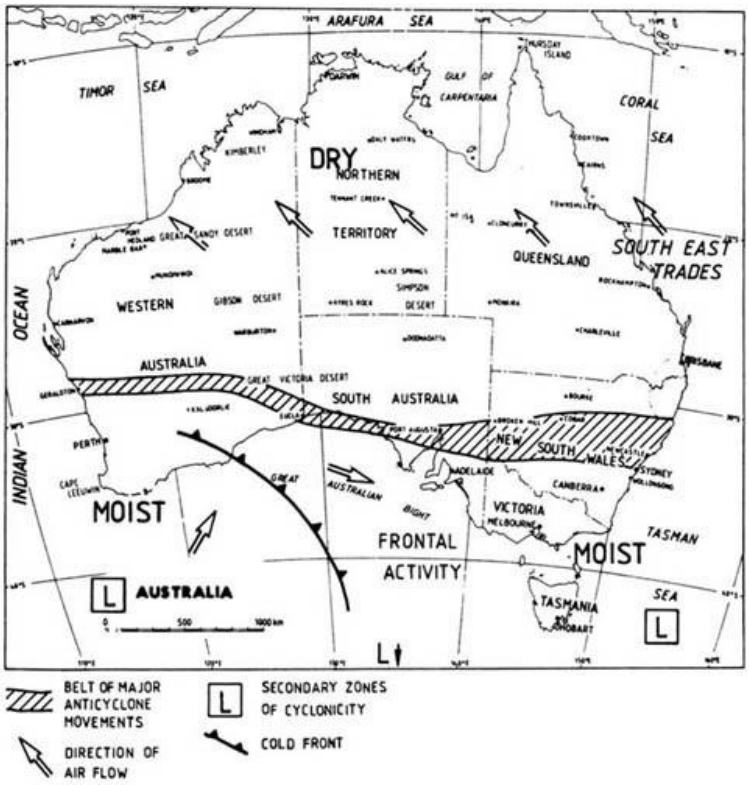

Figure 2.4: Typical weather pattern that develops during the dry season in northern Australia, Thunderstorm development over the Tiwi islands is associated with the end of the dry season. Figure taken from Bridgman, 1998.

During the dry season northern Australia is under the influence of a southeasterly flow due to the high pressure systems in southern Australia and the trade winds which blow across the continent of Australia. The air that travels across the desert is dry and stable so this causes clear skies and a lack of weather systems in northern Australia. It is during this time of year that the surface can heat up and eventually the temperature gradient between the land and the Indian Ocean is large enough for sea breezes to develop. As stated previously it is the convergence of sea breezes that causes the development of convection over the Tiwi Islands during the pre-monsoon months (Carbone & Wilson, 2000).

2.3 - Atmospheric Variables

2.3.1 - Equation of State

The equation of state for the atmosphere is the ideal gas law, which relates pressure, density and temperature together

$$P = \rho RT \quad (2.1)$$

where *P* is the air pressure in Pascals, ρ is density in kg/m^3 and *T* is the air temperature in Kelvin. *R* is the ideal gas constant which is 287 J kg^{-1} K^{-1}. Pressure in the Earth's atmosphere is not constant and it decreases exponentially with altitude above the surface. There is a large vertical pressure gradient that is directed upwards. The pressure gradient force must balance the force of gravity. This balance can be expressed by the hydrostatic equation

$$\frac{\partial P}{\partial z} = -\rho g \quad (2.2)$$

where $\frac{\partial P}{\partial z}$ is the vertical derivative of pressure, or the vertical pressure gradient in Pa/m and g is acceleration due to gravity which is 9.81 m/s^2. The ideal gas law (equation 2.1) can be solved for density ($\rho = \frac{P}{RT}$) and then substituted into equation 2.2.

$$\frac{\partial P}{\partial z} = \frac{-Pg}{RT} \quad (2.3)$$

Next equation 2.3 can be solved as a separable equation to produce the Barometric equation

$$P(z) = P_0 e^{-\frac{z}{H}} \quad (2.4)$$

where *H* is the scale height. It is equivalent to *RT/g*. This is the vertical distance required for the atmospheric pressure to change by a factor of *e* (2.71828).

2.3.2 – Humidity

Water can exist in the atmosphere in all 3 physical states. It can exist as solid ice particles, liquid water droplets or it can be in a gaseous state as water vapour. This section focuses on the variables that are used to express how much water vapour is in the air. These variables are absolute humidity, specific humidity, mixing ratio, relative humidity and vapour pressure. Absolute humidity is defined as the mass of water vapour divided by the volume of air usually in units of grams per cubic meter. Mixing ratio can be expressed in parts per million by volume, or as the mass of water vapour divided by the total mass of air (Korotcenkov, 2018). If the total mass of the air is not known it is more convenient to express humidity by using the water vapour mixing ratio. Vapour pressure is the partial pressure exerted by water vapour. The vapour pressure increases when more water vapour molecules are added to the air, more molecules will mean that more pressure is exerted due to water vapour (Wiederhold, 1997).

Each of these humidity measurements can be used as an expression for the total amount of water vapour that is in the air but the humidity variables can also be used to figure out which parts of the atmosphere will see water vapour condense into cloud droplets. The rate that water vapour condenses (deposits) onto a surface of liquid (ice) water is dependent on the vapour pressure. The rate at which water evaporates (sublimates) from a surface of liquid (ice) water is dependent on the temperature. When the rate of condensation (deposition) is equal to the rate of evaporation (sublimation) a parcel of air is holding the maximum amount of water vapour, which is called the saturation vapour pressure. The saturated vapour pressure is thus dependent on temperature. The vapour pressure of the air at saturation and the mixing ratio of the air at saturation can be calculated if the temperature is known for that air parcel. The air in a cloud is always very close to saturation over either ice or liquid water. If the temperature of saturated air

decreases, the rate of evaporation (sublimation) would decrease and condensation (deposition) would exceed evaporation (sublimation). If the temperature increases then the rate of evaporation (sublimation) would exceed the rate of condensation (deposition) until a new equilibrium was reached.

Saturation vapour pressure represents the vapour pressure of the air when water vapour begins to condense (deposit) into water droplets (ice crystals). This can be calculated using the Clausius-Clapeyron equation for which the Arden-Buck equation is an accepted approximation at very low temperatures (Buck, 1981)

$$e_s = 6.1121\exp\left((18.678 - \frac{T}{234.5})(\frac{T}{257.14+T})\right) \text{ w.r.t liquid water (2.5a)}$$

$$e_s = 6.1115\exp\left((23.036 - \frac{T}{333.7})(\frac{T}{279.82+T})\right) \text{ w.r.t solid ice (2.5b)}$$

where e_s is the saturation vapour pressure and T is the temperature of the air in Celsius. Mixing ratio and saturation mixing ratio can be calculated using the following equation

$$w = \varepsilon \frac{e}{P} \text{ (2.6)}$$

where w is the mixing ratio in kg/kg, ε is the ratio of the gas constant for dry air to the gas constant for water vapour (0.622), e represents vapour pressure and P is the total atmospheric pressure. Saturation mixing ratio can be determined by substituting the saturation vapour pressure into the equation. Mixing ratio and saturation mixing ratio can be calculated with respect to ice by using equation 2.5b to solve for vapour pressure (e). If the mixing ratio is greater than or equal to saturation mixing ratio with respect to ice then water vapour begins to be deposited as ice on particles in the air, creating ice crystals.

Relative humidity is defined as the ratio of the vapour pressure to the saturation vapour pressure or the ratio of the mixing ratio to the saturation mixing ratio (Wiederhold, 1997). Relative humidity is expressed as a percentage (the ratio is multiplied by 100). Relative humidity can also be calculated with respect to ice. In this case it is the ratio of the vapour pressure over ice to the saturation vapour pressure over ice, or the mixing ratio with respect to ice divided by the saturation mixing ratio with respect to ice. Water vapour begins to be deposited as ice on particles in the air when relative humidity is 100% or higher with respect to ice.

2.3.3 – Atmospheric Stability

The stability of the atmosphere is the deciding factor in the development of deep convection. The atmosphere is considered to be stable if the force of buoyancy opposes upward or downward motion. A parcel of air that is displaced vertically will oscillate about its initial position in a stable atmosphere. The opposite condition is an unstable atmosphere in which the force of buoyancy is in the direction of displacement and air parcels will accelerate away from their original position when they are vertically displaced (Markowski, 2007). Air parcels that are less dense than their surrounding environment experience an upward pressure gradient force that is greater than the downward force of gravity and will move upwards. Air parcels that have a higher density than their environment will be acted upon by a downward force of gravity that is greater than the upward pressure gradient force and will move downwards. The temperature of a gas is related to its density and this relationship is clear when the ideal gas law is rearranged so density is on the left side of the equation

$$\rho = \frac{P}{RT} \quad . \text{(2.7)}$$

Density and temperature are inversely proportional so air that is warmer than the surroundings will rise while colder air will sink. In an unstable atmosphere the rising air parcels are always warmer than the surrounding air and sinking air parcels are always colder than their surroundings so the air parcels keep moving vertically until they reach a point where they are at the same temperature as the environment.

When an unsaturated air parcel rises above the surface it expands adiabatically as the air molecules perform work on the surrounding atmosphere. In an adiabatic process no heat is transferred from the air parcel to the surrounding environment. The temperature in the air parcel will drop since the air molecules use their own internal energy to help the parcel expand (Nugent & DeCou, 2019). The temperature of this air parcel will decrease at the dry adiabatic lapse rate

$$\Gamma_d = -\frac{dT}{dz} = \frac{g}{c_p} \quad (2.8)$$

where c_p is the specific heat of dry air, 1005 J kg^{-1} K^{-1}. Γ_d is approximately 9.81 ^{o}C/km in the troposphere.

A saturated air parcel will cool at a much slower rate because water vapour is condensing into liquid water as the air parcel rises. Latent heat is released into the air parcel when condensation occurs so the temperature of a saturated air parcel will decrease at a slower rate while ascending (Rogers & Yau, 1989). The temperature of the saturated air parcel will decrease at the saturated adiabatic lapse rate (Markowski, 2007). The process is not truly adiabatic due to release of latent heat and is called the pseudo adiabatic (or wet, or saturated) lapse rate.

$$\Gamma_s = -\frac{dT}{dz} = \frac{\Gamma_d}{1+(\frac{L\ dw_s}{c_p\ dT})} \quad (2.9)$$

Where L is the latent heat of condensation, and w_s is the saturation mixing ratio. The stability of the atmosphere is based on comparing the environmental lapse rate (Γ_e) with the lapse rate of the air parcels. If Γ_e is less than Γ_d & Γ_s the atmosphere is stable. Air parcels that move vertically will return to their initial position. If Γ_e is greater than Γ_s but less than Γ_d the atmosphere is conditionally unstable and this means that saturated air parcels can become unstable but dry air parcels will remain stable. Finally if Γ_e is greater than Γ_d the atmosphere is absolutely unstable and all air parcels would be able to move vertically under the force of buoyancy.

2.3.4 – Potential Temperature

Potential temperature is defined as the temperature that an air parcel would have if it was compressed adiabatically to a reference pressure level. Usually this is the 1000 hPa pressure level. The potential temperature equation is as follows,

$$\theta = T\left(\frac{P_o}{P}\right)^{\frac{R}{cp}} \quad (2.10)$$

where T is the air temperature in Kelvin, P_o is the reference pressure level, P is the pressure at the altitude of the air parcel, R is the gas constant for dry air (287 J kg^{-1} K^{-1}) and c_p is the specific heat of dry air.

Potential temperature is always conserved for an adiabatic process and as a result the dry adiabatic lapse rate corresponds with constant potential temperature (Rogers & Yau, 1989). The potential temperature gradient can be used to determine atmospheric stability for dry air. The atmosphere is stable if potential temperature increases with height. This corresponds to the

environmental lapse rate being less than the dry adiabatic lapse rate. The atmosphere is unstable if potential temperature decreases with height. This will correspond to an environmental lapse rate that is higher than the dry adiabatic lapse rate. If potential temperature is constant with height the atmosphere is neutral and the environmental lapse rate is equal to the dry adiabatic lapse rate. An atmosphere with constant potential temperature is also a sign of mixing since the lapse rate in a layer of dry air will be close to dry adiabatic with thorough mixing (Rogers & Yau, 1989).

Potential temperature requires air to be brought to the reference level adiabatically, this is not possible for saturated air since latent heat is released within the air parcel. Equivalent potential temperature is the temperature an air parcel would reach if all the water vapour is first condensed with the release of latent heat before it is brought adiabatically to a reference pressure level (Rogers & Yau, 1989). It is given by the equation

$$\theta_e = \theta exp(\frac{L}{c_p}\frac{w_s}{T}) \quad (2.11)$$

where T is the temperature of the air in Kelvin. L, w_s, and c_p are the same as previously defined. T and w_s are the temperature and mixing ratio where the air becomes saturated after being lifted adiabatically. The equivalent potential temperature gradient can be used to determine the stability of saturated air in the atmosphere. If equivalent potential temperature increases with height then the atmosphere is stable for saturated air. The atmosphere is neutral for moist air if equivalent potential temperature is constant with height and the atmosphere is unstable for saturated air if equivalent potential temperature decreases with height.

2.3.5 – Brunt-Väisälä Frequency

Vertical acceleration of air can be expressed as,

$$\frac{d^2z}{dt^2} = -\left(\frac{g}{\theta}\frac{\partial\theta}{\partial z}\right)z = -N^2z \quad (2.12)$$

where N can be defined as $\left(\frac{g}{\theta}\frac{\partial\theta}{\partial z}\right)^{1/2}$ and is called the Brunt-Väisälä frequency (Rogers & Yau, 1989).

The Brunt-Väisälä frequency has units of radians per second. It is the frequency of an oscillating air parcel in a stable atmosphere. If the atmosphere is stable an air parcel that is displaced vertically will be subject to a force of buoyancy directed to its original altitude but the inertia of the air parcel causes it to go past its original altitude so it starts to oscillate back and forth (Stull, 2016). This is considered to be the highest possible frequency for gravity waves in the atmosphere (Wüst, 2017).

The Brunt-Väisälä frequency depends on the potential temperature gradient. When the potential temperature gradient is positive the Brunt-Väisälä is also positive, the atmosphere is stable, and the frequency value will be a real number which represents the frequency of a buoyancy oscillation. If the vertical potential temperature is constant with height then $\frac{\partial\theta}{\partial z}$ is 0 and the Brunt-Väisälä is equal to 0 which means there is no buoyancy oscillation. The physical reason for this is the air in a neutral atmosphere will not move vertically due to buoyancy. Finally, if the potential temperature gradient is negative then N^2 is a negative number and the Brunt-Väisälä frequency becomes an imaginary number. If N^2 is negative and it gets substituted into equation 2.12 then there will be positive acceleration of the air. This means that the force of

buoyancy will be in the direction of displacement and displaced air parcels will continue to accelerate vertically

2.4 – Waves

2.4.1 – Internal Gravity Waves

In section 2.3.5 it was mentioned that the Brunt-Väisälä frequency represents the frequency of the oscillation of an air parcel that is displaced vertically and then oscillates above and below its equilibrium level due to the force of buoyancy. The air parcel creates a periodic disturbance, similar to that of a sine wave with a single frequency that is equal to the Brunt-Väisälä frequency. The movement of the air parcel would constitute a buoyancy oscillation, also commonly known as a gravity wave. More specifically, this is an internal gravity wave since it propagates through a fluid. The term gravity waves implies that gravity is the restoring force acting on the air parcel but the restoring force is actually buoyancy (Nappo, 2013). The air parcel's temperature is changing at the adiabatic lapse rate (pseudo adiabatic lapse rate if it is saturated) and since the atmosphere is stable the parcel is cooler than its environment when it gets displaced upward and a downward force of buoyancy acts on the parcel causing it to sink. The opposite is true when the air parcel is displaced downward.

The following equations of motion are for two dimensional, incompressible and irrotational flow in the atmosphere. The Boussinesq approximation is applied to density. The momentum equation in the zonal direction, the momentum equation in the vertical direction, the continuity equation, the conservation of mass equation, and the ideal gas law.

$$\frac{\partial u}{\partial t} + u\frac{\partial u}{\partial x} + w\frac{\partial u}{\partial z} = -\frac{1}{\rho}\frac{\partial P}{\partial x} \quad (2.13a)$$

$$\frac{\partial w}{\partial t} + u\frac{\partial w}{\partial x} + w\frac{\partial w}{\partial z} = -\frac{1}{\rho}\frac{\partial P}{\partial z} - g \quad (2.13b)$$

$$\frac{\partial u}{\partial x} + \frac{\partial w}{\partial z} = 0 \quad (2.13c)$$

$$\frac{\partial \theta}{\partial t} + u\frac{\partial \theta}{\partial x} + w\frac{\partial \theta}{\partial z} = 0 \quad (2.13d)$$

$$P = \rho RT \quad (2.13e)$$

The equations are linearized by separating the variables into the background component and the perturbation from the background.

$$u = \bar{u} + u' \quad (2.14a)$$

$$\theta = \bar{\theta} + \theta' \quad (2.14b)$$

$$w = \bar{w} + w' \quad (2.14c)$$

$$P = \bar{P} + P' \quad (2.14d)$$

$$\rho = \rho_0 + \rho' \quad (2.14e)$$

After linearizing the variables and applying the Boussinesq approximation the result is the following system of equations.

$$\frac{\partial u'}{\partial t} + \bar{u}\frac{\partial u'}{\partial x} + w'\frac{\partial \bar{u}}{\partial z} = -\frac{1}{\rho_0}\frac{\partial P'}{\partial x} \quad (2.15a)$$

$$\frac{\partial w'}{\partial t} + \bar{u}\frac{\partial w'}{\partial x} = -\frac{1}{\rho_0}\frac{\partial P'}{\partial z} - \frac{\theta'}{\bar{\theta}}g \quad (2.15b)$$

$$\frac{\partial u'}{\partial x} + \frac{\partial w'}{\partial z} = 0 \quad (2.15c)$$

$$\frac{\partial \theta'}{\partial t} + \bar{u}\frac{\partial \theta'}{\partial x} + w'\frac{\partial \bar{\theta}}{\partial z} = 0 \quad (2.15d)$$

Equation 2.15d can be rewritten so that it is a function of N^2 since $\frac{\partial \bar{\theta}}{\partial z} = \frac{N^2\theta}{g}$, the result is

$$\frac{\partial \theta'}{\partial t} + \bar{u}\frac{\partial \theta'}{\partial x} + w'\frac{N^2\bar{\theta}}{g} = 0. \quad (2.15e)$$

Next the system of equations (2.15a, 2.15b, 2.15c and 2.15e) is simplified using substitution and elimination. The simplified equation is a function of *w'*

$$\left(\frac{\partial}{\partial t} + \bar{u}\frac{\partial}{\partial x}\right)^2\left(\frac{\partial^2 w'}{\partial x^2} + \frac{\partial^2 w'}{\partial z^2}\right) + N^2\frac{\partial^2 w'}{\partial x^2} = 0. \quad (2.16)$$

The solutions to this system of equations take the form of complex exponential functions.

$$u', v', w', \theta', P' = Ae^{i(kx+mz-\omega t)} \quad (2.17)$$

Where *k* and *m* are the horizontal and vertical wavenumbers, ω is the frequency of the wave. Equation 2.17 is then substituted into equation 2.16 and the resulting equation is solved for wave frequency.

$$(-i\omega + ik\bar{u})^2 (-k^2 - m^2) + N^2(ik)^2 = 0$$

$$\omega^2 - 2\bar{u}\, k\omega + \bar{u}^2 k^2 - \frac{N^2 k^2}{\sqrt{k^2+m^2}} = 0 \quad (2.18)$$

Equation 2.18 is solved by using the quadratic equation and the solution contains the dispersion relationship for internal gravity waves.

$$\omega = \bar{u}\, k \pm \frac{Nk}{\sqrt{k^2+m^2}} \quad (2.19)$$

Equation 2.17 satisfies the dispersion relationship for internal gravity waves,

$$\hat{\omega} = \frac{Nk}{\sqrt{k^2+m^2}} \quad (2.20)$$

where *N* is the Brunt-Väisälä frequency. The dispersion relationship is used to determine the phase velocity of the wave. This is the velocity of one individual wave.

$$\overrightarrow{C_p} = \left(\frac{\hat{\omega}}{k}, \frac{\hat{\omega}}{m}\right) \quad (2.21)$$

$$\overrightarrow{C_p} = \left(\frac{N}{\sqrt{k^2+m^2}}, \frac{Nk}{m\sqrt{k^2+m^2}}\right) \quad (2.22)$$

The dispersion relationship can be used to determine the group velocity for internal gravity waves. This is the velocity of the wave energy.

$$\overrightarrow{C_g} = \left(\frac{\partial \hat{\omega}}{\partial k}, \frac{\partial \hat{\omega}}{\partial m}\right) \quad (2.23)$$

$$\overrightarrow{C_g} = \left(\frac{Nm^2}{(k^2+m^2)^{\frac{3}{2}}}, \frac{-Nkm}{(k^2+m^2)^{\frac{3}{2}}}\right) \quad (2.24)$$

For the next section, the wave vector will be introduced, it is denoted as $\vec{k}$ and it is a three dimensional vector that represents the direction of the phase velocity. It can be shown that the dot product of the wave vector $\vec{k}$ and group velocity $\overrightarrow{C_g}$ are equal to zero which means that the phase propagation is perpendicular to the group propagation (energy propagation).

$$\vec{k} \,.\, \overrightarrow{C_g} = C_{px}k_x + C_{pz}k_z = C_{px}k + C_{pz}m \quad (2.25)$$

$$\vec{k} \,.\, \overrightarrow{C_g} = \frac{Nkm^2}{(k^2+m^2)^{\frac{3}{2}}} - \frac{Nkm^2}{(k^2+m^2)^{\frac{3}{2}}} = 0 \quad (2.26)$$

Phase velocity and group velocity always have opposite vertical components. Figure 2.5 is an illustration of the propagation of gravity waves.

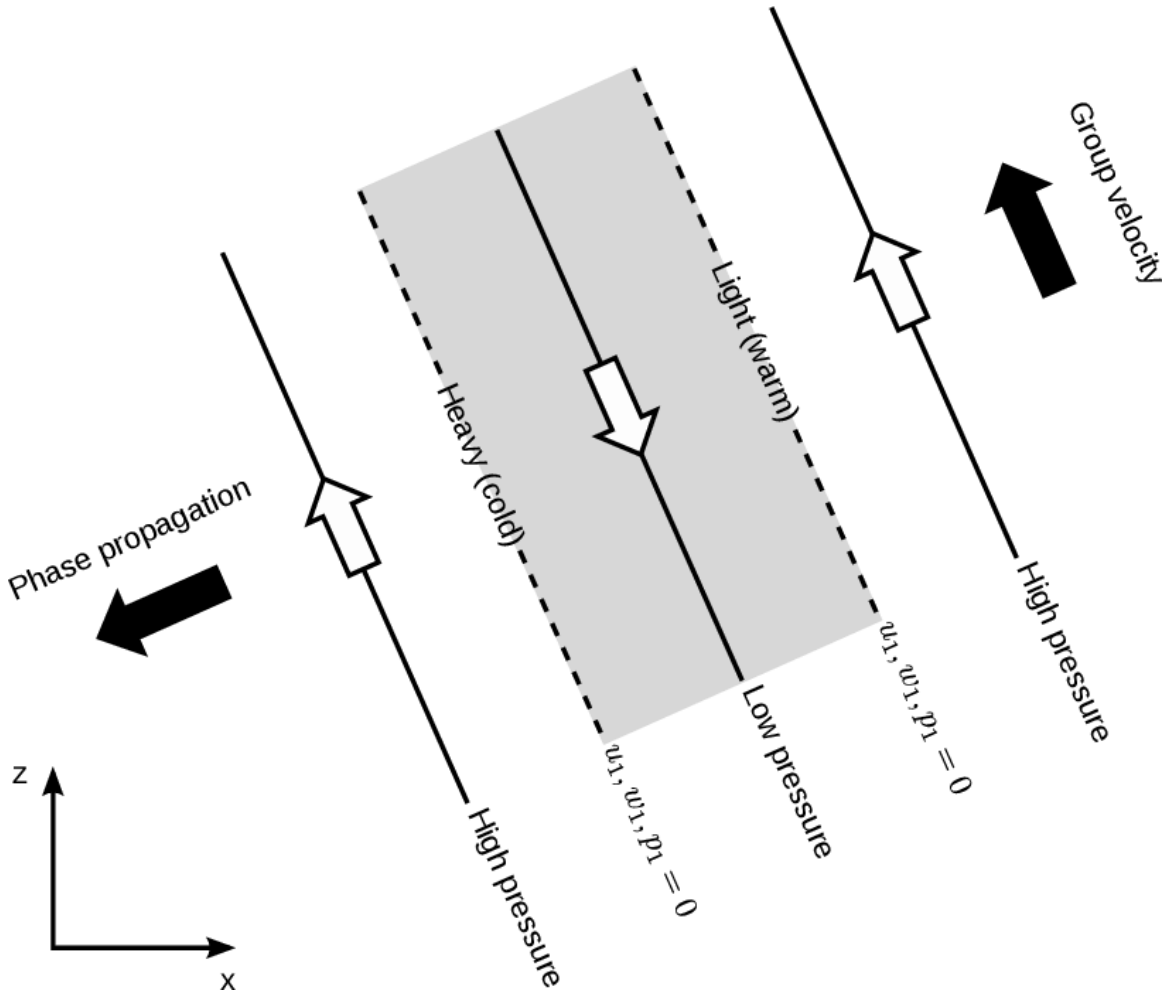

Figure 2.5: Schematic of the propagation of an atmospheric gravity wave. Figure taken from Allaerts, 2016

The direction of gravity wave propagation depends on the sign of the horizontal and vertical wavenumbers (*k* & *m* respectively). If both *k* & *m* are greater than 0 the gravity waves will propagate towards the east and upwards. If both *k* & *m* are less than 0 the gravity waves propagate downward and towards the west. If *k* is positive and *m* is negative gravity waves will propagate downward and toward the east. If *k* is negative and *m* is positive the gravity waves will propagate upwards and towards the west.

2.4.2 – Evanescent Gravity Waves

Evanescent gravity waves are gravity waves that only propagate horizontally, in this case the vertical wave number (m) is not a real number. The dispersion relationship can be rearranged to solve for vertical wavenumber.

$$m = \pm k\sqrt{\frac{N^2}{\omega^2} - 1} \quad (2.27)$$

If the ratio $\frac{N^2}{\omega^2}$ is greater than or equal to 1 then the number under the square root is positive and vertical wavenumber will be real. If $\frac{N^2}{\omega^2}$ is less than 1, the number under the square root will be negative which will mean that vertical wavenumber is also imaginary and an evanescent wave is able to occur (Nappo, 2013). This means that an evanescent gravity wave can be observed whenever the frequency of the wave is greater than N. Doppler shifting of the wave frequency can cause a vertically propagating gravity wave to become evanescent or vice versa.

2.4.3 – Ducted Gravity Waves

In the previous section it was shown that the vertical wavenumber (denoted, *m*) of a gravity wave is quantified by equation 2.27.

$$m = \pm k\sqrt{\frac{N^2}{\omega^2} - 1}$$

The vertical wavenumber will be a real value if the ratio $\frac{N^2}{\omega^2}$ is greater than or equal to 1. If the frequency of the wave is shifted so that the ratio $\frac{N^2}{\omega^2}$ is less than 1 then the vertical wavenumber is an imaginary number. This will be interpreted as a physical discontinuity in the vertical propagation of the gravity wave. When a gravity wave reaches the discontinuity it may be reflected or refracted based on its angle of incidence (Nappo, 2013).

Gravity waves are ducted or trapped if they are placed between two layers where the vertical wavenumber is discontinuous. Some waves may be able to be refracted into the wave duct while other waves get trapped because they are reflected by both of the layers of discontinuity. Inside of the wave duct the incident wave and the refracted wave may interact to form a standing wave. Evanescent (horizontally propagating) gravity waves may develop if the vertical wave number of the standing wave is complex. It is also possible to have a refracted gravity wave become an evanescent gravity wave if the vertical wavenumber changes and becomes complex.

The Scorer parameter can be used to find reflecting layers in the atmosphere. R.S. Scorer developed the Scorer parameter (denoted ι) and said that the Scorer parameter must normally decrease with height in order for gravity waves to occur over level ground to the lee of mountains. (Scorer, 1949). The Scorer parameter decreases sharply with height wherever there is a discontinuity in the vertical wavenumber. The square of the Scorer parameter is easily quantified using the equation from Trier & Sharman (2018)

$$\iota^2 = \frac{N^2}{(U-c)^2} - \frac{\frac{d^2U}{dz^2}}{U-c} \text{ . (2.28)}$$

The second term in the equation is eliminated whenever $\frac{d^2U}{dz^2} = 0$. If the value of $\frac{d^2U}{dz^2}$ is very close to 0 then the second term of equation 2.28 can be ignored and the square of the Scorer parameter can be approximated as

$$\iota^2 \cong \frac{N^2}{(U-c)^2} \quad (2.29)$$

where N^2 is the static stability or the square of the Brunt-Väisälä frequency, U is the wind speed in the direction of horizontal wave propagation, and c is the phase speed of the wave. If the wave has zero phase speed relative to the ground ($c = 0$) the square of the Scorer parameter can be approximated with the following expression. This is the case for waves that are generated by air flowing over variable topography (Whiteway, 1999).

$$\iota^2 \cong \frac{N^2}{U^2} \quad (2.30)$$

If the horizontal wavenumber is known for the gravity wave, ducted gravity waves can be found wherever $\iota^2 - k^2$ is approximately 0 (Trier & Sharman, 2018). Horizontal wavenumber can be determined based on the horizontal wavelength of the gravity wave,

$$k = 2\pi/\lambda \quad (2.31)$$

where λ is the horizontal wavelength in meters.

2.4.4 - Gravity Wave in Background Wind

In practice, gravity waves will be propagating while air is moving in the background. Gravity waves that appear to be moving with any arbitrary phase speed are actually moving at an intrinsic speed which is the difference between the phase speed of the wave and the component of the background wind in the direction of wave propagation (Nappo, 2013). Intrinsic speed is expressed by the following equation,

$$c_1 = c_{px} - u_0 \quad (2.32)$$

where c_{px} is the horizontal phase speed of the wave and u_0 is the background wind speed in the direction of wave propagation. The frequency of the wave appears as an intrinsic frequency which is quantified by the following equation. Both sides of equation 2.32 are multiplied by horizontal wavenumber (*k*). The equation for intrinsic frequency is

$$\Omega = \omega - u_0 k \, . \quad (2.33)$$

Intrinsic frequency takes the place of the wave frequency in the equation for vertical wavenumber (equation 2.27) the result is the following equation

$$m = \pm k \sqrt{\frac{N^2}{(\omega - u_0 k)^2} - 1} \, . \quad (2.34)$$

It is possible to let vertical wavenumber approach infinity if the intrinsic frequency approaches 0. The intrinsic frequency can be related to horizontal phase speed and when intrinsic frequency is set to 0 it will reveal which conditions cause an infinite vertical wavenumber.

$$\Omega = c_1 k = c_{px} k - u_0 k \quad (2.35)$$

$$0 = c_{px}k - u_0 k$$

$$0 = k(c_{px} - u_0)$$

$$c_{px} = u_0$$

Therefore, a gravity wave in a background wind will obtain an infinite vertical wavenumber whenever the horizontal phase speed of the wind is equal to the speed of the horizontal background wind. The altitude in the atmosphere where this occurs is called the critical level. As a gravity wave approaches the critical level its vertical wavenumber grows at a fast rate. This means the vertical wavelength of the wave is decreasing rapidly and the wave fronts begin to get squeezed together. The wave begins to dissipate and its energy is transformed into turbulence, this is also known as wave breaking, it is similar to ocean waves that break when they reach the coast (Nappo, 2013).

2.4.5 – Gravity Wave Breaking

It was stated in the previous section that a wave begins to break, overturn and dissipate into turbulence when the phase speed of the wave is equal to the speed of the horizontal background wind. Generally it can be shown that a wave is breaking and overturning if the wave induced a convectively unstable temperature gradient (Whiteway et al., 2003). The atmosphere was initially stable with a positive potential temperature gradient and the overturning wave flips the temperature profile so that potential temperature is decreasing with height. This is inducing convective instability in the atmosphere. The second sign of an overturning wave is that the horizontal wind

perturbation (u') will be greater than the phase speed of the wave (Whiteway et al., 2003). For a gravity wave that is propagating in horizontal background wind (u_0), the horizontal perturbation will need to be greater than the intrinsic phase speed (see equation 2.32 for intrinsic phase speed)

$$u' > c_{px} - u_0 \text{ .} \quad (2.36)$$

The amplitude of a breaking gravity wave will increase with height. Once the wave is above the level where it induces convective instability turbulence is generated and the wave breaks. Figure 2.6 contains observations from Aberystwyth, UK where vertically propagating gravity waves were generated by flow over nearby mountains (Whiteway et al., 2003). The Egrett research aircraft took measurements of vertical wind at horizontal flight legs. Flight leg F has the lowest altitude while flight leg A had the highest. The altitude of each flight leg from A-F is as follows, 13.2 km, 12.3 km, 11.4 km, 10.5 km, 9.6 km, and 8.4 km. The observations capture a gravity wave which increases in amplitude from flight legs F-C before it starts to overturn and breaks down into turbulence at the altitude of flight leg B. The breaking wave was found along flight leg C at -3.9^o longitude where the peak vertical wind perturbation was observed.

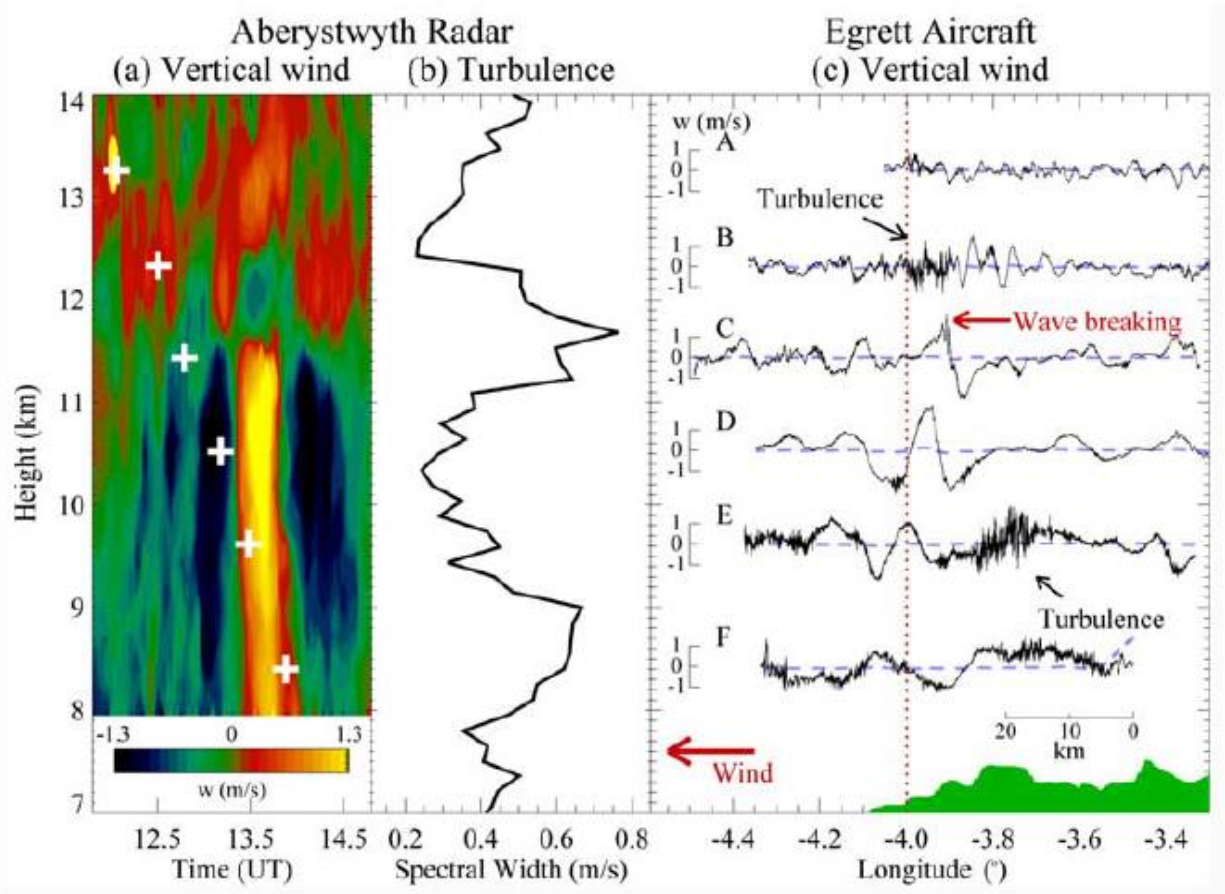

Figure 2.6: (a) Measurements of vertical wind by the Aberystwyth VHF radar. (b) The spectral width of the radar signal averaged between 12:30 and 01:00 UTC. (c) Vertical wind measured on the Egrett. Each flight leg is placed at its height relative to the vertical scale in (a). The topographic height below the Egrett track is shown in green at the bottom with the same relative vertical scale as in (a). The coast of Wales is at 4.1° longitude; the position of the Aberystwyth radar is indicated by the vertical dotted line at 4.0 ° longitude. Crosses in (a) indicate the time and height when the Egrett passed directly above the radar. Taken from Whiteway et al., 2003.

2.4.6 – Gravity Wave Momentum Transport

Gravity waves take horizontal momentum from the mean background wind and transport that momentum vertically through the atmosphere. This may also be referred to as wave stress (Nappo, 2013). The following equation is used to quantify wave stress which is denoted as $\tau(z)$

$$\tau(z) = -\rho_0 \overline{u'w'} \quad (2.37)$$

where ρ_0 is mean atmospheric density, $\overline{u'w'}$ is the vertical flux of zonal momentum, and the overbar denotes temporal spatial averages. If $\overline{u'w'}$ is positive then eastward momentum is being transported upward or westward momentum is being transported downward. If $\overline{u'w'}$ is negative then eastward momentum is being transported downward or westward momentum is being transported upward. For wave momentum transport in the meridional direction u' would be replaced by v'. Wave stress is constant with height unless the gravity wave is dissipating, which will occur when the gravity wave is breaking. Whenever there is a vertical gradient in the wind stress, momentum is transferred to the mean wind which will cause a change in the direction or speed of the mean wind (Nappo, 2013).

2.4.7 – Kelvin – Helmholtz Waves

Kelvin-Helmholtz waves develop in an environment where there is significant wind shear. Nappo developed a model to describe Kelvin-Helmholtz waves in which the atmosphere has neutral stratification and the atmosphere is assumed to be inviscid, irrotational, and incompressible. Lastly, the atmosphere is assumed to be in hyrdrostatic balance. The Kelvin-Helmholtz wave begins as a disturbance that causes vertical displacement of the interface between two atmospheric layers. The disturbance in the upper layer will push the interface upward while the disturbance in the lower layer will push the interface downward. This creates an interface that looks like a sinusoidal wave with a crest and a trough (Nappo, 2013).

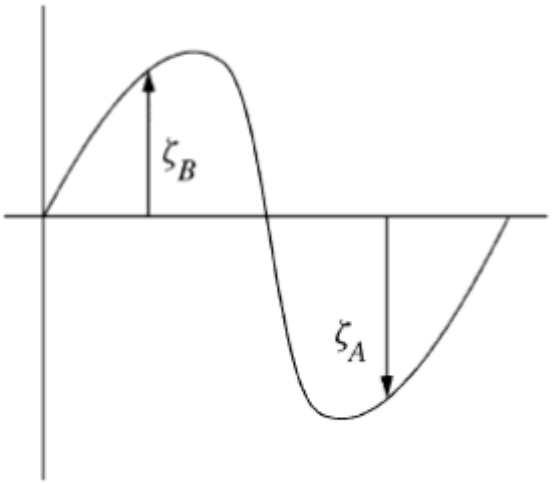

Figure 2.7: The interface displacement across the upper layer (layer B) and the lower layer (layer A) when a Kelvin -Helmholtz wave begins to grow. Figure taken from Nappo, 2013.

If the density of layer A is greater than the density of layer B the interface is convectively stable but if the density of layer B is greater than the density of layer A the interface is convectively unstable and the instability will cause the growth of the interface displacement. The mean flow in each layer push the top of the wave crests downstream and the Kelvin-Helmholtz wave appears to roll up which limits the vertical growth of the wave (Nappo, 2013). Kelvin-Helmholtz waves that are rolling up will appear as billow clouds just like what is shown in Figure 2.8.

Figure 2.8: Kelvin-Helmholtz waves that are in the process of breaking and overturning. Figure taken from Stull, 2020.

Once Kelvin-Helmholtz waves overturn they break down into turbulence just like other breaking gravity waves. The turbulence that is generated by breaking waves is able to cause mixing between layers A & B. This is important for the vertical transport of constituents in the atmosphere.

2.5 – Turbulence

2.5.1 – Properties of Turbulence

Turbulence can be described as random and irregular changes in the flow of a fluid caused by instability in the flow. There are many examples of turbulent flows such as the water flowing through a river, natural gas that is flowing through a pipeline, or a plume of smoke that is rising into the atmosphere. It is best to describe turbulence based on common characteristics that have been observed. The first characteristic of turbulence is its random and irregular nature (Tennekes and Lumley, 1972). In the case of atmospheric observations turbulent flows may

appear as random and irregular changes in the observed wind speed. A graph of the wind speed plotted with respect to distance or time may look like a series of random fluctuations when there is moderate or strong turbulence. Diffusivity is another aspect of turbulence. This is the rate at which different properties of the flow can spread or mix into other parts of the fluid. In the case of the atmosphere this is important for the transfer of heat, water vapour, ice crystals, momentum, atmospheric gases or other quantities that are able to spread throughout the fluid. Turbulence in the atmosphere is often the cause of mixing between two air masses.

Turbulence is characterized by high amounts of fluctuations in vorticity. The vorticity is only able to be sustained if there are velocity fluctuations in 3 dimensions. This means that turbulent flows must exhibit a high amount of vorticity fluctuations. If there are no vorticity fluctuations in the flow then it is not considered to be a turbulent flow. Turbulence is always dissipative and viscous shear stresses act on the fluid to increase the internal energy of the fluid while decreasing the kinetic energy of the turbulence. There must be a continuous supply of energy for turbulence or else the turbulence will dissipate rapidly (Tennekes and Lumley, 1972).

2.5.2 – The Spectrum of Turbulence

Larger turbulent eddies break down into smaller and smaller eddies (Kolmogorov, 1941). The energy is dissipated by the effects of viscosity once turbulent eddies are smaller than a critical size (MacCready, 1953). The energy for turbulent eddies is supplied by coherent structures such as waves. It was shown in section 2.4.5 that turbulence is produced when gravity waves break and overturn and in section 2.4.7 the same is occurring with Kelvin-Helmholtz

waves when the disturbance grows and the wave crests start to overturn turbulence is produced in the flow.

The kinetic energy spectrum of turbulence is a manifestation of the energy cascade from larger to smaller scales. This occurs as large structures dissipate into isotropic turbulence and the turbulence dissipates into heat. The total spectrum can be divided into 3 sections based on the movement of energy. The first section is the production region where the mean flow is adding energy into the system through shearing or buoyancy forces (MacCready, 1953).

The second region is the inertial-subrange where no energy is added by the mean flow and no energy is being taken away by viscous dissipation. There is a constant flux of energy from larger to smaller scales in the inertial-subrange. The energy spectrum for turbulence in the inertial subrange is given by the following equation,

$$E(k) = C_0 E_d^{2/3} k^{-5/3} \quad (2.38)$$

where $E(k)$ is the power spectral density in m^3/s^2, C_o is the Kolmogorov constant which is 0.5 for 1 dimensional spectra, E_d is the dissipation rate of turbulence kinetic energy in m^2/s^3 and k is wavenumber in m^{-1} (Tennekes & Lumley, 1972).

The turbulence kinetic energy dissipation rate can be used as an indication of the intensity of turbulence. If the dissipation rate is relatively high this means that turbulence kinetic energy is dissipating rapidly and it is an indication of intense turbulence. Lower dissipation rates are a sign that turbulence is not very intense and as a result energy is being transferred to smaller scales at a much slower rate.

The third region is the dissipation range, also known as the viscous subrange where viscous dissipation is taking energy out of the eddies and the eddies keep getting smaller until they completely dissipate into heat. Complete dissipation occurs when the wavenumber of the eddy is equal to the Kolmogorov microscale which is given by the following equation,

$$\eta = \left(\frac{\nu^3}{\varepsilon}\right)^{1/4} \quad (2.39)$$

where η is the Kolmogorov microscale, ν is viscosity of the fluid and ε is the average kinetic energy dissipation rate (Tennekes & Lumley, 1972). Figure 2.9 is a schematic of the spectrum of turbulence. The integral scale represents scales in the production region, the inertial scale represents scales in the inertial subrange and the Kolmogorov scale represents scales that are in the dissipation region or viscous subrange.

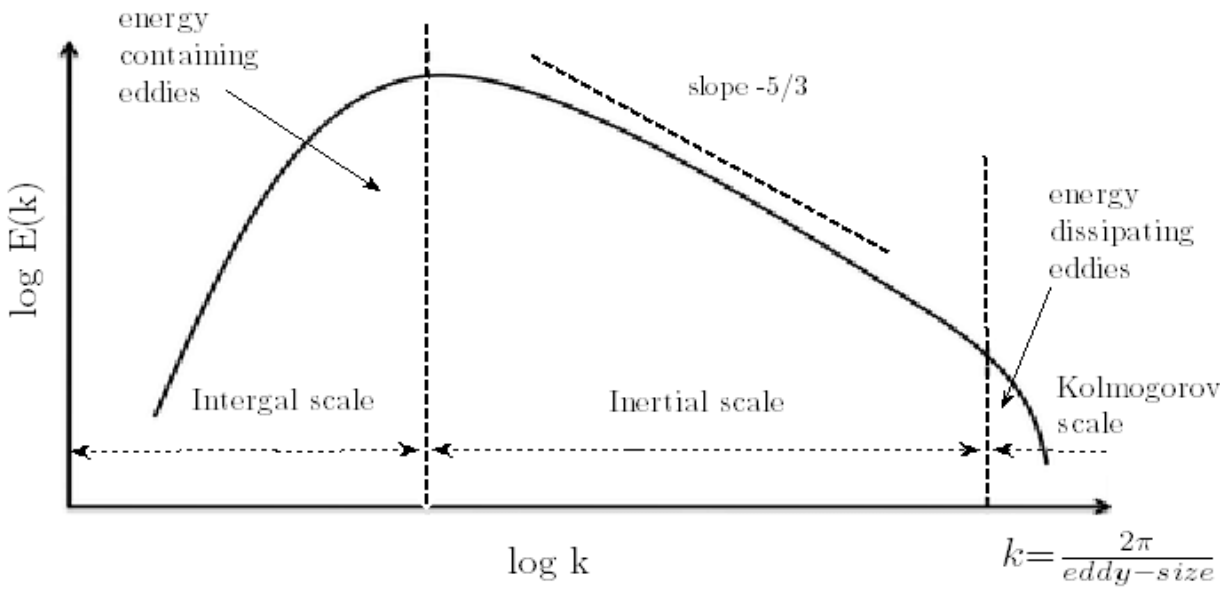

Figure 2.9: The energy cascade for eddies in a turbulent flow, coherent structures are associated with the integral scale, turbulence is found in the inertial scale. Taken from Sinha, 2013.

2.5.3 – Richardson Number

The Richardson number is a parameter that is defined as the ratio of the buoyant production to shear production of turbulent kinetic energy. (Tennekes and Lumley, 1972). It is given by the following equation,

$$Ri = \frac{N^2}{\left(\frac{\partial u}{\partial z}\right)^2 + \left(\frac{\partial v}{\partial z}\right)^2} \quad (2.40)$$

where N^2 is the static stability or the square of the Brunt-Väisälä frequency, u is the zonal wind and v is the meridional wind. Buoyancy is considered to be the stabilizing force while shear is the destabilizing force.

Turbulence may be observed in any situation where the stabilizing influence of buoyancy is small relative to the destabilizing force of shear. $Ri \leq R_c$ for a laminar flow to become turbulent. R_c is known as the critical Richardson number and it is estimated to be 0.25. Turbulence can be sustained if the Richardson number is less than 1 which means the influence of shear is larger than the influence of buoyancy. If $Ri \geq 1$ then turbulence cannot be sustained. Turbulent energy will dissipate, and the flow will become laminar (Hines, 1971).

2.6 – Cloud Dynamics

The following section will focus on the dynamics that were found to be occurring inside of the anvil cloud that was produced by the Hector thunderstorm on December 2nd, 2002. A powerful updraft at the surface causes air from the surface to rise up to the level of the tropopause. At the tropopause or a capping inversion some of the air continues to move upward

to create an overshooting top but generally the air separates into two branches. One branch travels in the same direction as the background wind and the other branch travels upstream, opposing the background wind. Air parcels that are moving in the direction of the background wind constitute the outflow jet which flows outward from the core of the thunderstorm. The outflow jet takes ice crystals from the top of the thunderstorm and blows them downstream creating a large anvil shaped cloud that extends dozens of kilometers away from the core of the thunderstorm (Krider, 1998). Figure 2.10 is a schematic of air motions in a strong thunderstorm, similar to Hector. Notice how updrafts of warm air rise upward through the core of the thunderstorms and then start to diverge at the tropopause. In this image, the background wind blows ice crystals from the top of the storm towards the right which creates the anvil cloud.

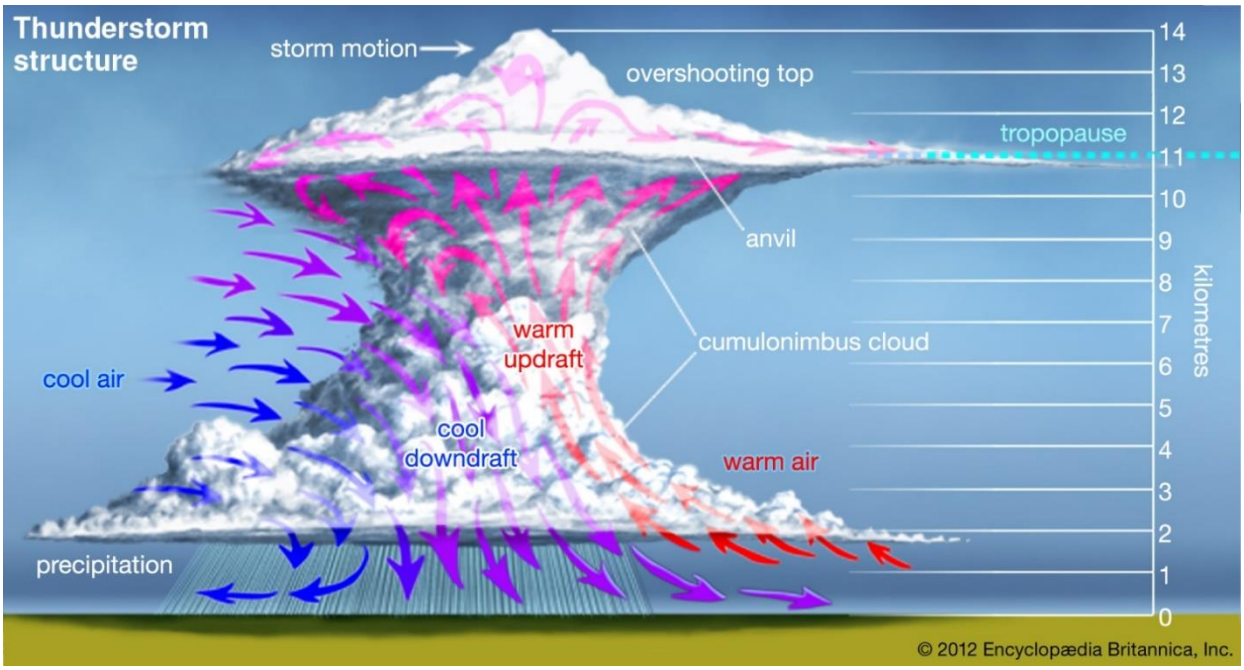

Figure 2.10: The structure of a typical thunderstorm and arrows that show the motion of air inside of a thunderstorm. Figure taken from Krider, 1998.

The dynamical phenomena that are typically found in the anvil outflow of a thunderstorm can include gravity waves, turbulence, and convective rolls. Both vertically and horizontally propagating internal gravity waves are observed in the environment of the anvil outflow region

of a thunderstorm (Trier et al., 2010; Lilly, 1983; Trier & Sharman, 2018). Internal gravity waves can be produced when deep convection in the overshooting top enters the lower stratosphere (Trier & Sharman, 2018). Internal gravity waves may become ducted if the environment of the anvil outflow creates conditions where gravity waves would be reflected. A wind jet or discontinuity in the temperature gradient can create a reflecting layer (Nappo, 2013).

Turbulence in the anvil outflow region of the thunderstorm is either driven by convective instability or shear instability. It is expected that convective instability generates turbulence close to the core of the thunderstorm while shear instability generates turbulence further downstream towards the edge of the anvil cloud (Lilly, 1983). Convective rolls in the anvil outflow may develop in a similar fashion to Rayleigh-Bernard convection. Usually the top of the anvil cools due to the release of IR radiation. The bottom of the anvil cloud warms as it absorbs IR radiation from the earth's surface. This creates a convectively unstable temperature gradient inside of the anvil cloud and convective cells develop (Trier et al., 2010).

2.7 - Mammatus Cloud Formation Theories

2.7.1 – Anvil Subsidence

The anvil subsidence mechanism was proposed by Wagner (1948), Ludlam and Scorer (1953), and Scorer (1958, 1972). It begins with saturated anvil air travelling horizontally over a layer of unsaturated air. There is a large moisture gradient between the anvil and the dry air underneath. The anvil cloud begins to sink due to sinking hydrometeors (Wagner, 1948; Martner, 1995; Platt et al., 2002), downdrafts that are compensating for the main updraft (Ludlam and Scorer, 1953), or because the cloud deck has reached the level of neutral buoyancy. The dry air begins to sink at the same time. The cloudy air is warming at the psuedoadiabatic lapse rate while

the dry air is warming at the dry adiabatic lapse rate (see section 2.3.3 for the lapse rates). The dry air underneath the cloud is warming at a faster rate than the cloudy air which creates a steep temperature gradient at the cloud base. Convective overturning will then cause parcels of cloudy air to descend below the base of the anvil cloud. These dropping parcels of cloudy air become mammatus clouds (Ludlam and Scorer, 1953).

2.7.2 – Subcloud Evaporation/Sublimation

This mechanism was proposed by Troeger (1922), Letzmann (1930), Hlad (1944), Ludlam (1948), and Scorer (1958). Water droplets, ice crystals or snowflakes fall from the anvil cloud into dry air below the cloud and frozen hydrometeors sublimate while the water droplets evaporate. Latent heat is transferred from the atmosphere to the hydrometeors which causes the temperature below the anvil cloud to drop. Air parcels in the lower part of the anvil cloud cool down and begin to sink until they reach their level of neutral buoyancy and at that point some of the air parcels that overshoot the equilibrium level rise upwards around the saturated air parcels to create a round mammatus lobe (Schultz et al., 2006). Figure 2.11 is a sounding from an environment that is suitable for sublimation or evaporation. From the 700 hPa level up to the 500 hPa level the dewpoint curve on the left and the temperature curve on the right are far apart but above 500hPa the dewpoint and temperature curves are closer together. A moist layer of air is sitting on top of air that is very dry.

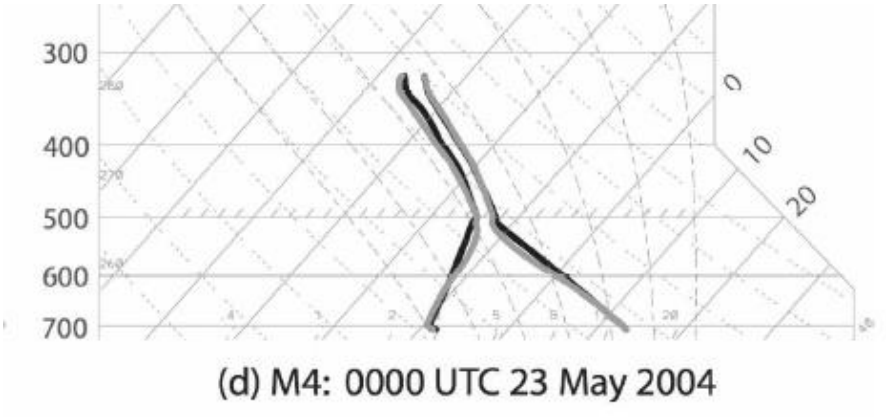

Figure 2.11: A Skew-T, log-P plot from an environment that is favourable for the sublimation of ice crystals. Taken from Kanak et al., 2008.

2.7.3 – Melting

Knight et al. (2004) noticed that the formation of mammatus clouds could be associated with a cloud base at an altitude below the freezing level. They proposed a mechanism, based on the suggestion of Findeisen (1940). Frozen precipitation falls out of the anvil cloud and melts. Latent heat is transferred from the atmosphere to the ice crystal or snowflake and this cools the environment. This causes an increase in the depth of the isothermal layer at 0^{o}C. The magnitude of the temperature gradient underneath the cloud increases as the environment near the cloud base cools off. Eventually the layer below the melting levels reaches saturation and convection can begin. This would mean the atmosphere is conditionally unstable. This can lead to the formation of mammatus if the cloud base is close to the freezing level (Findeisen, 1940; Stewart, 1984; Bosart & Sanders, 1991; Kain et al., 2000).

2.7.4 – Hydrometeor Fallout

This mammatus formation mechanism has been called the local scale hydrometeor fallout mechanism. Hydrometeors descend in lobes and evaporation or sublimation occurs which reduces the size of the hydrometeors and limits how far the lobe can descend. A baroclinic zone forms near the mammatus lobe due to the horizontal temperature gradient and the horizontal mass gradient. The temperature gradient is between the dry air where evaporation/sublimation is occurring and the saturated air inside the lobe. The mass gradient is caused by the hydrometeors inside of the lobe. As a result of the gradients, shear and curvature vorticity are occurring in the environment surrounding the lobe. Curvature vorticity leads to upward motion around the mammatus lobes (Scorer, 1958; Schultz et al., 2006).

2.7.5 – Cloud Base Detrainment Instability

Cloud Base Detrainment Instability (or CDI) is the theory created by Emanuel (1981, 1994) to explain the formation of mammatus clouds. CDI typically occurs when there is advection of cloudy air over clear air, as in the case of an anvil cloud. CDI is similar to entrainment instability that occurs at the cloud top but it is applied to the base of the anvil cloud. (Deardorff, 1980; Randall, 1980). The conditions for CDI can be quantified by using the vertical profile of liquid water static energy in the vicinity of the cloud base. Liquid water static energy is the work done on an air parcel when all of the liquid water in the air parcel is evaporated and the parcel is lowered adiabatically to a reference altitude. The CDI criteria is satisfied when liquid water static energy is higher in the sub-cloud layer than it is inside of the anvil cloud (Emanuel,

1981). This would correspond to a negative gradient in liquid water static energy across the cloud base. The equation for liquid water static energy is given below,

$$s_L = C_p T + gz - L_v w_L \quad (2.41)$$

where C_p is the specific heat of dry air as previously defined, T is the air temperature in Kelvin, g is the acceleration due to gravity as previously defined, z is the altitude in meters, L_v is the latent heat of vaporization, and w_L is the liquid water mixing ratio of the air (AMS, 2012). The anvil cloud from Hector was located above the freezing level so the cloud was composed of ice crystals. The static energy would need to account for the sublimation of ice crystals. The equation for ice static energy is the following,

$$s_i = C_p T + gz - L_s w_i \quad (2.42)$$

where L_s is the latent heat of sublimation, and w_i is the mixing ratio of ice.

The presence of CDI on its own will not produce mammatus clouds. Hydrometeors from the cloud must be mixed into the dry air underneath the cloud (Emanuel, 1981). The CDI formation mechanism does not explain how this happens. It is possible that dynamical processes that cause mixing will need to occur near the cloud base. (Schultz et al., 2006).

2.7.6 – Radiative Effects

There are three theories related to radiative effects that were discussed as possible formation mechanisms for mammatus. The top of the cloud will cool by emission of infrared radiation to space. The bottom will warm due to the exchange of infrared radiation with the

surface of the earth. Under these conditions the anvil cloud may act like a stratocumulus cloud which exhibits convection that is driven by cooling due to the emission of infrared radiation from the cloud top (Lilly, 1988; Wood, 2012; Schultz et al., 2006). The only difference is convection will begin at the base as well as the top. The mammatus lobes form due to convection at the cloud base.

The second mechanism was suggested by Plank et al (1955). Their mechanism starts with the emission of infrared radiation from the top of the cloud. This destabilizes the entire anvil cloud and causes deep vertical motion inside of the cloud. The mammatus clouds develop wherever there are downdrafts that penetrate the cloud base.

The third mechanism occurs with optically thick anvil clouds. Garett et al (2005) showed that longwave radiation from the surface only penetrates 100m into the cloud. The lower section of the anvil cloud becomes destabilized and convection occurs in the lower part of the cloud. Mammatus lobes develop from pockets of sinking air.

2.7.7 – Gravity Waves

Gravity waves were observed in the atmosphere while mammatus clouds were occurring. Gossard and Sweezy (1974) suspected that the gravity waves may help to release instability in the atmosphere which will cause convection and this can lead to the formation of mammatus. Yang and Houze (1995) and Pandya and Durran (1996) ran simulations of convective systems. They found gravity waves were able to modulate the base of the anvil cloud in a way that looked like mammatus but the waves were not on the same scale as mammatus clouds.

2.7.8 – Kelvin-Helmholtz Instability

Kelvin-Helmholtz waves were found to be associated with the development of mammatus clouds by Petre and Verline (2004). They were analyzing the atmosphere on the days when Jo et al. (2003) and Kollias et al. (2005) observed mammatus clouds. They observed Kelvin-Helmholtz waves in the vicinity of the cloud base at the same time the mammatus clouds developed. There are questions about the role Kelvin-Helmholtz waves may play since mammatus clouds do not appear to have the same scale or shape as billow clouds that form due to Kelvin-Helmholtz waves.

2.7.9 – Rayleigh-Taylor Instability

Rayleigh-Taylor instability was proposed as a mammatus formation mechanism by Agee (1975). Mammatus clouds would develop in the same way that plumes develop due to Rayleigh-Taylor instability. Figure 2.12 is a schematic of Rayleigh-Taylor instability. The upper layer denoted ρ_1 represents the cloudy anvil air while the lower layer ρ_2 represents the sub-cloud air.

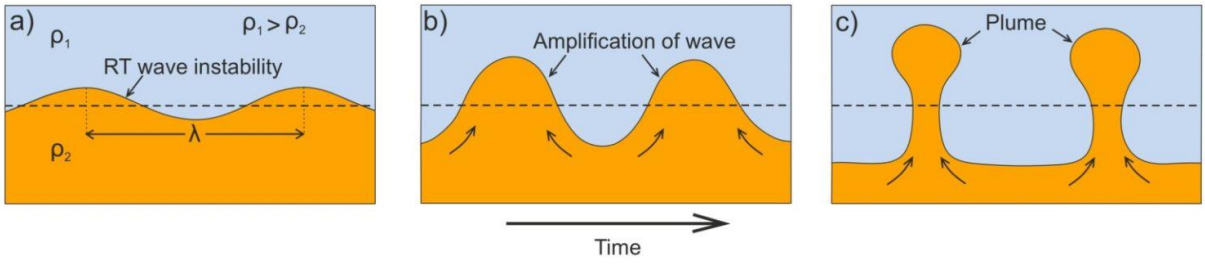

Figure 2.12: Rayleigh-Taylor instability for a high density fluid on top of a low density fluid. Figure taken from Ghosh, 2021.

The cloudy air would be considered to have a higher density than the sub-cloud air due to the mass of the hydrometeors. Rayleigh-Taylor waves begin to develop along the interface

between the cloud base and the dry air underneath. The amplitude of the waves begin to grow and the dry air will start to create plumes inside of the cloudy air. The mammatus cloud lobes would appear as the cloudy areas that were carved out by plumes of dry air due to Rayleigh-Taylor convection.

2.7.10 – Rayleigh-Bernard like Convection

Schaefer and Day (1981) proposed that mammatus clouds develop due to convection that is similar to Rayleigh-Bernard convection. Regular Rayleigh-Bernard convection occurs due to the heating of the lower boundary of a fluid or cooling of the upper boundary. Cellular convection develops as warm fluid parcels rise and cooler fluid parcels sink. Figure 2.13 is a schematic of Rayleigh-Bernard convection.

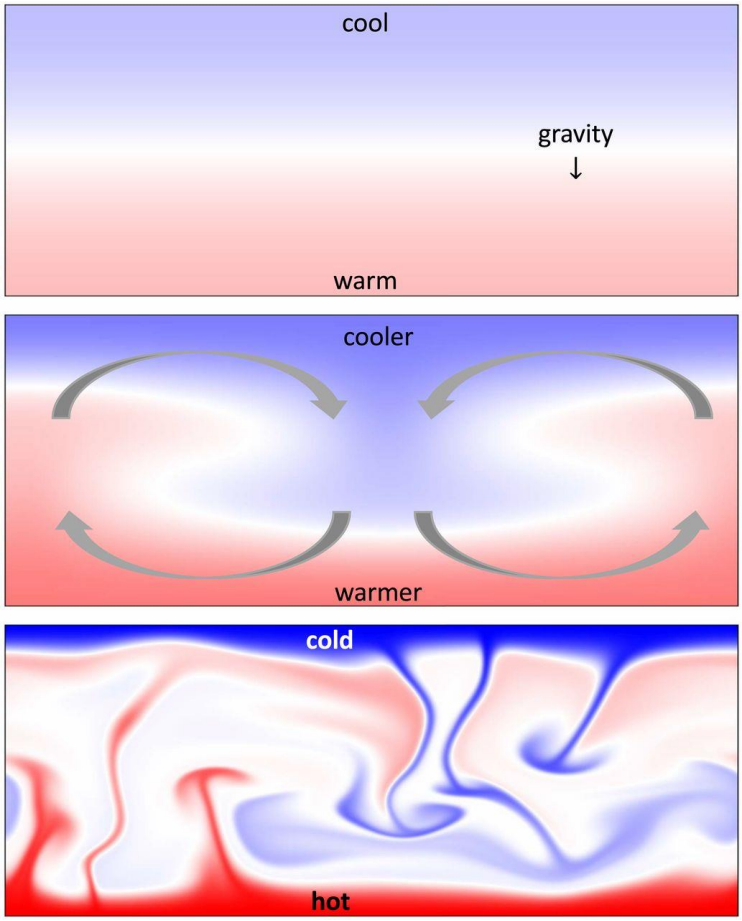

Figure 2.13: A schematic of Rayleigh-Bernard convection between two layers of fluid with a large temperature gradient. Taken from Doering, 2020.

The situation is reversed with the mammatus formation theory because the lower boundary, the cloud base is cooled by adiabatic cooling due to the vertical motion of air parcels. The lower boundary is not flat so theoretical Rayleigh-Bernard convection does not occur, this is why the theory is called Rayleigh-Bernard like convection (Schultz et al., 2006). The formation theory states that the cloudy air and the dry air below eventually reach the same temperature due to radiation and mixing. The cloudy air is unstable because of the combined weight of the cloud droplets and the falling air gets to divided into parcels of air that are like Bernard cells and these falling air parcels become the mammatus lobes (Schaefer & Day, 1981).

Chapter 3: Methods

3.1 – Measurements

3.1.1 – Aircraft & Equipment

Two research aircraft were used during the EMERALD research project. The first aircraft was the Grob T520 (known as the Egrett) which operates at altitudes up to 15 km and flies at air-speeds that range from 80-100 m/s. The second aircraft was the Beech 200T Super King Air (known as the King Air). This aircraft can operate at altitudes of up to 10 km. It flew in a matching flight pattern below the Egrett. Figure 3.1 is a picture of both the Egrett and the King Air.

Figure 3.1: The Egrett (top) and the King Air (bottom) the research aircraft that were used during EMERALD-2.

During the EMERALD research flights the Egrett was equipped with the following instruments.

- Cloud Particle Imager (CPI)
- Forward Scattering Spectrometer Probe (FSSP)
- Best Atmospheric Turbulence (BAT) Probe

- Rosemount Probe
- Frost Point Hygrometer (FPH)
- Tunable Diode Laser (TDL)
- Tropospheric Airborne Fourier Transform Spectrometer (TAFTS)
- TE-49C Ultraviolet absorption Spectrometer
- Novotel GPS
- INS

The King Air was equipped with the following instruments during the EMERALD campaign.

- 532nm polarization LIDAR
- Novotel GPS
- INS

5 different institutions collaborated to create and supply the instruments that would be used aboard the Egrett and the King Air.

- University of Wales at Aberystwyth (UWA)
- Airborne Research Australia (ARA)
- University of Manchester Institute for Science and Technology (UMIST)
- Deutsch zentrum für Luft und Raumfahrt (DLR)
- Imperial College London (IC)

The instruments, measured properties, and the supplying institution are outlined in Table 3.1.

Table 3.1: The instruments that were aboard the Egrett and the King Air.

Property Measured by the Instrument	**Instrument**	**Institution that Supplied the Instrument**
Cloud structure and optical properties	532nm, polarization LIDAR	UWA
Aircraft Position	Novotel GPS	ARA
Aircraft Attitude	INS	ARA
Ice Microphysics	Cloud Particle Imager (CPI) Forward Scattering Spectrometer Probe (FSSP)	UMIST
Air Temperature, Wind, Pressure	Best Atmospheric Turbulence (BAT) Probe Rosemount Probe	ARA
Water Vapour	Frost Point Hygrometer (FPH) Tunable Diode Laser (TDL)	DLR UWA
Far IR Spectra	Tropospheric Airborne Fourier Spectrometer (TAFTS)	IC
Ozone	TE-49C Ultraviolet absorption Spectrometer	DLR

3.1.2 – In Situ Measurements

The atmospheric properties that needed to be measured for this thesis were temperature, pressure, wind, water vapour, and cloud structure. This involves the use of the BAT probe, Rosemount probe, Frost Point Hygrometer, and Tunable Diode Laser. The LIDAR was used as well but this will be discussed in section 3.1.3. The BAT and Rosemount probes were mounted under the wings of the Egrett. A schematic of the BAT probe is presented in Figure 3.2.

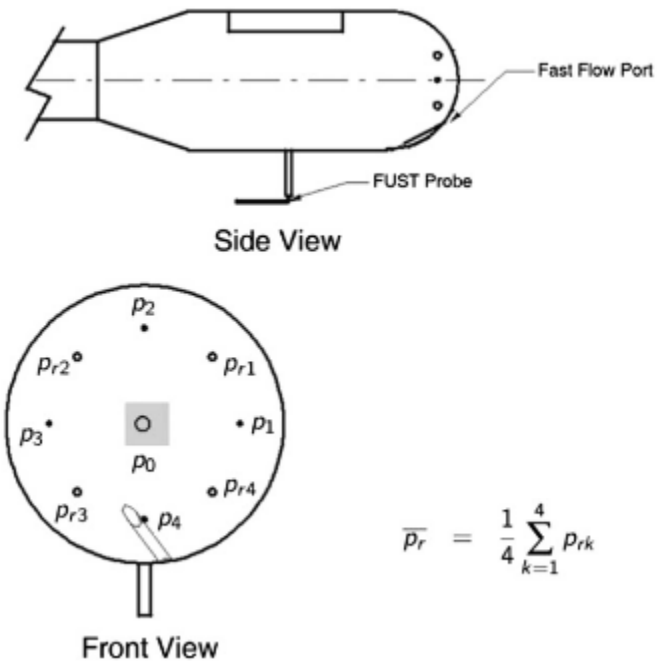

Figure 3.2: BAT probe schematic which shows the side view and front view of the probe. The front view shows each of the holes where pressure measurements are made. p_1, p_2, p_3, and p_4 are used to measure the direction and speed of the wind while the ambient pressure is the average of the pressure measurements from $p_{r1,}$ p_{r2}, p_{r3}, and $p_{r4.}$ The hole in the center p_0 measures the Pitot pressure and there is also a thermistor inside this hole to measure the temperature. Taken from Dobosy et al., 2013.

The BAT probe has 9 holes for pressure measurements, $p_{r1,}$ p_{r2}, p_{r3}, and p_{r4} are used for measuring the air pressure while $p_{1,}$ p_2, p_3, and p_4 are used for measuring the wind speed and direction. The ambient pressure is taken to be the average pressure measured in the 4 holes that are used to measure pressure. The temperature of the air is measured using a thermistor that is inside the central pressure hole, p_0 (Crawford & Dobosy, 1992). Wind speed and direction are determined by the distribution of pressure that is caused by the wind striking the head of the probe (Dobosy et al., 2013). This information is used to get the 3D wind vector relative to the sensor. The wind speed relative to the sensor is corrected for the velocity, acceleration and attitude of the aircraft. The wind velocity relative to the sensor is then added

to the velocity of the probe relative to the earth. The summation of these two vectors is taken to be the wind velocity vector (Crawford & Dobosy, 1997). The wind velocity vector consists of the zonal, meridional and vertical wind components. The Rosemount Probe uses the same techniques to determine the wind speed, temperature, and pressure. The only difference is that it contains 5 pressure holes instead of 9 (Wroblewski et al., 2010).

The Frost Point Hygrometer (FPH) contains a metal surface that is exposed to a stream of air. The metal surface cools down until a layer of dew or frost develops on the surface. The temperature of condensation or deposition is taken to be the dew point (or frost point if deposition occurs) temperature of the air (Hall et al., 2016).

The in-situ measurements for wind, temperature and pressure have a sampling frequency of 25Hz, assuming the speed the plane is 100m/s this corresponds to a horizontal sampling interval of 4m. The wind measurements have an uncertainty of ± 10 cm/s in the horizontal direction and ± 15 cm/s in the vertical direction. This is very small relative to the size of the wind speed measurements that have been documented in the thesis.

3.1.3 – LIDAR

The LIDAR was used for directing the flight path of the Egrett in real time during research flights. LIDAR data from the research campaign was used in this thesis as a visual tool that shows the structure of the clouds and the position of the Egrett relative to clouds. This is useful for figuring out where the Egrett encounters waves, turbulence, and changes in the state of the atmosphere.

The LIDAR works by emitting pulses of light into the atmosphere and measuring the amount of backscattered radiation. Photomultipliers are used to detect the incoming backscattered radiation and photon counting was used for signal acquisition. The backscattered radiation is recorded as a function of time, or equivalently distance. The LIDAR that was used onboard the King Air contains an Nd-YAG laser system (Whiteway et al., 2004a). The laser emits visible light with a wavelength of 532 nm, the pulse energy of the laser is 30mJ and the pulse repetition frequency for the beam is 20 Hz (20 pulses/s). The receiving system of the LIDAR contains a telescope with a diameter of 10 cm. Photon counting data acquisition had a vertical resolution of 30 m. An interference filter with a bandwidth of 1nm was applied to eliminate most of the background light. A beam splitter was used to divide the backscattered radiation into its parallel and perpendicular components relative to the radiation emitted from the laser. Figure 3.3 contains a schematic of the LIDAR system in (a), (b) is a picture of the LIDAR and its components at the University of Wales, Aberystwyth.

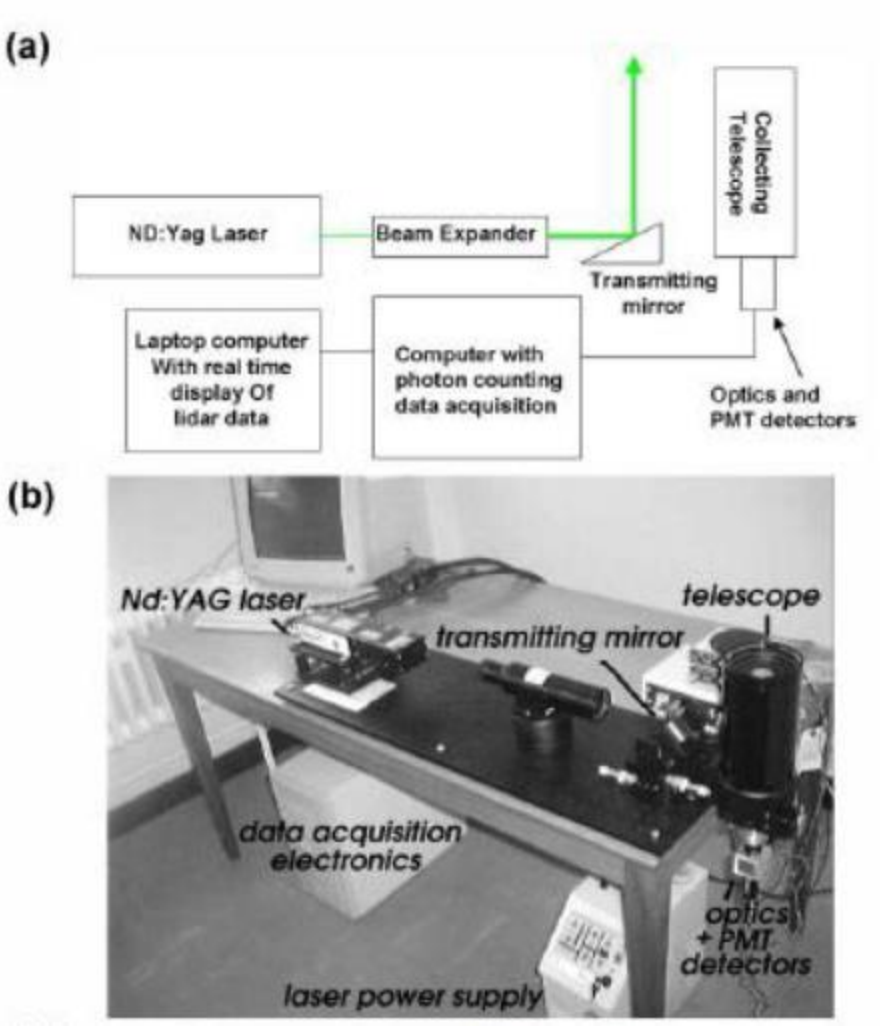

Figure 3.3: (a) Schematic diagram of the LIDAR employed aboard the King Air for the EMERALD 2 campaign. (b) Lidar system under construction in the lab at the University of Wales, Aberystwyth, taken from Lederman, 2015.

3.2 – Design of the Experiment

The campaign was carried out in November and December of 2002, when the isolated deep convection above the Tiwi Islands was active every day. The flight on December 2nd focussed on mammatus clouds. It consisted of 11 horizontal flight legs oriented parallel to the anvil outflow and stacked vertically. Satellite and radar data was provided by the Australian Bureau of Meteorology. This information was used to locate the anvil outflow and the core of the thunderstorm. It was important for making sure that the Egrett would not fly too close to the core

of the thunderstorm where it would encounter life threatening turbulence. Real time decisions for the flight patterns were made on board the King Air, based on the LIDAR measurements, visual survey, and the ground based radar images that were obtained from the Australian Bureau of Meteorology over a satellite telephone link. In each research flight the Egrett and the King Air would fly matching flight legs. The King Air was placed about 5km below the Egrett and it would collect LIDAR data of the cloud structure while the Egrett gathered data on the state of the atmosphere and its dynamical features. Table 3.2 contains the name, average altitude and the length of each flight leg on December 2nd.

Table 3.2: The name, average altitude and the length of each flight leg on December 2nd, 2002.

Flight Leg Number	Flight Leg Name	Altitude (km)	Length(km)
1	a13dn1	5.00	110.97
2	a13r1_322	10.37	170.55
3	a13r2_dn	12.56	151.14
4	a13r3_281	9.09	64.29
5	a13r4_dn	8.06	66.28
6	a13r5_230	7.44	66.36
7	a13r5_dn	7.12	10.47
8	a13r6_216a	6.96	76.63
9	a13r6_216b	6.97	32.79
10	a13r7_dn	9.11	69.33
11	a13r8_341	11.04	42.60

The base of the anvil cloud was at a height of approximately 8.0km in the vicinity of the mammatus clouds and the mammatus cloud lobes extend to a height of around 7.45km on average but some lobes have a base at an altitude of 6.8km based on LIDAR data. The base of the anvil cloud itself fluctuates greatly along its length. The base of the anvil cloud is usually at altitudes between 8 and 9 km based on the LIDAR. Figure 3.4 is a diagram of the position of the flight legs in the anvil outflow of the thunderstorm.

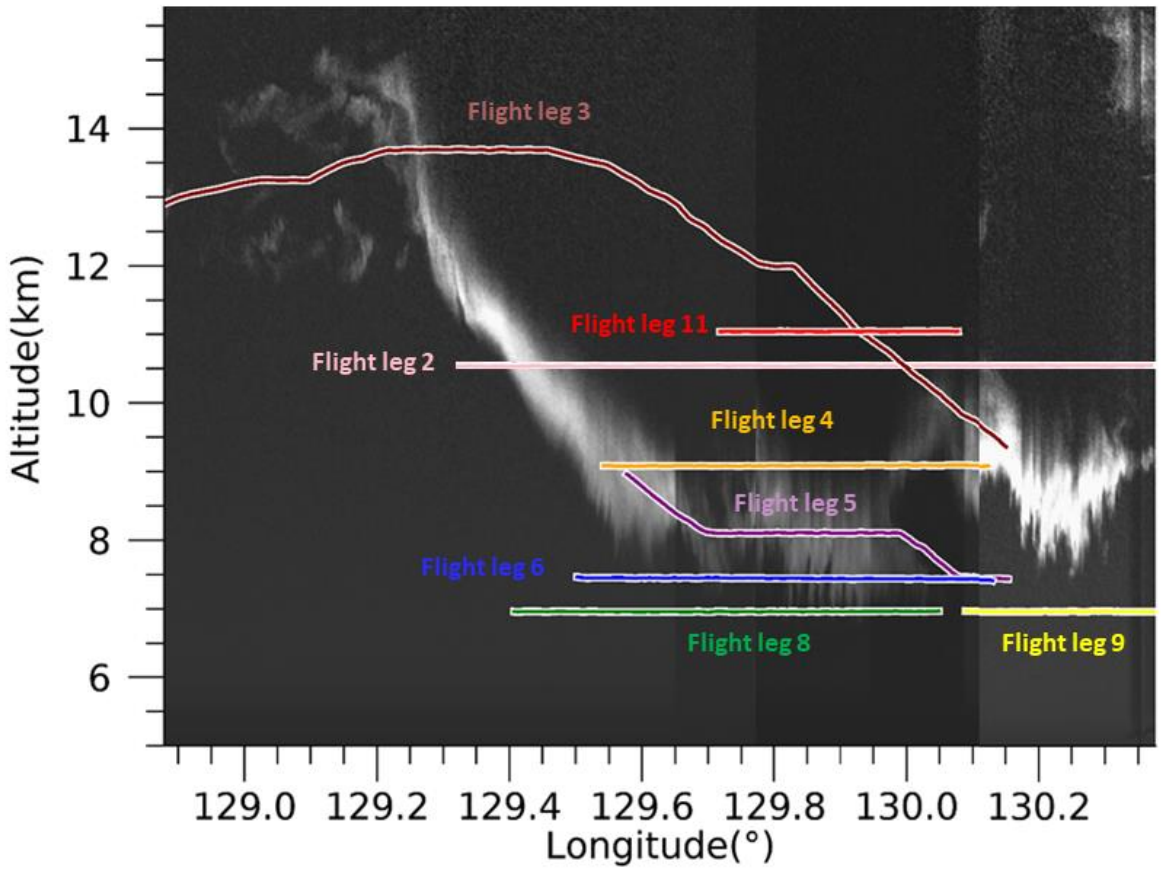

Figure 3.4: LIDAR image showing the anvil outflow region of Hector and the positions of some of the flight legs that were conducted in the vicinity of the mammatus clouds.

In each of the LIDAR images the anvil cloud appears to be thinner than it was in reality. This happens because the laser produced by the LIDAR cannot penetrate through the entire cloud. In most cases the laser travels up to 1.5km into the cloud before it is completely attenuated, but the cloud extended to heights of up to 15 km and above.

3.3 – Analysis of Turbulence Probe Measurements

3.3.1 – Reynolds Decomposition

Analysis of the data begins with Reynolds' decomposition. Each raw data point is treated as the sum of an atmospheric background value and the fluctuation or deviation from this background value

$$u(x) = \overline{u(x)} + u'(x) \quad (3.1)$$

where $u(x)$ represents the raw data, $\overline{u(x)}$ represents the atmospheric background value and $u'(x)$ is the fluctuation. The atmospheric background functions were calculated by fitting a set of overlapping cubic polynomials to the data. Each cubic polynomial was about 20 km (5000 points) long. The first point of each successive cubic polynomial was shifted by about 100 m (25 points) to the right of the starting point of the previous polynomial. This is repeated up to the end of the data set. The function that represents the atmospheric background value was determined by calculating the mean of the overlapping cubic polynomials. The fluctuations are the result of subtracting the background value from the raw data.

$$u'(x) = u(x) - \overline{u(x)} \quad (3.2)$$

Figure 3.5 is an example of the use of Reynolds' decomposition on the data from December 2nd, 2002. Figure 3.5(a) shows the potential temperature data for flight leg 5 with the atmospheric background plotted on top. Figure 3.5(b) shows the potential temperature fluctuations for flight leg 5.

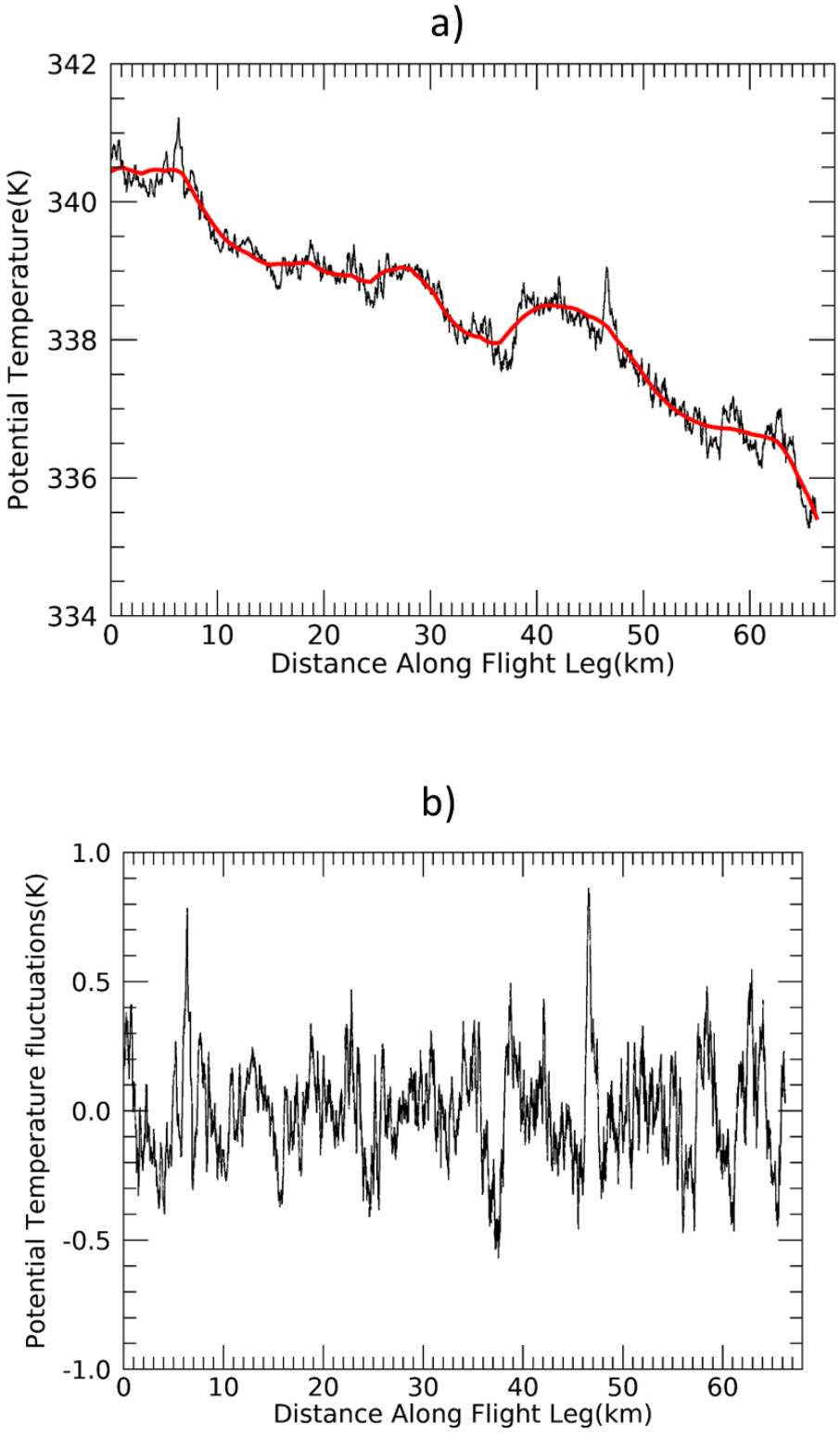

Figure 3.5: (a) Potential temperature data for flight leg 5 in black with the atmospheric background plotted on top in red. (b) Fluctuations in potential temperature for flight leg 5. The fluctuations are the result of subtracting the atmospheric background from the potential temperature data.

3.3.2 – Power Spectral Density

A power spectral density (PSD) shows how the perturbation variance is distributed over the wavenumber or wavelength scales that make up the signal (Brigham, 1988). In the case of wind speed fluctuations these scales represent the wavelength of the waves or the diameter of eddies and the magnitude of the PSD represents the amount of energy contributed from waves or turbulent eddies that can be resolved in the signal.

Before calculating the PSD a Hanning window was applied to the wind speed fluctuations and the Fast Fourier Transform (FFT) was applied to the windowed wind speed fluctuations. The FFT converts a function of distance into a function of wavenumber. The domain of the FFT extends from –Nyquist wavenumber to + Nyquist wavenumber. The Nyquist wavenumber is the largest wavenumber that can be resolved in the FFT without the issue of aliasing error. Nyquist wavenumber can be calculated with the following equation

$$k_n = \frac{1}{2\Delta x} \quad (3.3)$$

where k_n is the Nyquist wavenumber in m^{-1} and Δx is the horizontal sampling interval in m.

The positive wavenumbers form the first half of the FFT from a wavenumber of 0 up to the Nyquist wavenumber. This portion of the FFT is used for calculating the PSD. The following equation is used to calculate the PSD

$$S_{xx} = |FFT(X)|^2 \quad (3.4)$$

where S_{xx} is the power spectral density and *FFT (X)* is the fast Fourier transform of the dataset which is represented by X.

The PSD is normalized using Parseval's Theorem, the variance of the wind speed fluctuations is equal to the integral of the PSD. This is done by multiplying the PSD by a constant. The constant is the variance of the wind speed fluctuations divided by the integral of the PSD. The normalized power spectral density and the normalization constant are expressed by the following equation,

$$\hat{S}_{xx} = C|FFT(X)|^2 \quad (3.5)$$

$$C = \frac{var(X)}{\int(|FFT(X)|^2)} \quad (3.6)$$

where $\hat{S}_{xx}$ is the normalized power spectral density function and $\int(|FFT(X)|^2)$ is the integral of the un-normalized PSD.

3.4 – Analysis of Turbulence & Waves

The following section is a summary on the methods that were used to analyze turbulence and waves in the anvil outflow of Hector. The PSD which was discussed in the previous section has multiple applications to the study of turbulence and waves. The first thing it can be used for is determining how much energy in the flow comes from turbulence and coherent structures. The integral of the PSD over all coherent structure scales will produce the kinetic energy that is derived from coherent structures. In this case the coherent structures had scales at wavelengths between 250 m and 10 km (wavenumber range 0.1 – 4 km^{-1}) and the integral of the PSD between those scales is taken to be the coherent structure kinetic energy.

The scales of turbulent eddies range anywhere from 20 m to 250 m (wavenumber range 4 – 50 km^{-1}) based on the PSD function. Figure 3.6 is a sample PSD, the theoretical Kolmogorov spectrum has been plotted on top of the PSD in red. The wavelength (wavenumber) range where the Kolmogorov spectrum fits to the PSD is considered to be the scales of the turbulent eddies. Larger wavelengths (smaller wavenumbers) are considered to be the scales of the coherent structures such was waves and rolls.

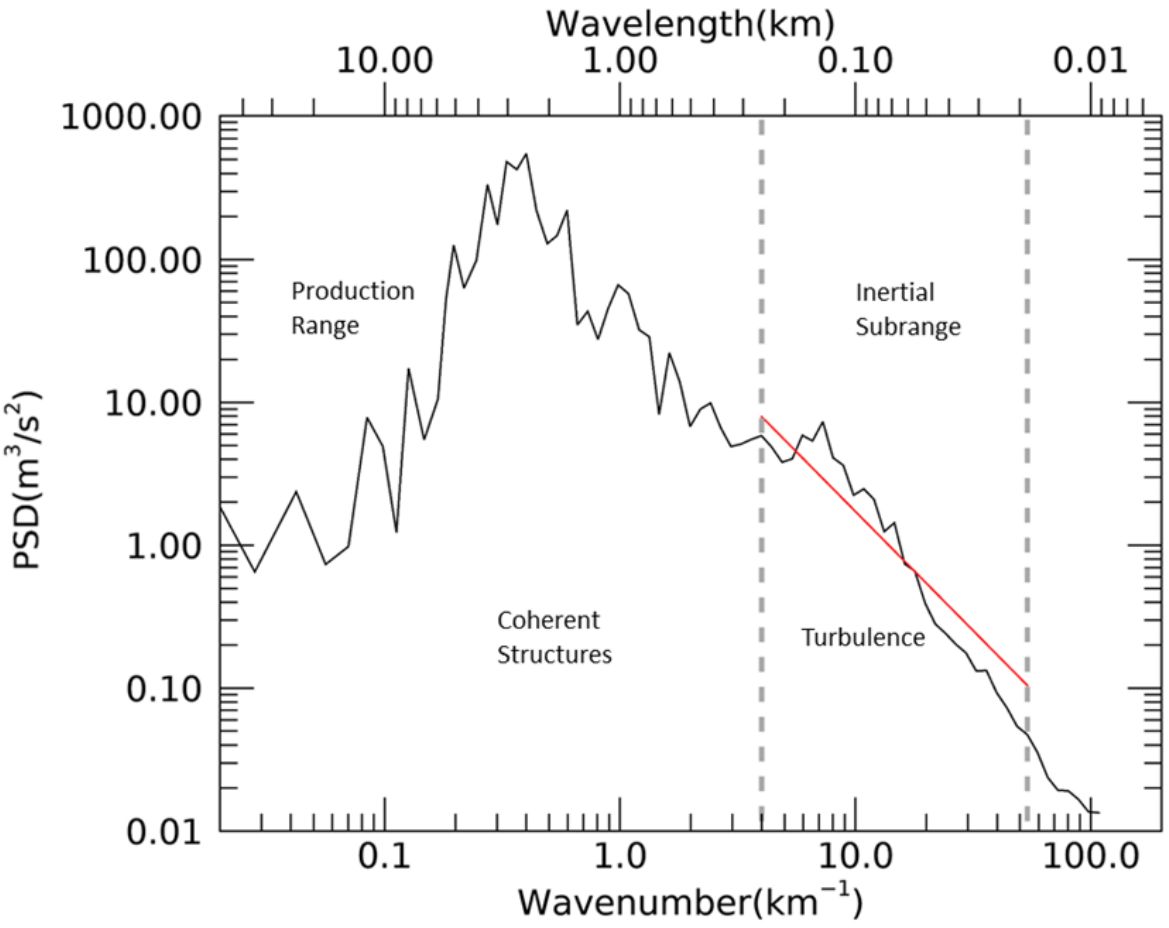

Figure 3.6: The PSD of vertical wind fluctuations from flight leg 5 with the Kolmogorov inertial subrange plotted on top of the PSD in red. The inertial subrange is the region of the PSD where the average slope is close to -5/3 on a log-log scale. Scales that are larger than the inertial subrange represent the scales of coherent structures.

The turbulence kinetic energy dissipation rate can be used as an indication of the intensity of turbulence. If the dissipation rate is relatively high this means that turbulence kinetic energy is

dissipating rapidly and it is an indication of intense turbulence. Lower dissipation rates are a sign that turbulence is not very intense and as a result energy is being transferred to smaller scales at a much slower rate. The dissipation rate can be solved by fitting a line that has a slope of -5/3 to the inertial subrange of the power spectral density on a log-log axis (x and y axis have a logarithmic scale). This is based on equation 2.38 which represents the Kolmogorov energy spectrum for the inertial subrange ($E(k) = C_0 E_d^{2/3} k^{-5/3}$).

A vertical profile of the Richardson number is another tool that is used to analyze turbulent flow in the atmosphere. When greater than zero, the magnitude of the Richardson number is used to identify areas where there is potential for the generation of turbulence by shear instability (i.e. *Ri* less than 0.25). If the Richardson number is less than zero there is buoyant instability. The momentum fluxes, and coherent structure are useful for analyzing the areas of the atmosphere where coherent structures were most active.

Chapter 4: Results & Analysis

The results of the experiment and an analysis of the data are presented in this chapter. Data from 11 legs of the flight on December 2nd, 2002 have been plotted with respect to altitude and distance in order to analyze the overall state of the atmosphere and the dynamical processes. The vertical profiles for atmospheric state variables such as temperature, moisture, and wind components have been designed by taking all data points from the flight legs and sorting the data according to altitude. This was done for each variable that required a vertical profile. The Richardson number and Scorer parameter profiles were derived based

on the vertical profiles of the state variables. These vertical profiles concentrate on the lower part of the anvil outflow between the altitudes of 5.9 km and 8.9 km.

The momentum fluxes, coherent structure energy and turbulence dissipation rate profiles were constructed in a different way. The vertical profiles are based on the average value of the variable across each of the 11 flight legs. The average value is plotted at the height that represents the average altitude of the flight leg. It took almost 4 hours to complete all 11 flight legs and there were variations in the cloud structure as the Egrett flew across the anvil outflow. The structure of the anvil cloud was changing over this period of time. Data points from flight legs close to the top of the anvil cloud were sampled earlier than the data points from flight legs in the lower part of the anvil outflow as a result there is some uncertainty in the exact trend between observations in the upper anvil and the lower part of the anvil. The averaging accounts for any variations which occurred across the flight leg.

The vertical profiles are used to analyze changes in atmospheric properties that may have an impact on the formation of mammatus clouds. The mammatus clouds that are the focus of the study developed along the bottom of the anvil cloud. The Egrett passes right through the mammatus clouds along flight leg 5. Figure 4.1 is a LIDAR image from flight leg 5, the mammatus clouds have been identified and labelled in this figure.

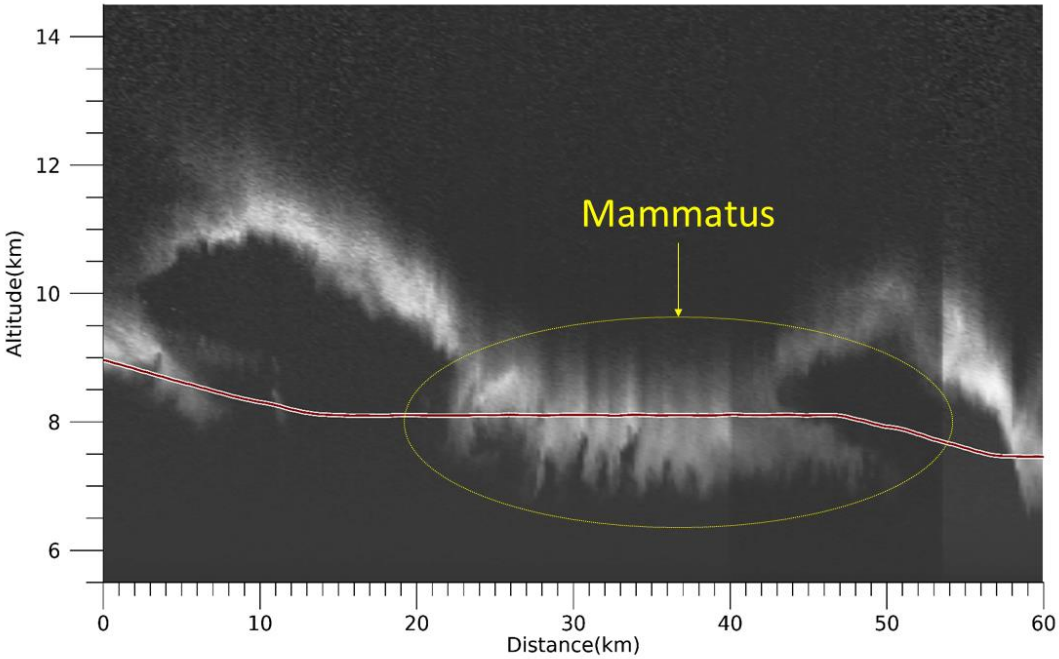

Figure 4.1: LIDAR image from flight leg 5 with the track of the Egrett plotted on top in maroon. The mammatus clouds are inside of the yellow oval.

It is important to note that the base of the anvil cloud was not always at a constant altitude. There were wave-like undulations in the cloud base. The Egrett passes through the cloud base at more than one height, most of the horizontal flight legs pass through the base of the anvil cloud. This occurs in flight leg 2, flight leg 4, flight leg 5, flight leg 6, and flight leg 8. The first section of results focuses on some of the dynamics that are encountered along 8 of the 11 flights that were conducted on December 2nd, 2002.

4.1 - Dynamics in the Anvil Outflow

4.1.1 - Vertical Wind Fluctuations

Figures 4.2-4.9 are the vertical wind fluctuations plotted on top of the LIDAR data for flight leg 2, flight leg 3, flight leg 4, flight leg 5, flight leg 6, flight leg 8, flight leg 9 and flight leg 11 respectively.

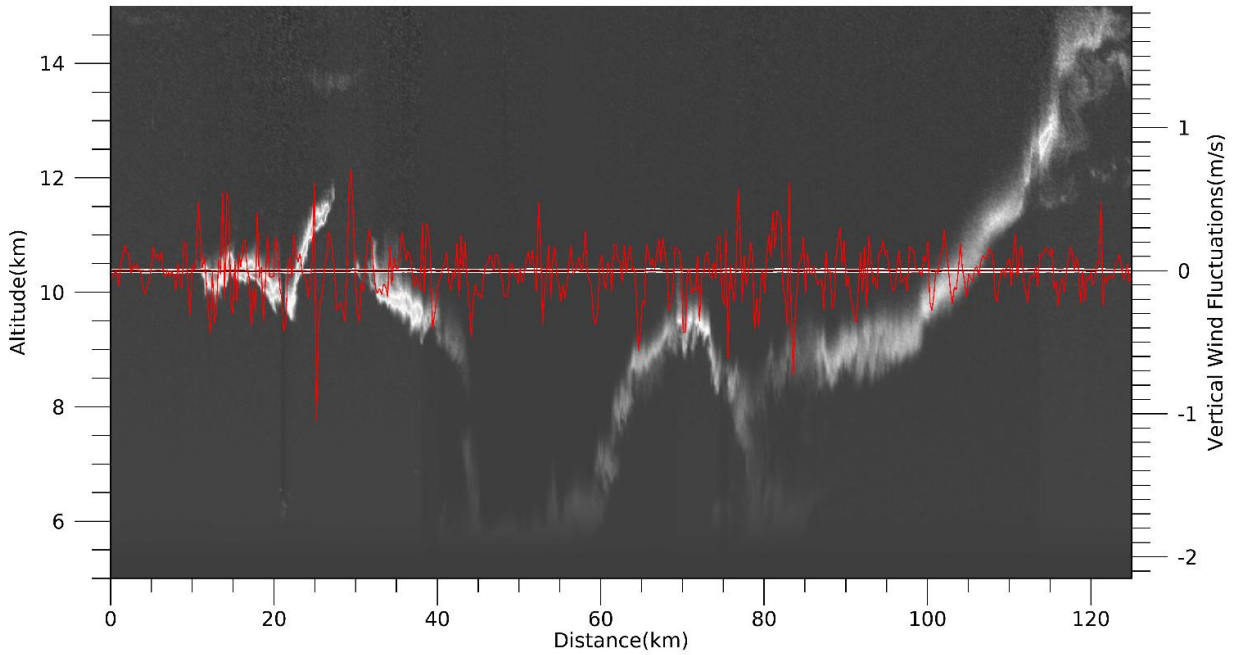

Figure 4.2: Vertical wind fluctuations (red) plotted on top of the LIDAR signal for flight leg 2.

The Egrett was flying through coherent structures during the first 10km of the flight. Then from 10 km to 28 km the Egrett passed through a patch of light turbulence. From 28 km up to 35 km there was another area of coherent structures and there was isotropic turbulence from 35 km to the end of the flight.

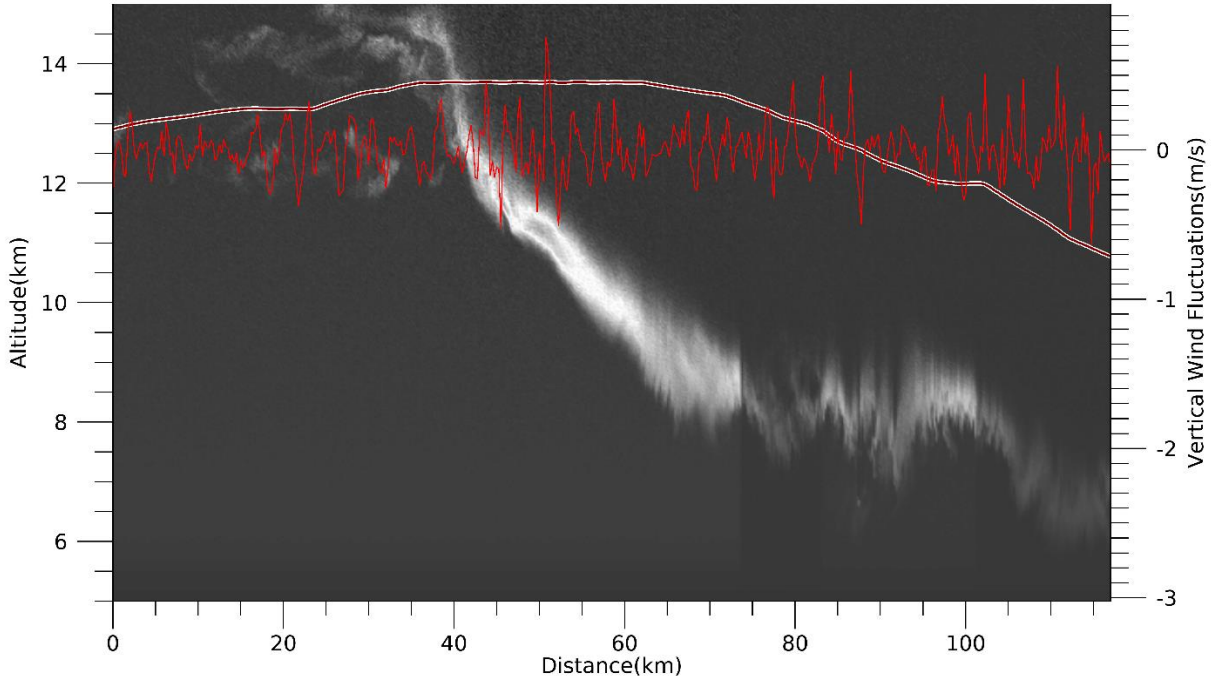

Figure 4.3: Vertical wind fluctuations (red) plotted on top of the LIDAR signal for flight leg 3.

Along flight leg 3, the Egrett was flying through coherent structures for the majority of the flight. There was a patch of isotropic turbulence starting at around 110 km into the flight, the turbulence continued to the end of the flight leg.

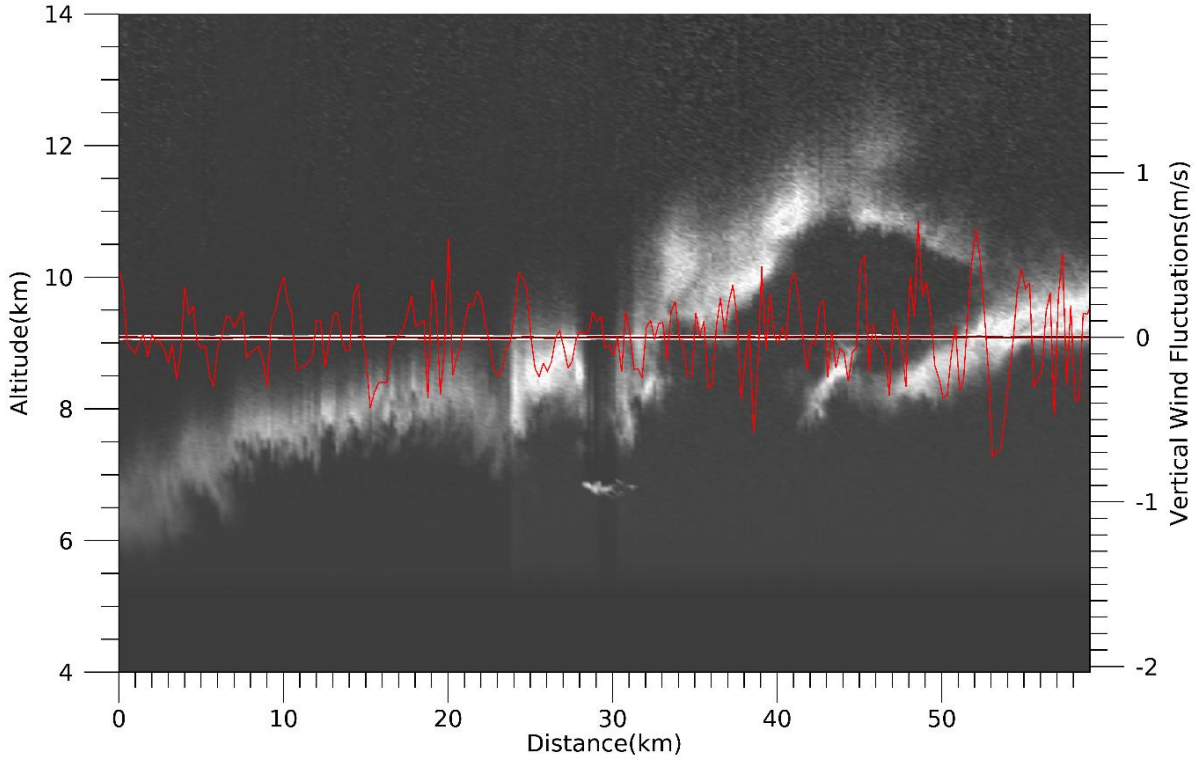

Figure 4.4: Vertical wind fluctuations (red) plotted on top of the LIDAR signal for flight leg 4.

There were coherent structures all along the length of flight leg 4. In between these coherent structures the Egrett encountered some patches of turbulence.

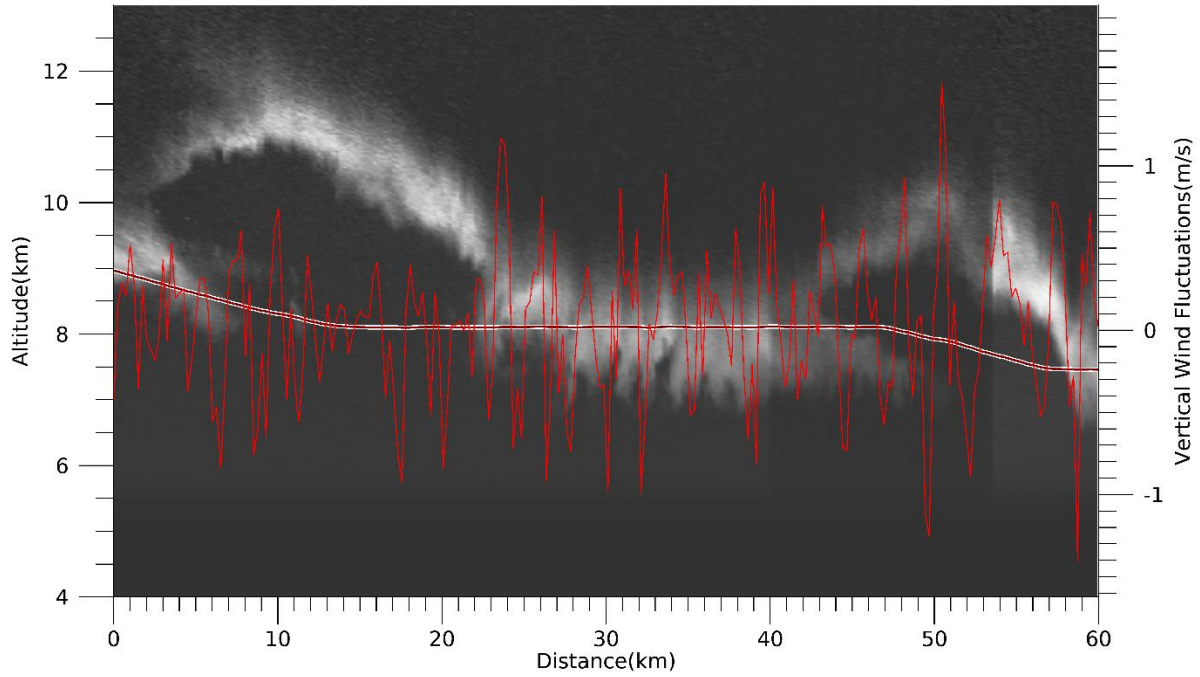

Figure 4.5: Vertical wind fluctuations (red) plotted on top of the LIDAR signal for flight leg 5.

Flight leg 5 was similar to flight leg 4, the Egrett was flying through coherent structures along the entire length of the flight leg. Patches of isotropic turbulence were observed at a few locations along the flight. Notably 0-5 km, 18-22 km, and 35-37km.

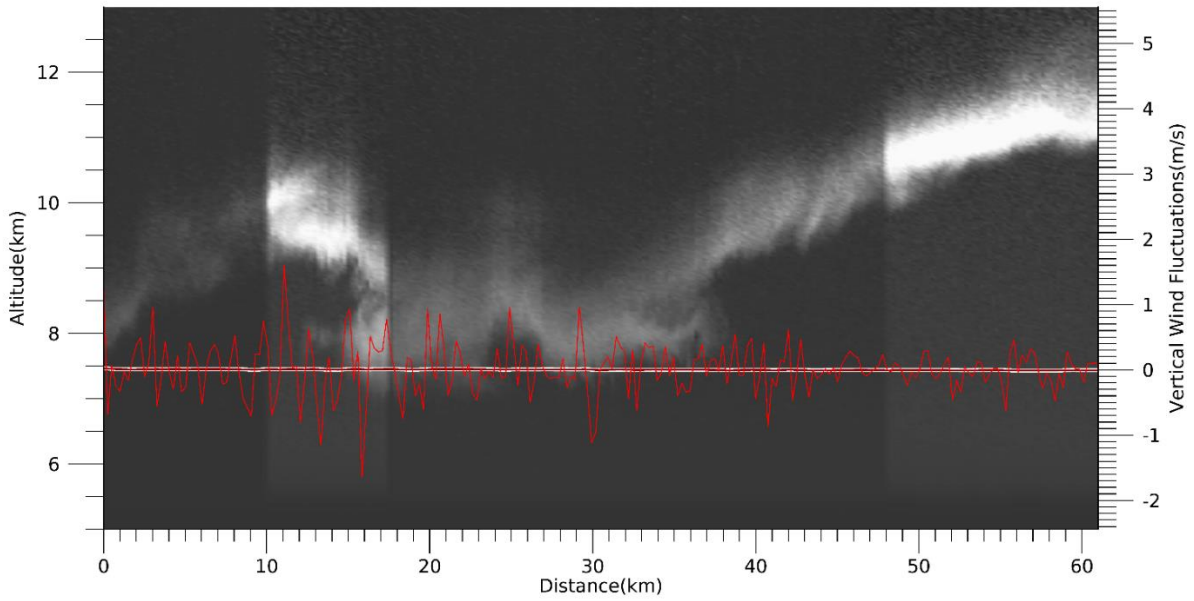

Figure 4.6: Vertical wind fluctuations (red) plotted on top of the LIDAR signal for flight leg 6.

There were coherent structures along the entire length of flight leg 6, some patches of turbulence were observed in between the coherent structures.

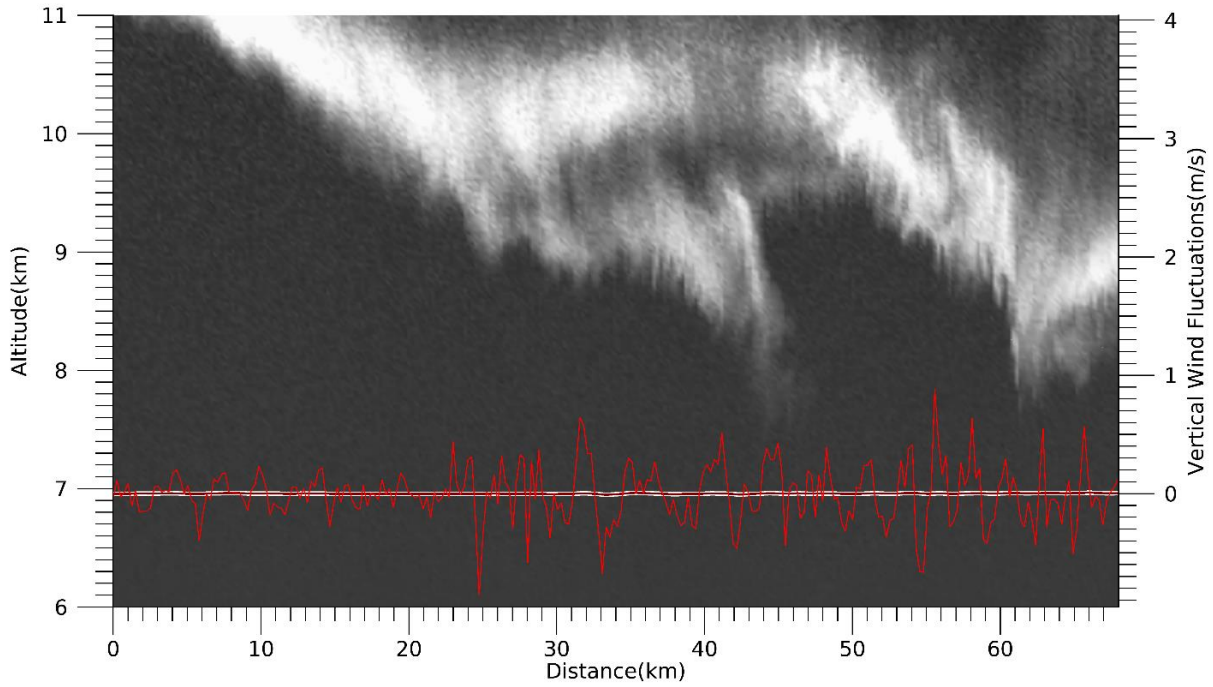

Figure 4.7: Vertical wind fluctuations (red) plotted on top of the LIDAR signal for flight leg 8.

The Egrett passed through coherent structures for most of the flight, there was a notable coherent structure is approximately 34 km into the flight. This appears to be a breaking wave and it will be studied in more detail in section 4.3.4. Isotropic turbulence was observed in between the coherent structures including a larger patch of turbulence form 10-32km.

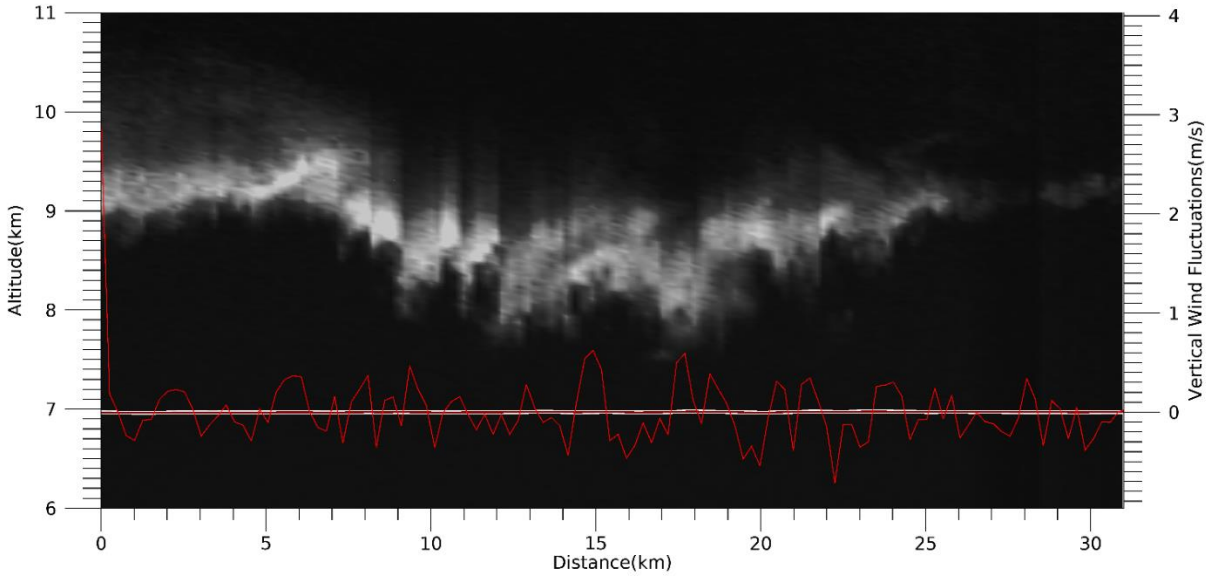

Figure 4.8: Vertical wind fluctuations (red) plotted on top of the LIDAR signal for flight leg 9.

Some sections of flight leg 9 were areas of isotropic turbulence while other sections contained a series of coherent structures. The sections with isotropic turbulence were found at 7-12 km and from 22.5 km to the end of the flight. For the first 7 km of the flight the Egrett passed through a series of a coherent structures. There was a second section of coherent structures from 12-22.5 km.

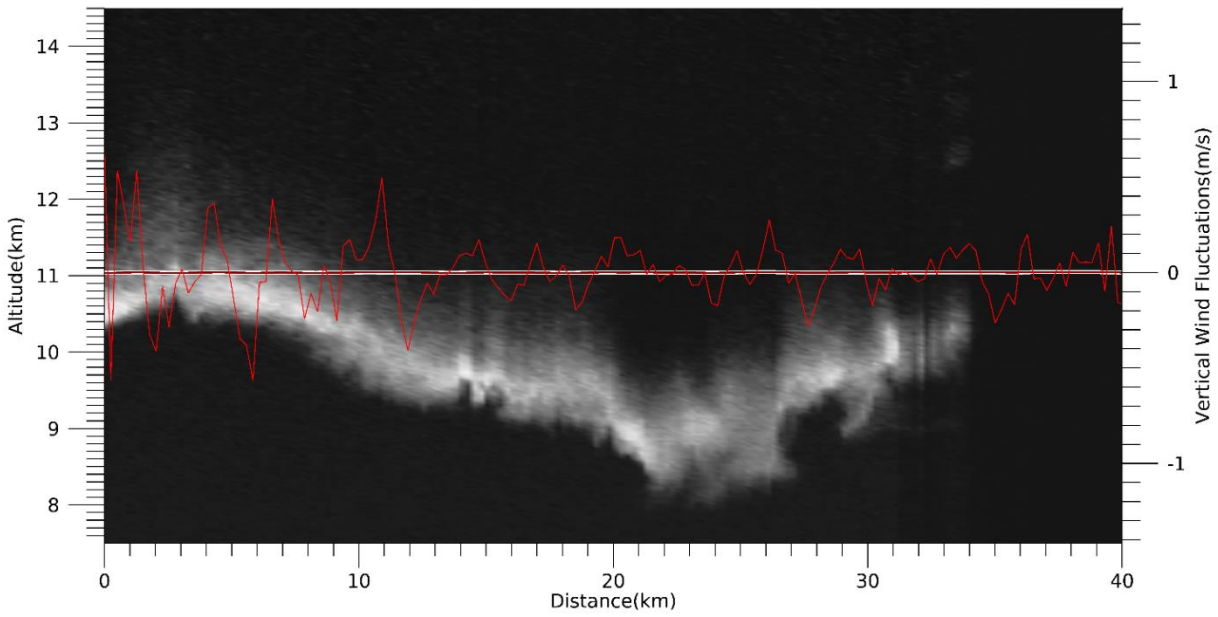

Figure 4.9: Vertical wind fluctuations (red) plotted on top of the LIDAR signal for flight leg 11.

Coherent structures can be found along the entire length of flight leg 11. There was some isotropic turbulence located between the 8 and 13 km mark.

4.1.2 - Intensity of Turbulence

Figures 4.10-4.17 are the eddy dissipation rates from the PSD of the vertical wind fluctuations. This has been plotted on top of the LIDAR data for their respective flight leg and it is used to estimate the intensity of the turbulence. The criteria for the intensity of turbulence is based on the work of Lane & Sharman (2014) and Trier & Sharman (2018). Eddy dissipation rates of 1.25×10^{-4} - 8.0×10^{-3} m^2s^{-3} are associated with light turbulence, eddy dissipation rates of 1.0×10^{-3}- 0.064 m^2s^{-3} are associated with moderate turbulence and eddy dissipation rates that are greater than 0.064 m^2s^{-3} are associated with heavy turbulence.

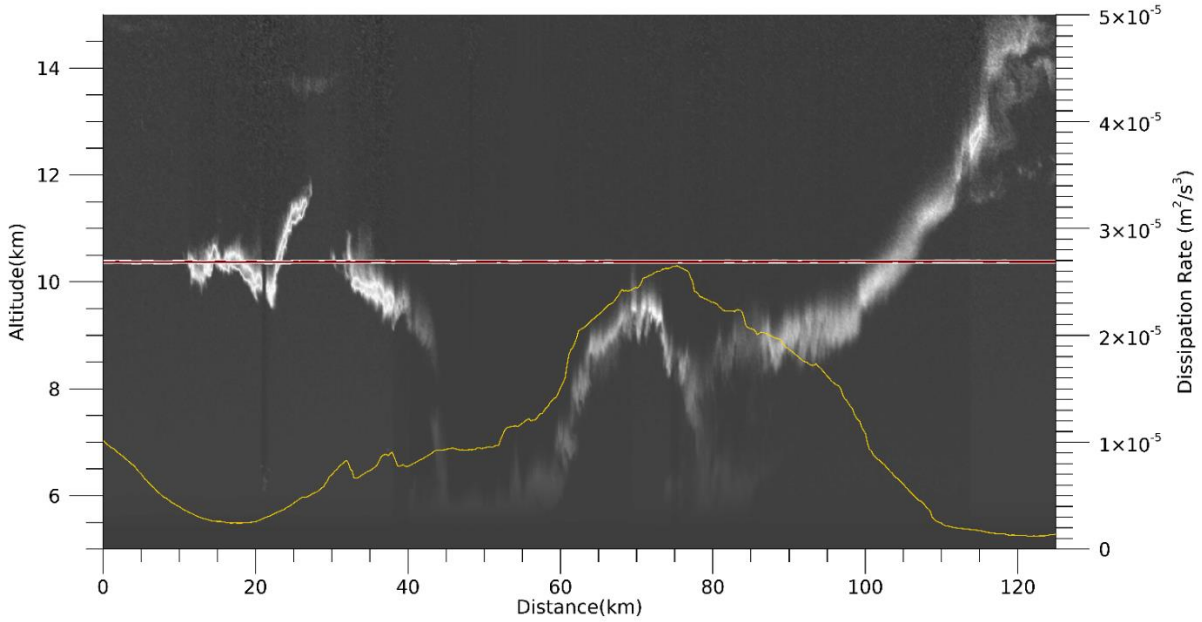

Figure 4.10: Eddy dissipation rate for *w'* (gold) plotted on top of the LIDAR signal for flight leg 2.

Light turbulent flow was observed along flight leg 2. Generally, the dissipation rate is higher inside of the anvil cloud (between 30 km and 105 km) than it is in the areas that are outside of the cloud.

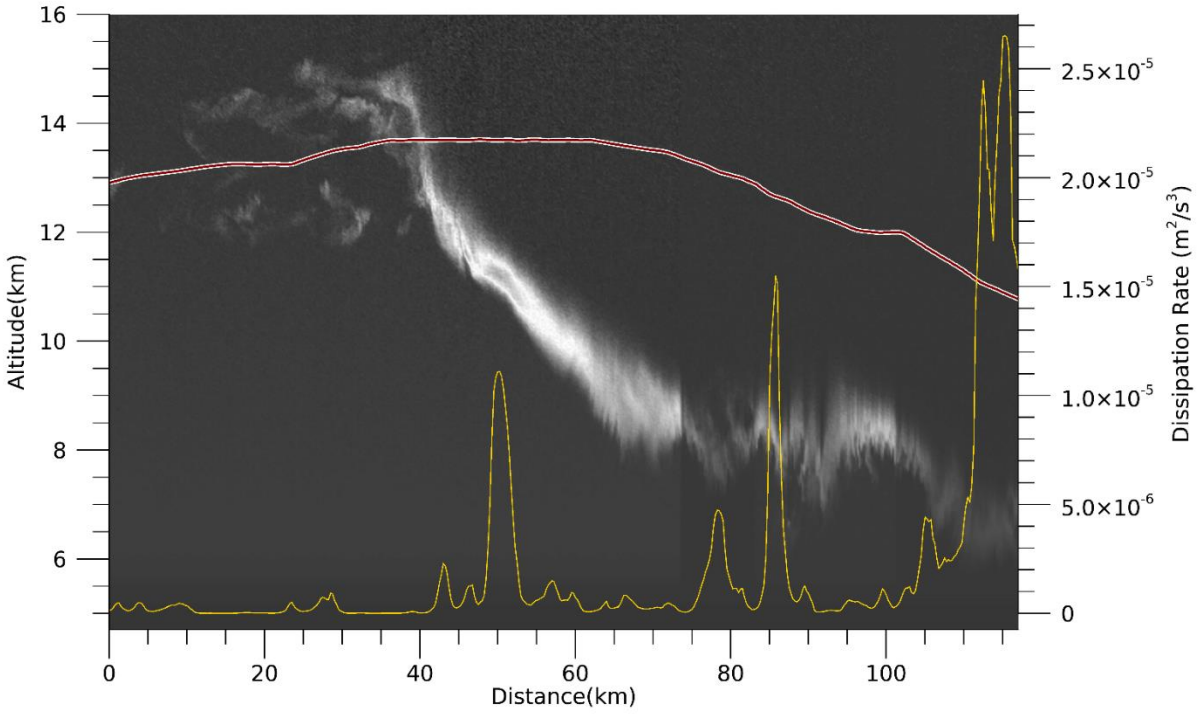

Figure 4.11: Eddy dissipation rate for *w'* (gold) plotted on top of the LIDAR signal for flight leg 3.

Light turbulent flow is observed along flight leg 3. There is very little turbulence along the edge of the anvil cloud where the dissipation rate is essentially 0. The dissipation rate increases with distance as the Egrett was flying into the interior of the anvil cloud and dropping to lower altitude.

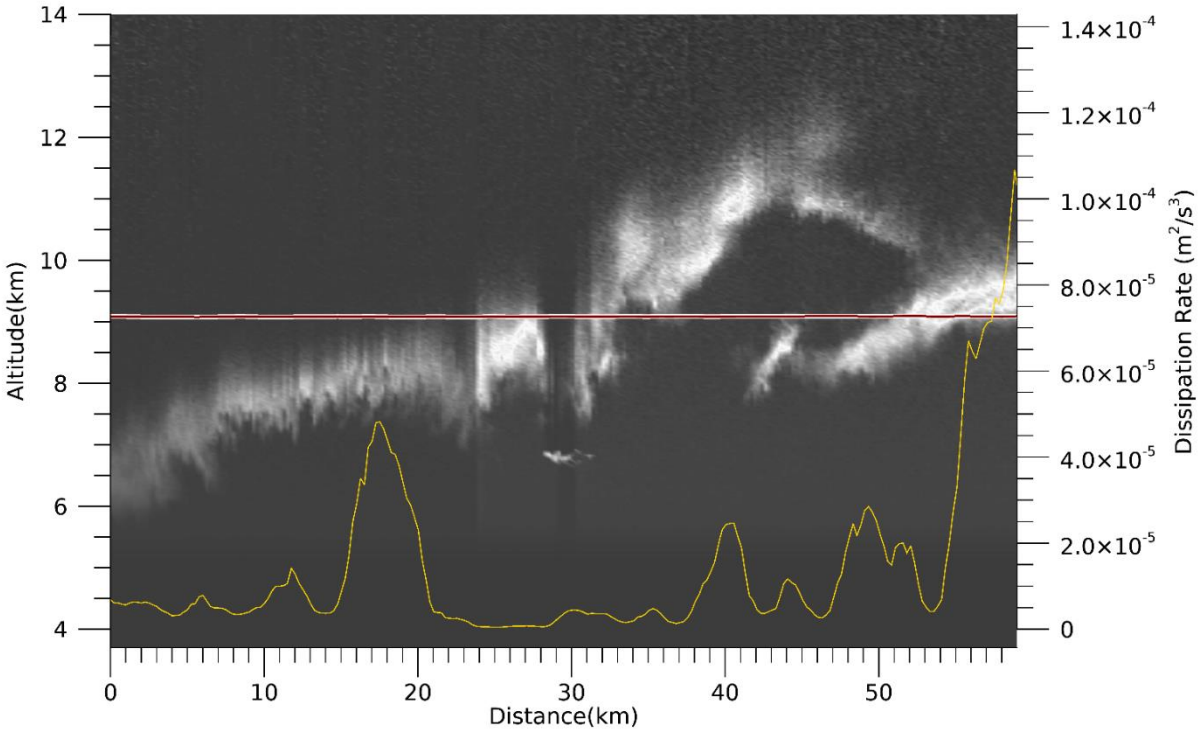

Figure 4.12: Eddy dissipation rate for *w'* (gold) plotted on top of the LIDAR signal for flight leg 4.

Light turbulent flow was observed along flight leg 4. There are a few notable peaks in the dissipation rate along the flight. These peaks occur at the following locations along the flight 16-21 km, 40-42 km, 47.5-52 km, and 55-59 km.

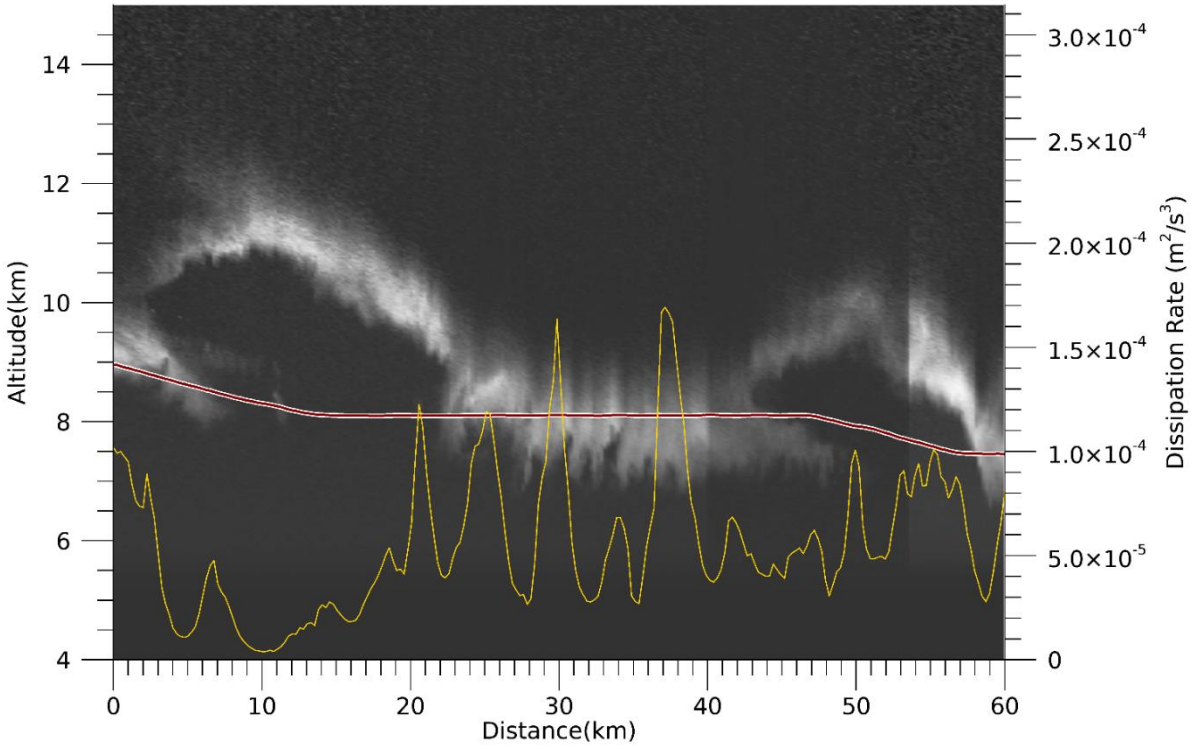

Figure 4.13: Eddy dissipation rate for *w'* (gold) plotted on top of the LIDAR signal for flight leg 5.

The flow along flight leg 5 contained light turbulence. On average the magnitude of the dissipation rate is highest in the vicinity of the mammatus clouds. The mammatus clouds were observed in the part of the flight with the highest average dissipation rate.

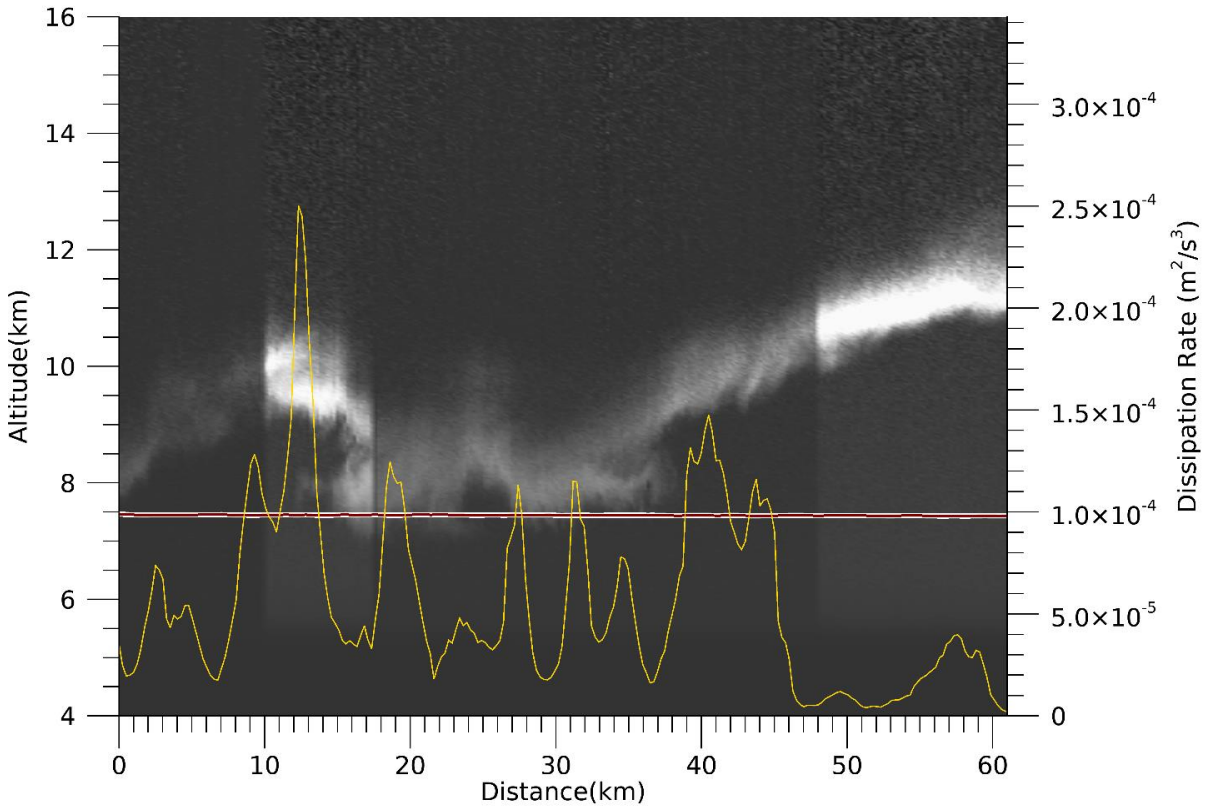

Figure 4.14: Eddy dissipation rate for *w'* (gold) plotted on top of the LIDAR signal for flight leg 6.

There was light turbulence all along flight leg 6. The Egrett is flying along the edge of the mammatus clouds between the 13km mark and the 40km mark. As the Egrett flew through the edge of the clouds the dissipation rate is relatively high compared to the dissipation rates observed during the first 7 km and the final 14 km of the flight leg.

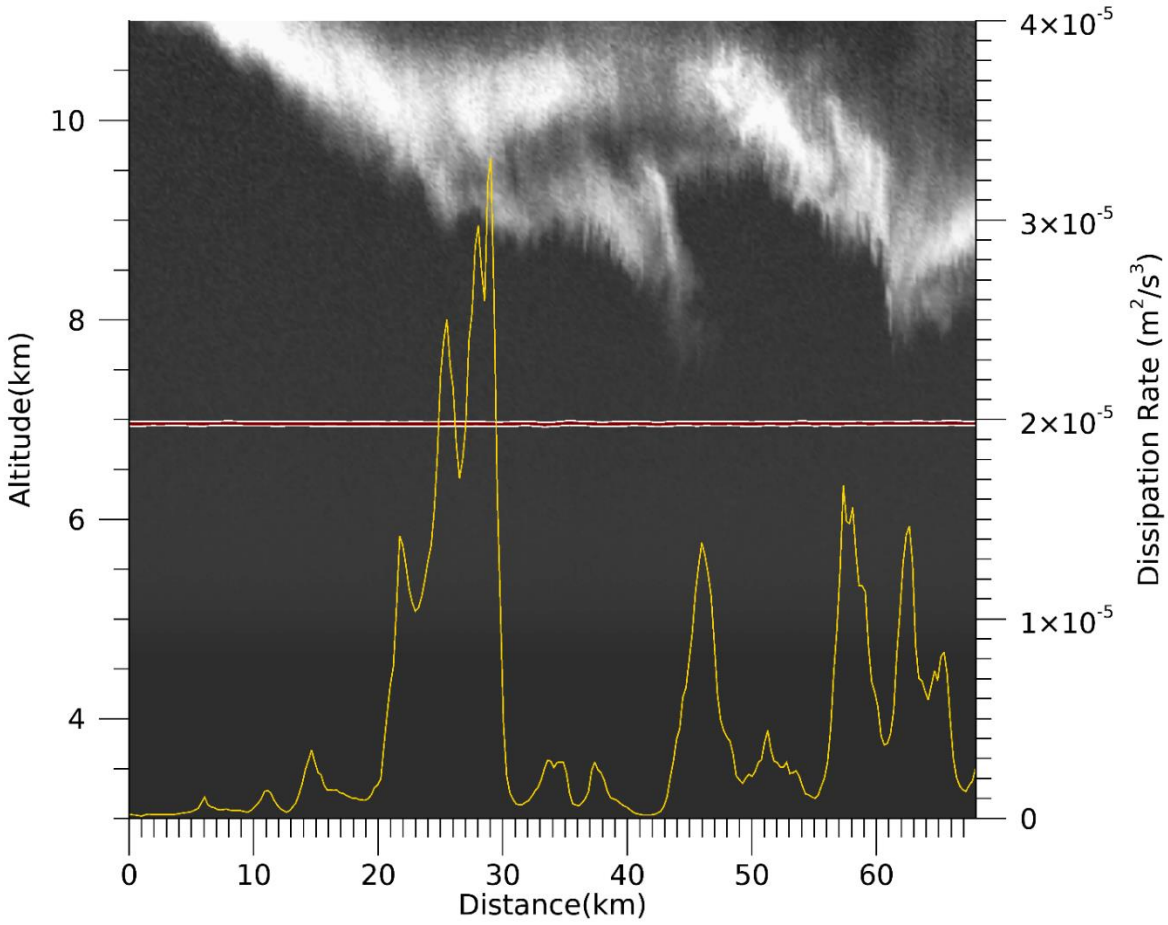

Figure 4.15: Eddy dissipation rate for *w'* (gold) plotted on top of the LIDAR signal for flight leg 8.

Light turbulent flow was observed along flight leg 8. The patches of turbulence generally correspond with the location of the local maxima in the dissipation rate. The maxima in the dissipation rate were observed at the following locations along the flight leg, 21-29.5 km, 45-47 km, 57-60 km, 62-64 km.

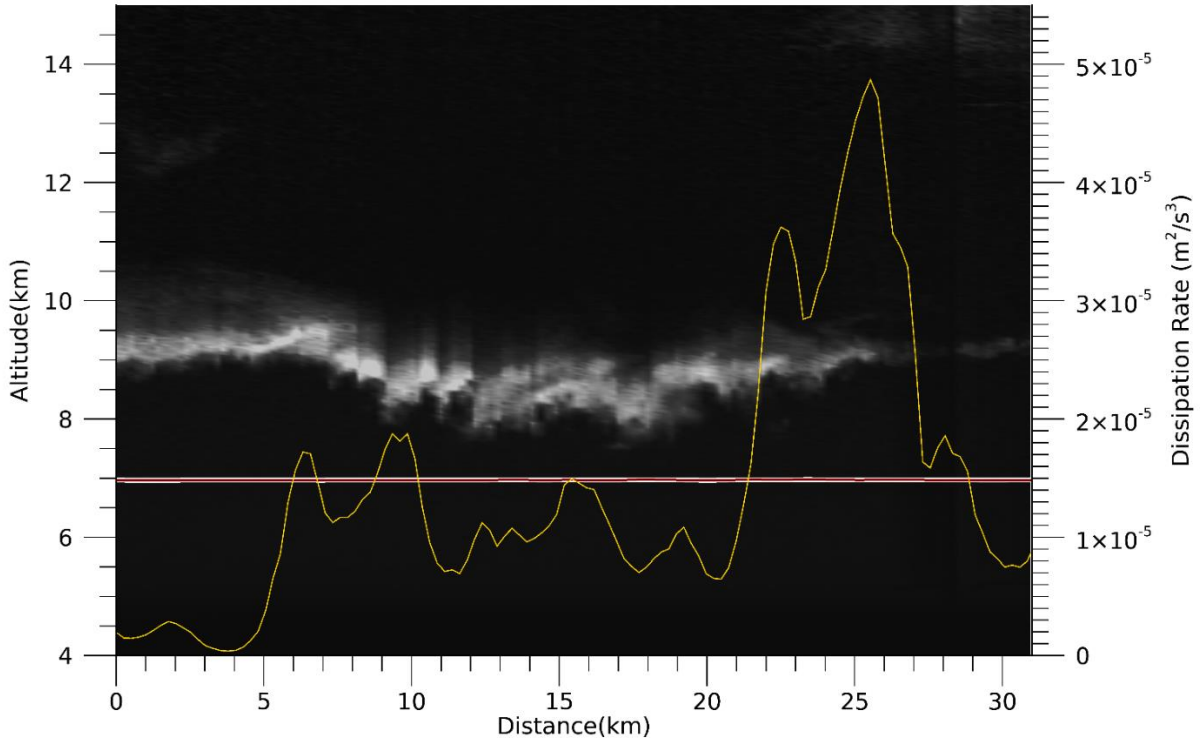

Figure 4.16: Eddy dissipation rate for *w'* (gold) plotted on top of the LIDAR signal for flight leg 9.

Light turbulent flow was observed along flight leg 9 along the entire length of the flight. The average dissipation rate increases over the course of the flight leg.

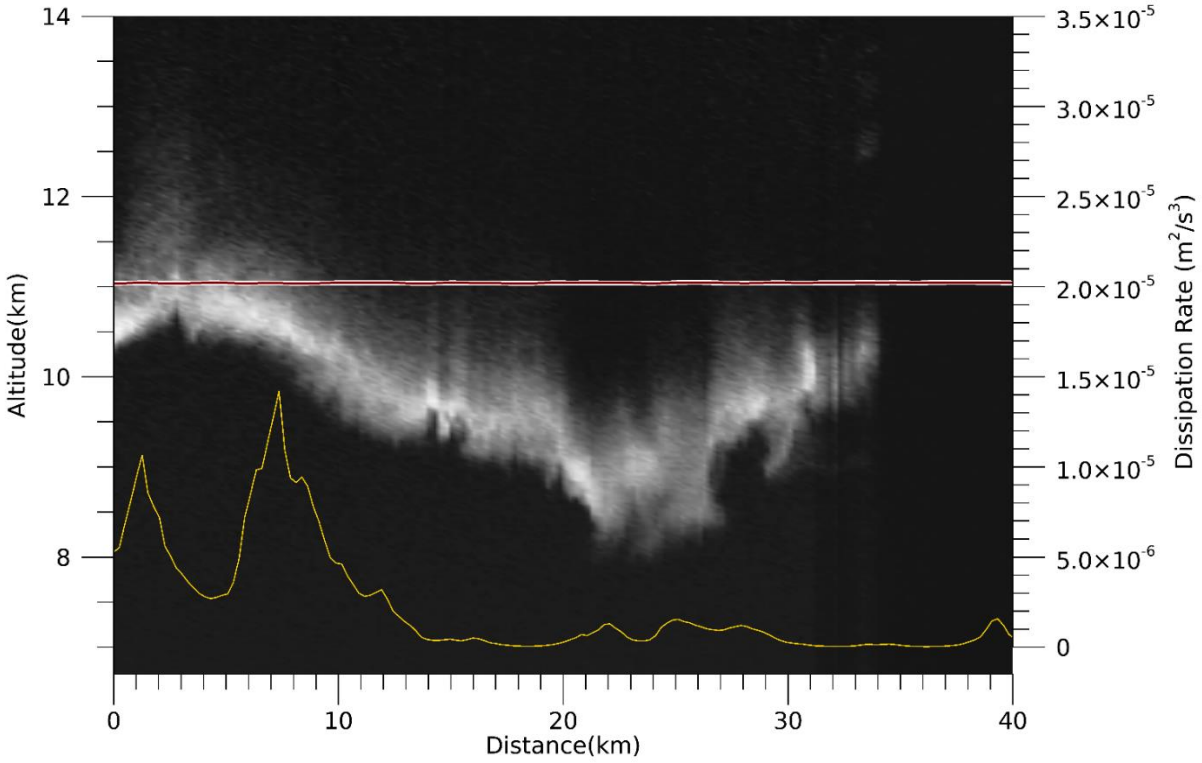

Figure 4.17: Eddy dissipation rate for *w'* (gold) plotted on top of the LIDAR signal for flight leg 11.

The Egrett encountered light turbulent flow along flight leg 11. The turbulence is stronger at the beginning of flight leg 11 than it is towards the end. This is reflected by a negative trend in the dissipation rate over the course of the flight.

4.2 - State of the Atmosphere

As stated at the beginning of the chapter, the vertical profiles for atmospheric state variables such as temperature, moisture, and wind components have been designed by taking all data points from the flight legs and sorting the data according to altitude. The Egrett did not always fly vertically through the anvil cloud and some of the data used in the vertical profile comes from horizontal flight legs. The dashed lines on the vertical profiles represent the height levels where the Egrett was flying horizontally. Along each horizontal flight leg there is a large

amount of variation in the atmospheric properties that are being measured. These are fluctuations that are caused by the vertical motion of air and the vertical advection of air parcels. Air parcels that are moved vertically will be either heated or cooled adiabatically and their potential temperature will be conserved. Large variations in the moisture profile along horizontal flight legs occur because the Egrett is flying between saturated air and cloudy air.

4.2.1 - Temperature & Potential Temperature

The temperature profile can provide information on the stability of the atmosphere, which can be inferred from the vertical gradients in temperature and humidity. It can be used to figure out where there may have been latent heat released into the environment or where it was taken away. Latent heat is released into the environment when condensation or deposition occurs and this will cause warming. On the other hand, latent heat is taken away from the environment during the process of evaporation or sublimation and this would cause cooling. Figure 4.18 displays a vertical profile of the temperature in the vicinity of the base of the mammatus clouds.

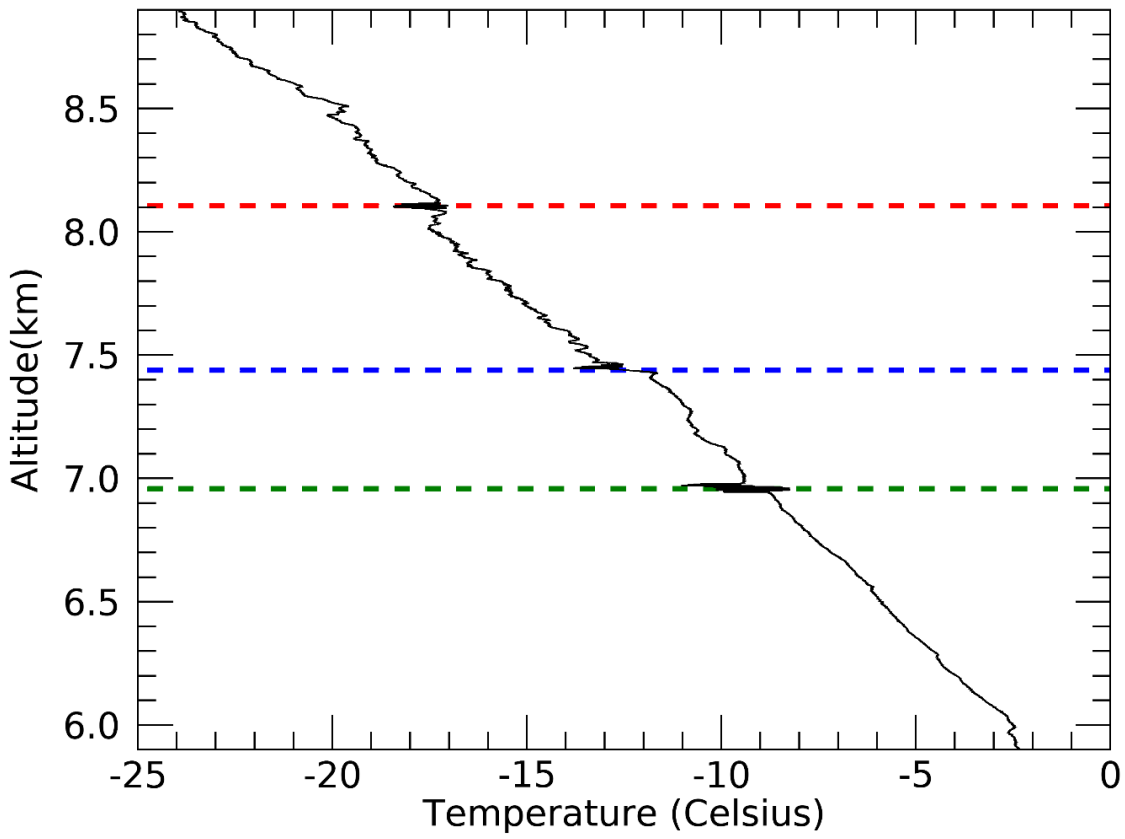

Figure 4.18: The vertical profile of air temperature in the vicinity of the mammatus cloud base. The base of the mammatus clouds is at approximately 7.45 km. The approximate altitude of flight leg 5 is represented by the red dotted line, the blue dotted line is horizontal flight leg 6 and the green dotted line represents flight legs 8 & 9.

The air temperature profile highlights two distinct layers in the vicinity of the cloud base. The temperature is between -2.5ºC and -11ºC from an altitude of 5.9 km up to 7.45 km. The temperature is between -11ºC and -18.7ºC in the layer between the altitudes of 7.45 km and 8.1 km. It is clear that there is a cold layer of air is sitting on top of a relatively warm layer of air. The potential temperature data also provides information on the stability of the atmosphere and it can be used to find areas where mixing is occurring. Figure 4.19 is a vertical profile of the potential temperature in the area of the mammatus clouds.

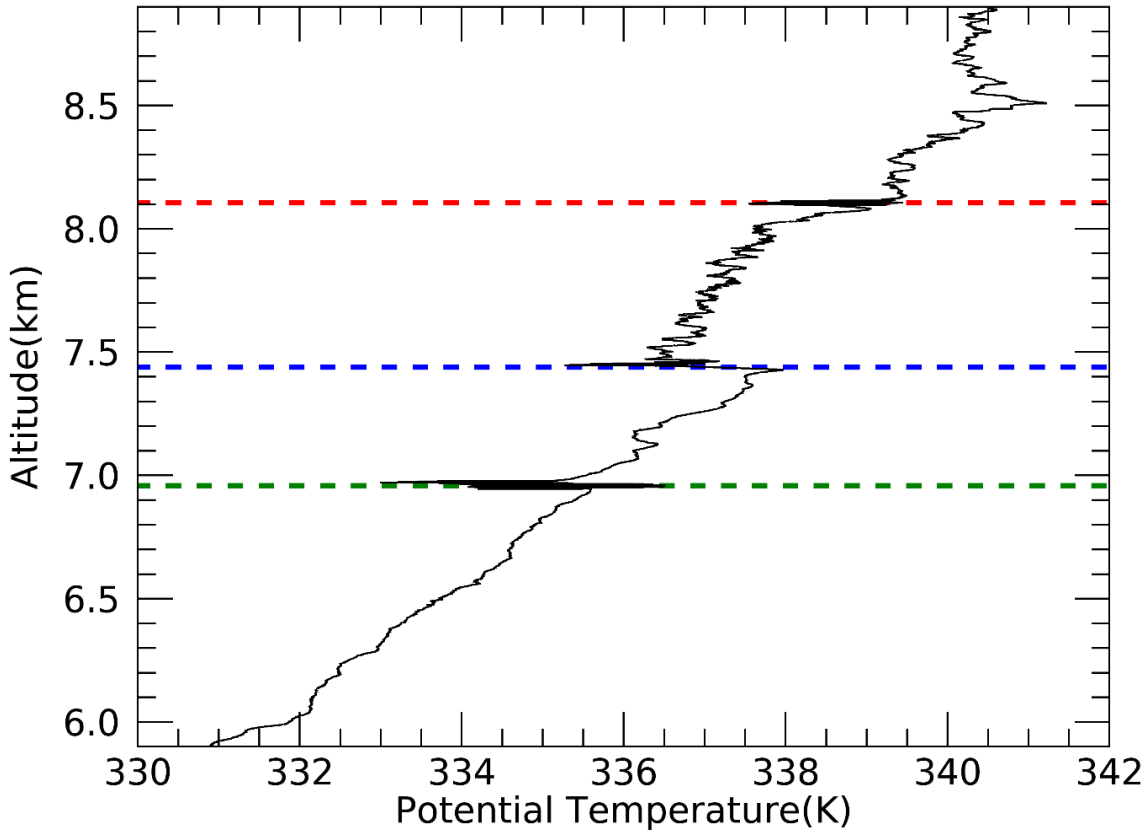

Figure 4.19: The vertical profile of potential temperature in the vicinity of the mammatus cloud base. The base of the mammatus clouds is at approximately 7.45 km. The approximate altitude of flight leg 5 is represented by the red dotted line, the blue dotted line is horizontal flight leg 6 and the green dotted line represents flight legs 8 & 9.

Between the heights of 6.9 km and 8.1 km the potential temperature profile shows that there is a layer of potentially cold air is sitting on top of a layer of potentially warm air and the interface between these two layers is around the same altitude as the cloud base. Figure 4.20 is a vertical profile of the potential temperature between the altitudes of 6.9 km and 7.7 km

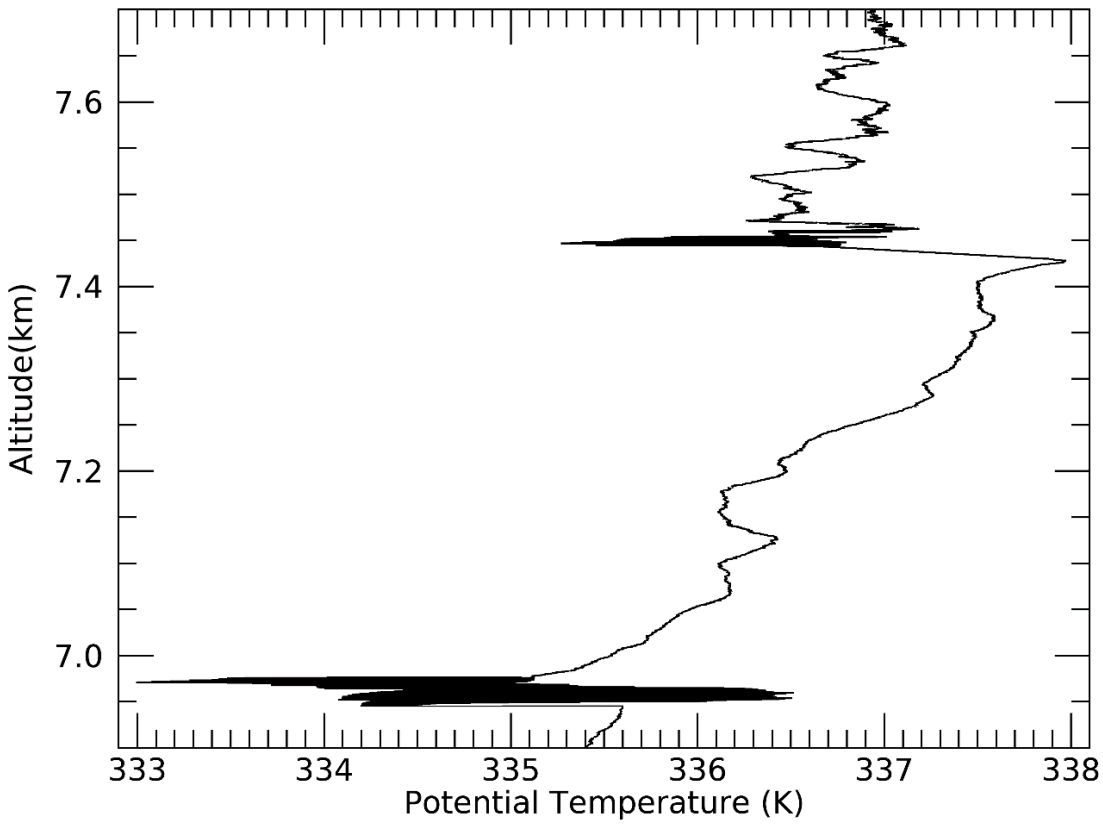

Figure 4.20: The vertical profile of potential temperature between the altitudes of 6.9 km and 7.7 km.

The potential temperature gradient is consistently negative between 7.44 km and 7.45 km. This suggests that the environment at the base of the cloud is convectively unstable. At the altitude of the cloud base the maximum potential temperature that was observed (338.8 K) is observed again at an altitude of 8.0 km and the minimum potential temperature that was observed (335.5 K) occurs below the cloud base at an altitude of 6.9 km. This is an indication that air from inside the cloud is being brought down to the cloud base and there is air underneath the cloud that is being brought up to the cloud base.

Equivalent potential temperature is the conserved temperature quantity for saturated air. It is used to obtain information on stability and mixing for saturated air in the atmosphere. Figure 4.21 is a vertical profile of the equivalent potential temperature in the vicinity of the base of the mammatus clouds.

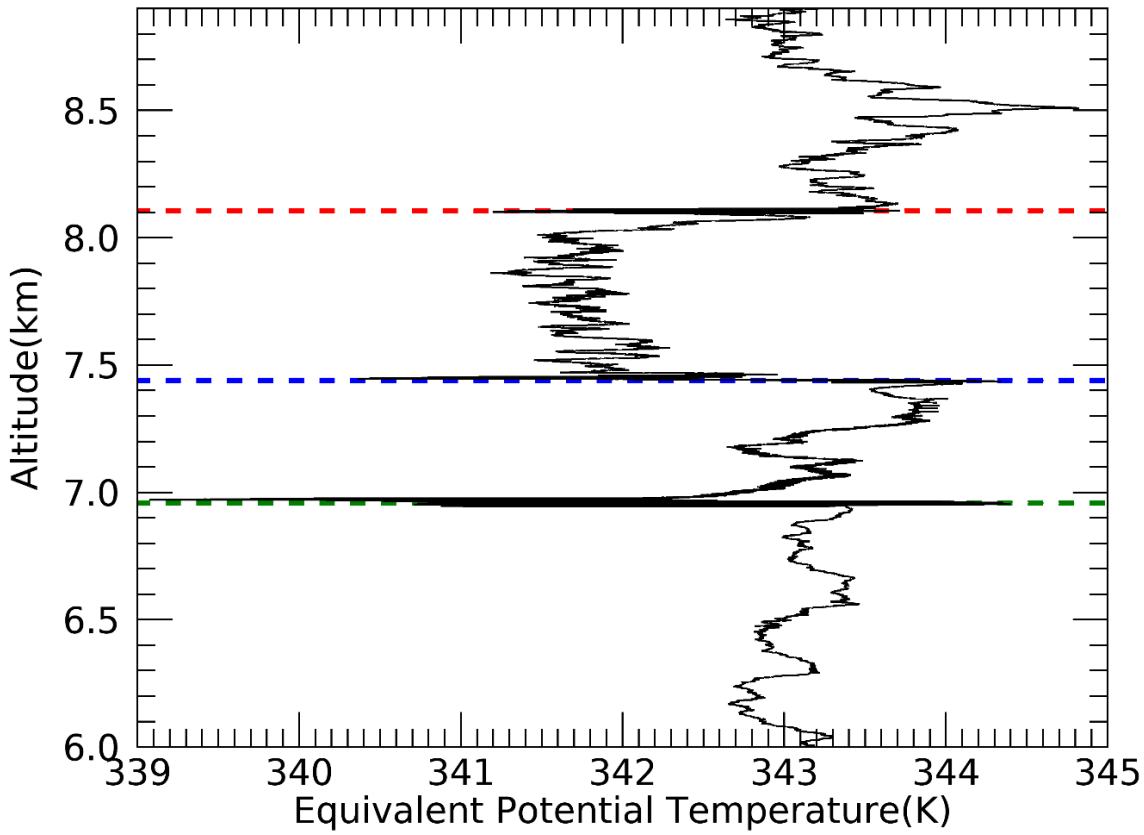

Figure 4.21: The vertical profile of the atmospheric equivalent potential temperature in the vicinity of the mammatus cloud base. The base of the mammatus clouds is at approximately 7.45 km. The approximate altitude of flight leg 5 is represented by the red dotted line, the blue dotted line is horizontal flight leg 6 and the green dotted line represents flight legs 8 & 9.

The equivalent potential temperature profile shows that equivalent potential temperature is higher in the sub cloud layer and inside of the cloud the average equivalent potential temperature drops by a few degrees. The altitude of the cloud base is around the

same altitude of the interface between these two layers. Inside of the cloud the average equivalent potential temperature decreases with height which indicates instability inside of the cloud. At the altitude of the cloud base (7.45 km) there is a very large range of equivalent potential temperature values.

This is similar to what happened with the potential temperature at the cloud base. The peak equivalent potential temperature at the cloud base (351.3 K) is very close to the equivalent potential temperature at 7.3 km (351 K). The minimum equivalent potential temperature at the altitude of the cloud base (345.6 K) matches the equivalent potential temperature at 8.1km. This is another sign that air inside of the cloud is being brought down to the cloud base and air from underneath the cloud is moving up towards the base of the cloud.

4.2.2 - Moisture

The next state variable of the atmosphere that must be analyzed is moisture. Atmospheric moisture was studied by creating vertical profiles of the relative humidity with respect to ice and the water vapour mixing ratio. Figure 4.22 displays the derived vertical profile of relative humidity in the vicinity of the mammatus clouds that developed of December 2nd, 2002. The data that is displayed in this section has been derived using the measurements from the frost point hygrometer.

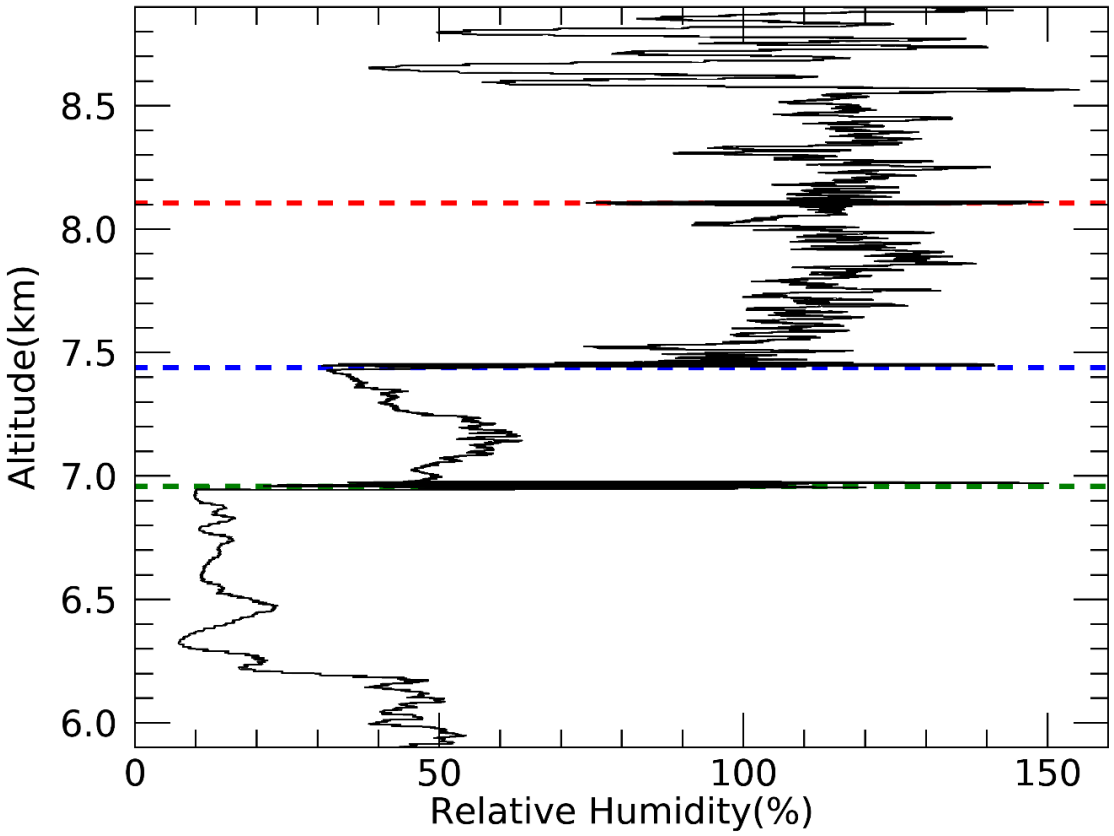

Figure 4.22: The vertical profile of relative humidity in the vicinity of the mammatus cloud base. The base of the mammatus clouds is at approximately 7.45 km. The approximate altitude of flight leg 5 is represented by the red dotted line, the blue dotted line is horizontal flight leg 6 and the green dotted line represents flight legs 8 & 9.

The relative humidity profile generally shows there is a layer of saturated air sitting on top of a layer of sub-saturated air. In the sub cloud layer the relative humidity ranges from 7.1% to 63.6%. Any ice particles that fall out of the cloud are likely to sublimate. The Egrett passed through some cloud along flight leg 8 which was conducted at an altitude of 6.96 km, there is a large range of relative humidity values along this flight leg. Figure 4.23 displays the vertical profile of the water vapour mixing ratio in the vicinity of the base of the Mammatus clouds.

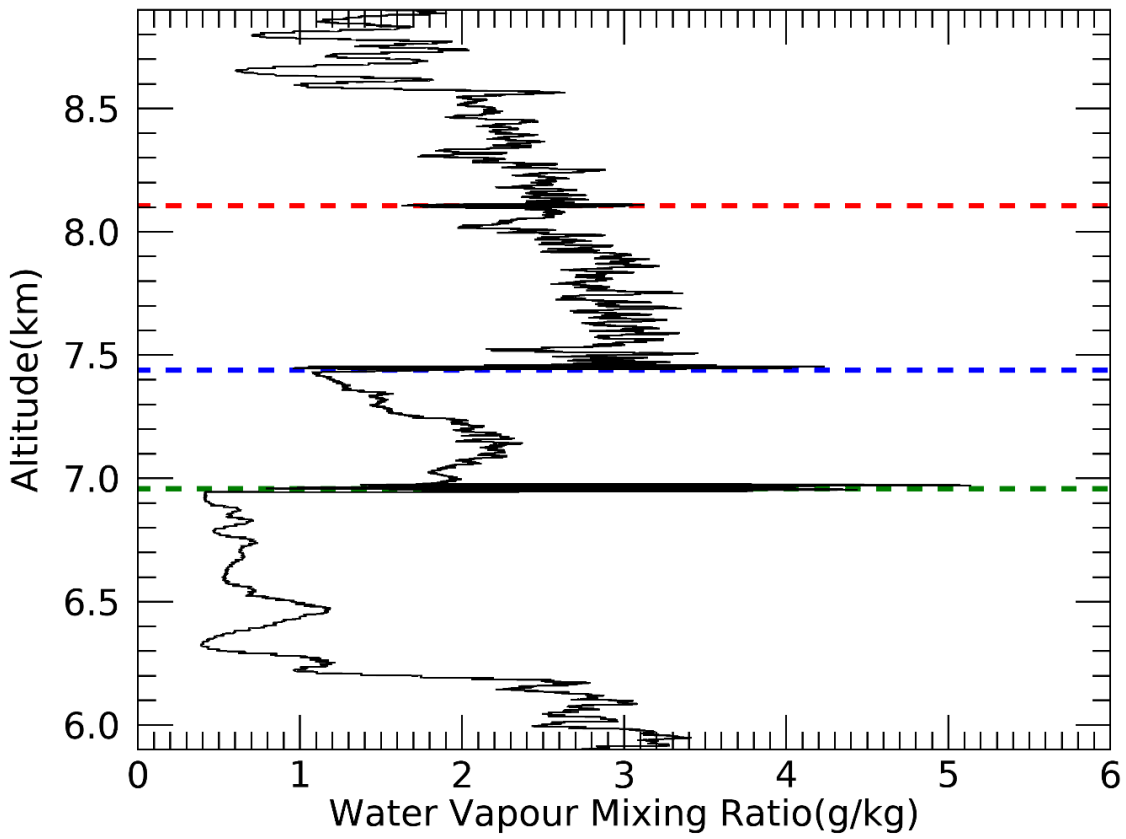

Figure 4.23: The vertical profile of water vapour mixing ratio in the vicinity of the mammatus cloud base. The base of the mammatus clouds is at approximately 7.45km. The approximate altitude of flight leg 5 is represented by the red dotted line, the blue dotted line is horizontal flight leg 6 and the green dotted line represents flight legs 8 & 9.

The water vapour mixing ratio profile shows that the water vapour in the dry sub-cloud air ranges from 0.4 g/kg to 2.4 g/kg and in the cloudy air water vapour mixing ratio is approximately 3 g/kg on average between 7.45 km and 7.9 km. Above 7.9 km the water vapour mixing ratio decreases with height. Inside of clouds the water vapour mixing ratio can be as high as 5.14 g/kg.

Temperature, potential temperature, equivalent potential temperature and moisture can be summarized by a skewT-logP chart. This type of chart is very useful for analyzing

all of these variables at one time. Figure 4.24 is a skewT-logP chart for the environment where the thunderstorm developed on December 2nd 2002.

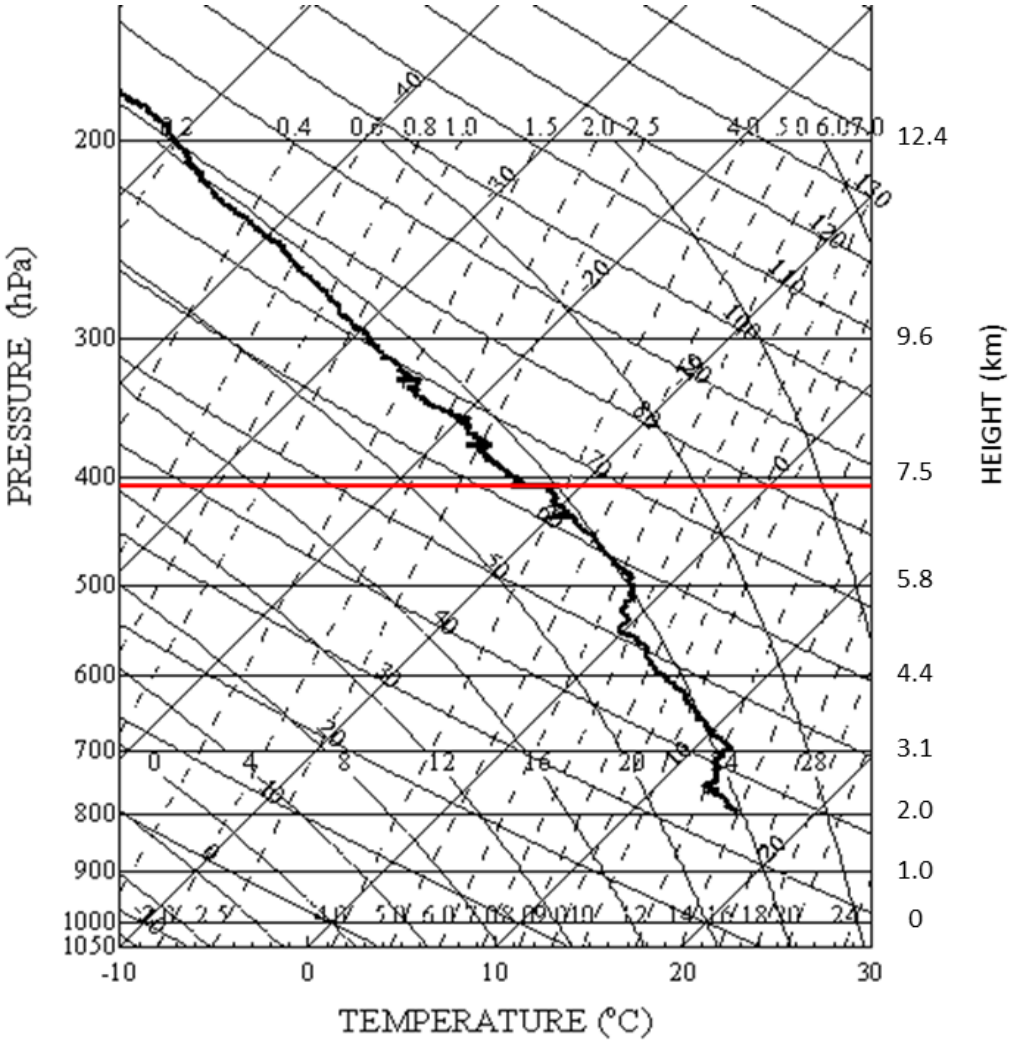

Figure 4.24: SkewT-logP chart for December 2nd, 2002. This represents the environment in the anvil outflow of Hector. The red line is the approximate altitude of the cloud base.

On the skewT-logP chart the base of the mammatus clouds is at approximately 409 hPa. Where the temperature drops suddenly from -10.8 ºC to -13.8 ºC. There is a sharp drop in the potential temperature and equivalent potential temperature as well. In the lower part of the anvil cloud the equivalent potential temperature is decreasing with height up until 350 hPa where the equivalent potential temperature becomes approximately constant with

height and then starts to increase with height above the 300 hPa pressure level. The chart confirms that the atmosphere is unstable at the base of the mammatus clouds and the atmosphere remains unstable through the mammatus clouds and into the lower section of the anvil cloud.

4.2.3 - Richardson Number Profile

The final section on the state of the atmosphere will deal with the Richardson number (*Ri*). Since the focus of the study is on cloudy air, *Ri* was calculated using equivalent potential temperature. It will be called the moist Richardson number so that there is no confusion with the standard Richardson number. It is known that there is buoyant instability occurring at the cloud base, analyzing *Ri* will help with the detection of shear instability in the area of the cloud base. Figure 4.25 is a vertical profile of the moist gradient Richardson number for the environment in the anvil outflow region of the thunderstorm that was observed off the coast of Darwin.

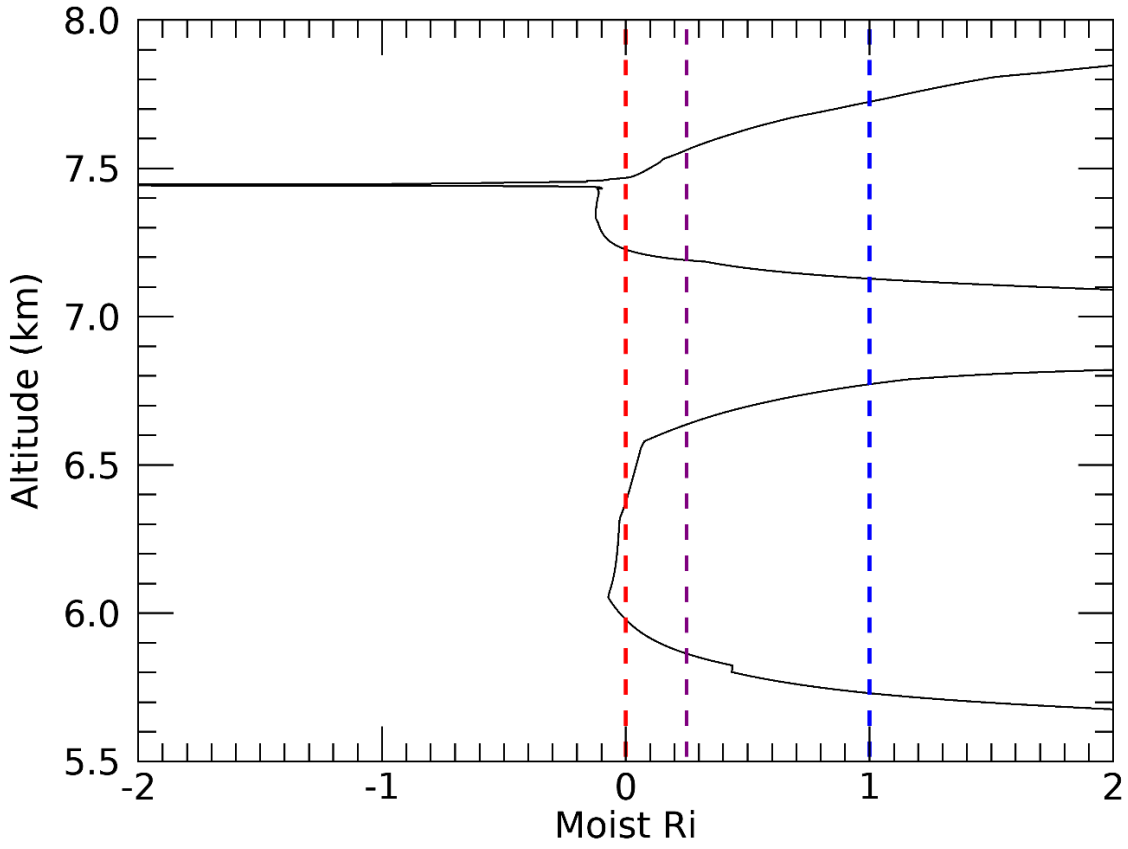

Figure 4.25: The vertical profile of the moist gradient Richardson number in the vicinity of the cloud base. *Ri* was derived using equivalent potential temperature. The red line represents *Ri* = 0, the atmosphere is conditionally unstable if *Ri* is less than 0. The purple line represents the critical Richardson number (*R*i = 0.25) laminar flow becomes turbulent if *Ri* is less than 0.25. The blue line represents *Ri* = 1.0, turbulent flow becomes laminar when *Ri* is 1.0 or greater.

The moist Richardson number profile indicates the atmosphere is conditionally unstable near the cloud base. The moist Richardson number is negative from an altitude of 5.9 km up to 6.3 km and from 7.2 km to 7.46 km. The moist Richardson number is approximately -30.96 at 7.45 km which is around the altitude of the cloud base. The results show that the atmosphere is conditionally unstable and there is a higher amount of shear in this part of the atmosphere. It would make sense for there to be a lot of shear close to the base of the anvil cloud where the outflow from the thunderstorm is moving across the

atmosphere and creates significant vertical wind shear. In addition to this *Ri* is less than 0.25 from 5.83 km up to 6.63 km and from 7.2 km up to 7.6 km, this is a sign that turbulence is being generated close to the base of the anvil cloud. Turbulence can be maintained from 5.7 km to 6.8 km and from 7.12 km to 7.72 km where *Ri* is 1.0 or less. This can be verified by looking at the vertical profile of the zonal and meridional wind in the environment of the anvil outflow. Figure 4.26 is the vertical profile of the zonal wind in the outflow region, Figure 4.27 is the vertical profile of the meridional wind in the.

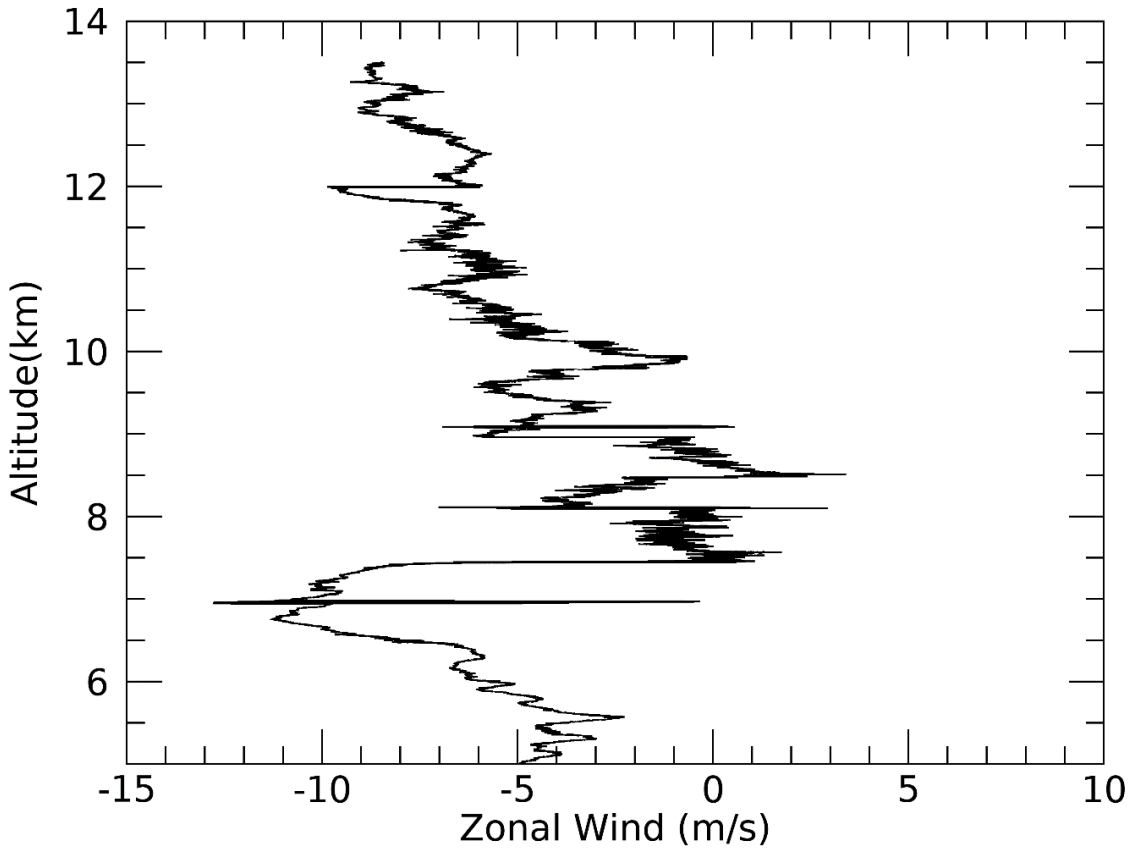

Figure 4.26: Vertical profile of the zonal wind in the anvil outflow of Hector on December 2nd, 2002.

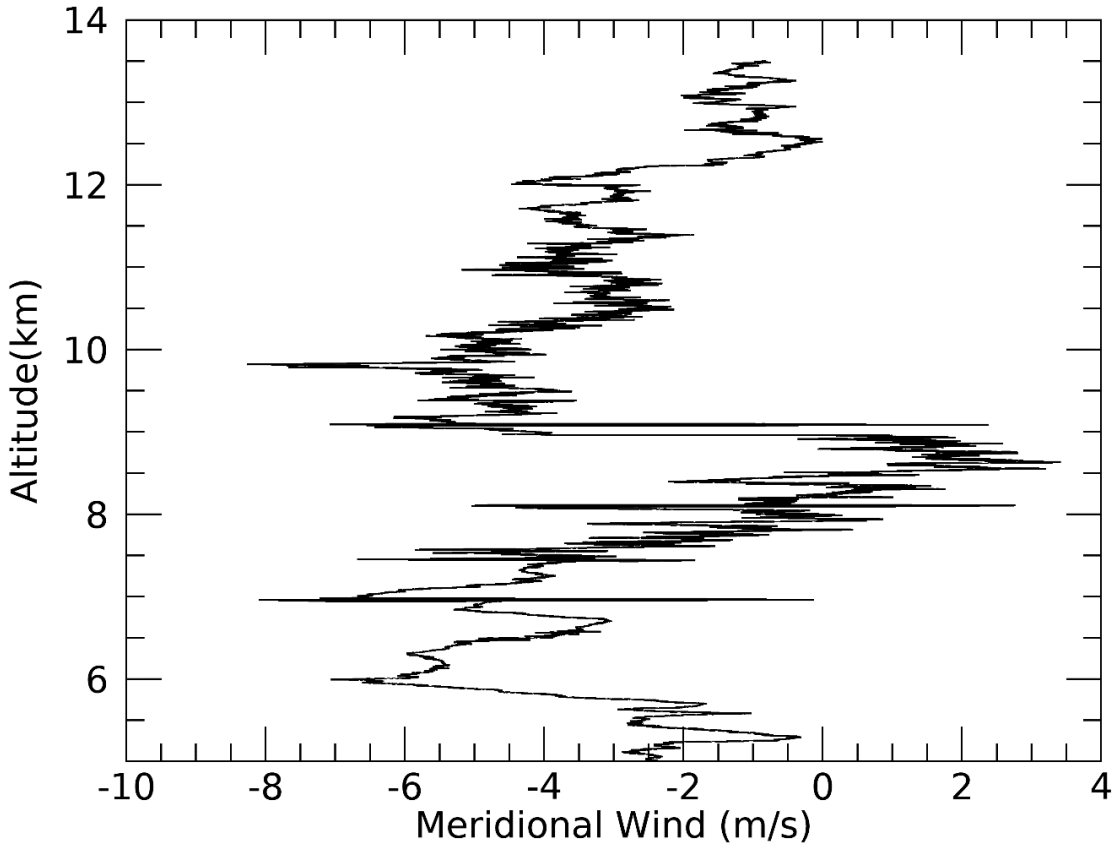

Figure 4.27: Vertical profile of the meridional wind in the anvil outflow of Hector on December 2nd, 2002.

The vertical wind profile of the zonal wind shows that there is strong wind shear in the zonal direction at an altitude of 7.4 km where the zonal wind speed goes from -9 m/s to approximately 0 m/s. This sudden change in the wind speed with height will create wind shear. The meridional wind profile shows there is a little bit of wind shear at 7.4 km but it is not very significant compared to the wind shear in the zonal direction. As discussed previously the denominator of the Richardson number represents the production of turbulence kinetic energy due to shear. This can confirm where there is a high amount of shear in the atmosphere. Figure 4.28 is the vertical profile of the value of the denominator in the Richardson number equation.

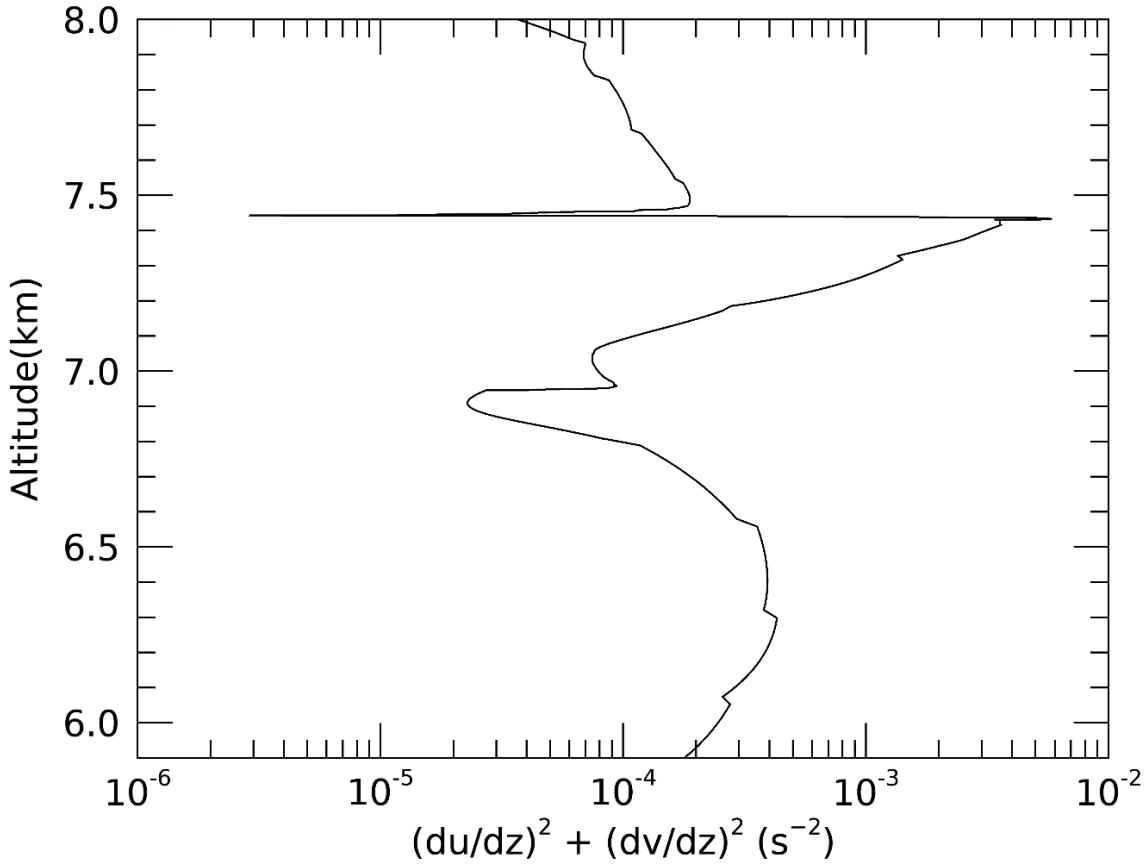

Figure 4.28: The vertical profile of the shear term (denominator of the Richardson number equation) based on wind data from December 2nd, 2002.

The vertical wind shear in this region has a maxima in the vicinity of the cloud base. The maxima occurs at an altitude of around 7.4 km where the denominator of the *Ri* equation is 6.3 x 10^{-3} s^{-2}. The Richardson number profile based on standard potential temperature has been included for a reference. Figure 4.29 is the vertical profile for the Richardson number calculated with θ.

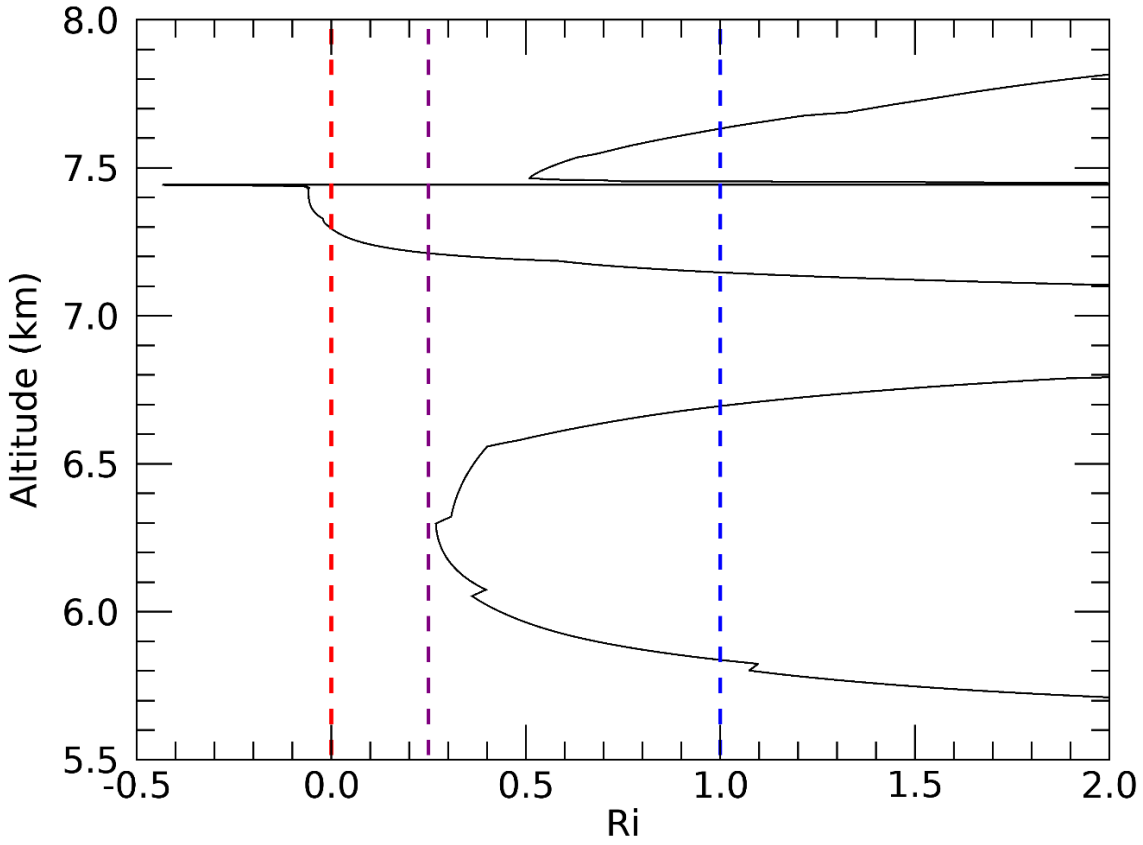

Figure 4.29: The vertical profile of the gradient Richardson number in the vicinity of the cloud base. *Ri* was derived using standard potential temperature. The red line represents *Ri* = 0, the atmosphere is unstable if *Ri* is less than 0. The purple line represents the critical Richardson number (*Ri* = 0.25) laminar flow becomes turbulent if *Ri* is less than 0.25. The blue line represents *Ri* = 1.0, turbulent flow becomes laminar when *Ri* is 1.0 or greater.

The Richardson number is less than 0.25 from an altitude of 7.2 km up to 7.44 km. These are areas where the environment is suitable for the development of turbulence. Turbulence is able to be maintained where the Richardson number is 1.0 or less. This occurs from 5.8 km up to 6.8 km, 7.15 km up to 7.44 km, and from 7.45 km up to 7.63 km.

4.3 - Waves in the Outflow

This next section of the results will involve variables that are related to the waves in the atmosphere. It is possible that waves and other coherent structures have a role in the development of mammatus clouds. Some of the mammatus cloud formation theories are based on the presence of waves such as gravity waves or Kelvin-Helmholtz waves (Petre & Verline, 2004; Gossard & Sweezy, 1974).

4.3.1 - Gravity Waves

Coherent structure kinetic energy is the kinetic energy that comes from turbulent structures with scales between 250 m and 10 km. The coherent structures that are of most interest are waves. The vertical coherent structure energy can be used to estimate where gravity waves are propagating vertically and where they may be trapped. Horizontal coherent structure energy has not been analyzed in this section. This is because horizontal wind fluctuations are not always caused by coherent structures. They may be caused by the vertical advection of the background wind shear (Whiteway et al, 2003). Therefore, horizontal wind fluctuations are not reliable for the detection of gravity waves. Figure 4.30 is a vertical profile of the coherent structure kinetic energy based on the PSD of the vertical wind fluctuations

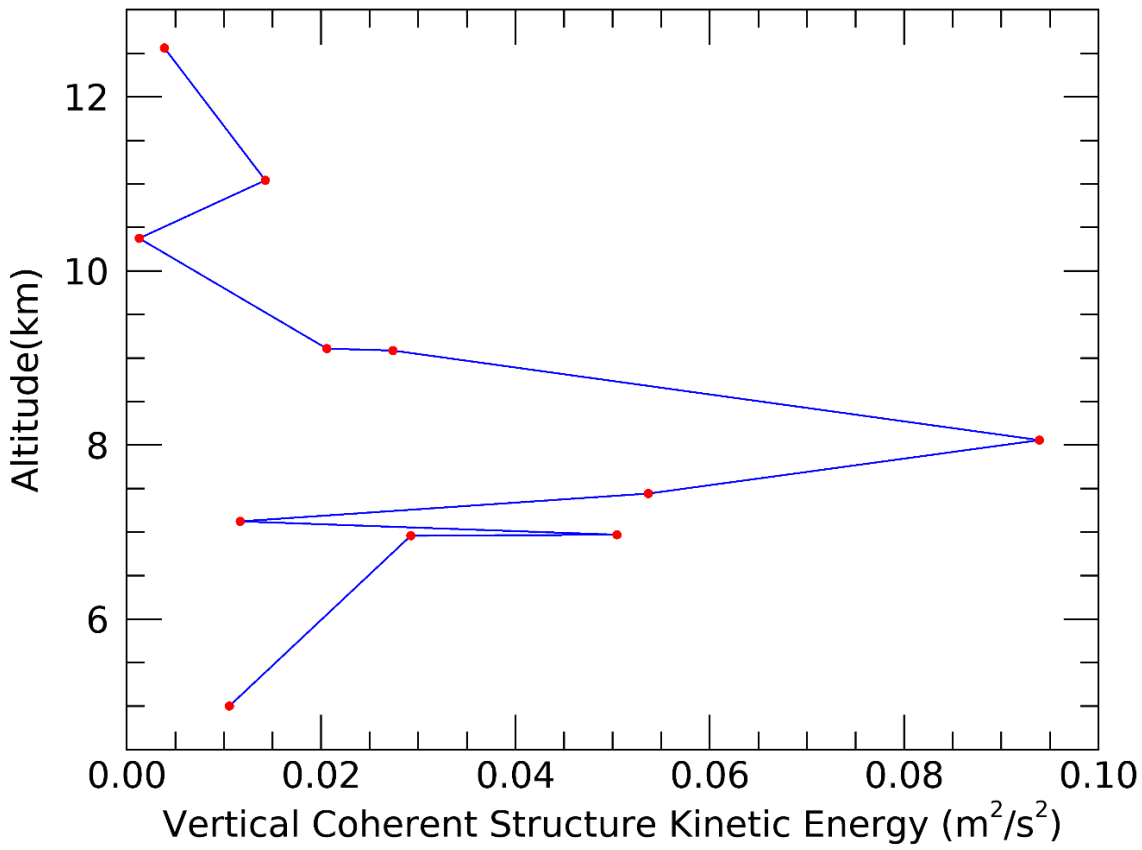

Figure 4.30: Coherent structure kinetic energy based on the PSD of vertical wind fluctuations (w') for all 11 flight legs on December 2nd, 2002.

There is a distinct peak in coherent structure kinetic energy between 7.4 km and 8.1 km while at the other altitudes the coherent structure kinetic energy is much smaller. This shows that vertically propagating gravity waves are generated and confined to the heights between 7 km and 9.1 km. Figures 4.31 to 4.41 are the PSD functions that were used to make the coherent structure energy profile. The PSD functions have been plotted in order of descending mean altitude so it coincides with figure 4.30. The area under the curve has been coloured in red across all of the coherent structure scales, this represents the coherent structure energy. The coherent structure energy is considered to be the energy for wavelength scales between 250 m and 10 km. Wavelength scales that are less than 250 m

are the scales of turbulent eddies. The polynomials that were used to estimate the atmospheric background were about 10 km long. This causes wavelength scales greater than 10 km to be attenuated.

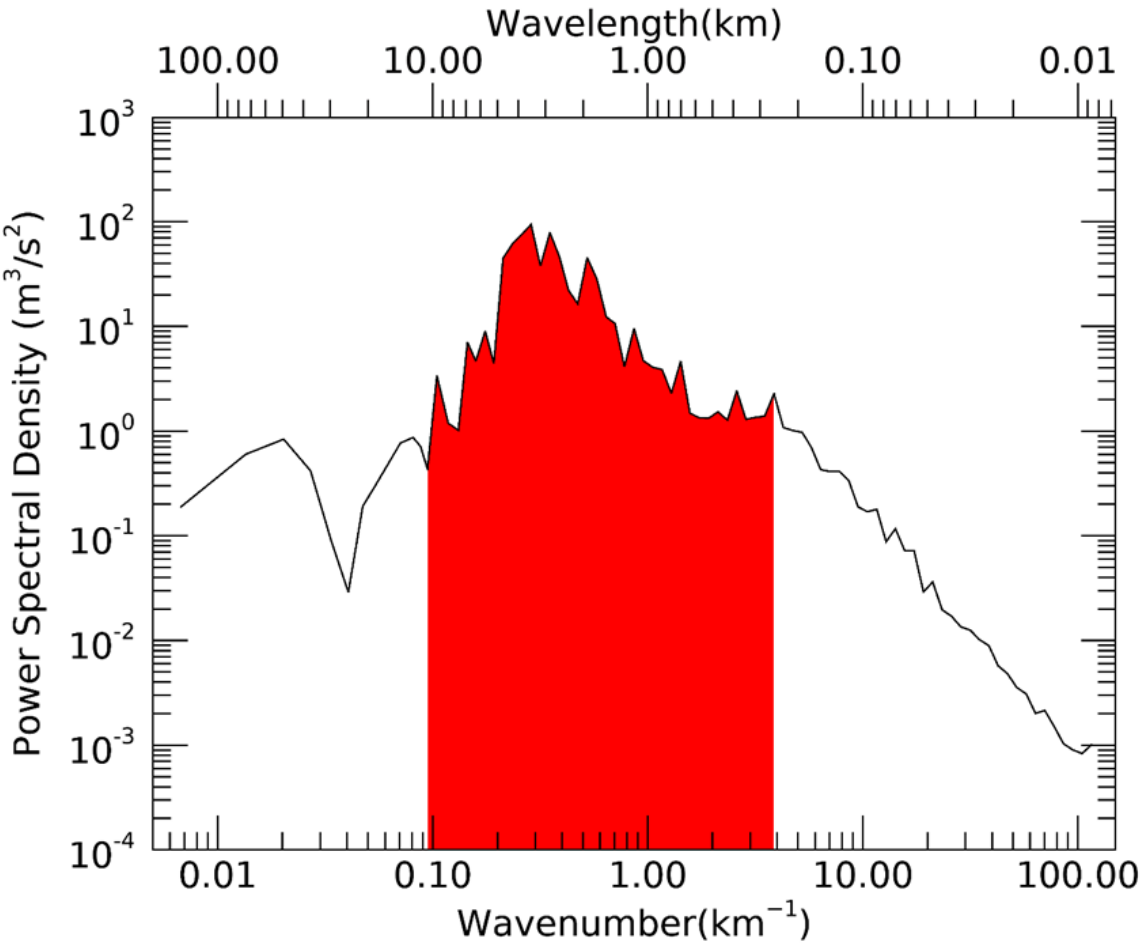

Figure 4.31: The PSD of vertical wind fluctuations, flight leg 3. The area representing the integral of the PSD across all coherent structure scales has been coloured red.

The integral of the coherent structure kinetic energy depends on the magnitude of the PSD and the range of scales that are being resolved in the integration. The coherent structure kinetic energy for flight leg 3 was 6.17 x 10^{-3} m^2/s^2 between the wavelength scales of approximately 250 m and 10km.

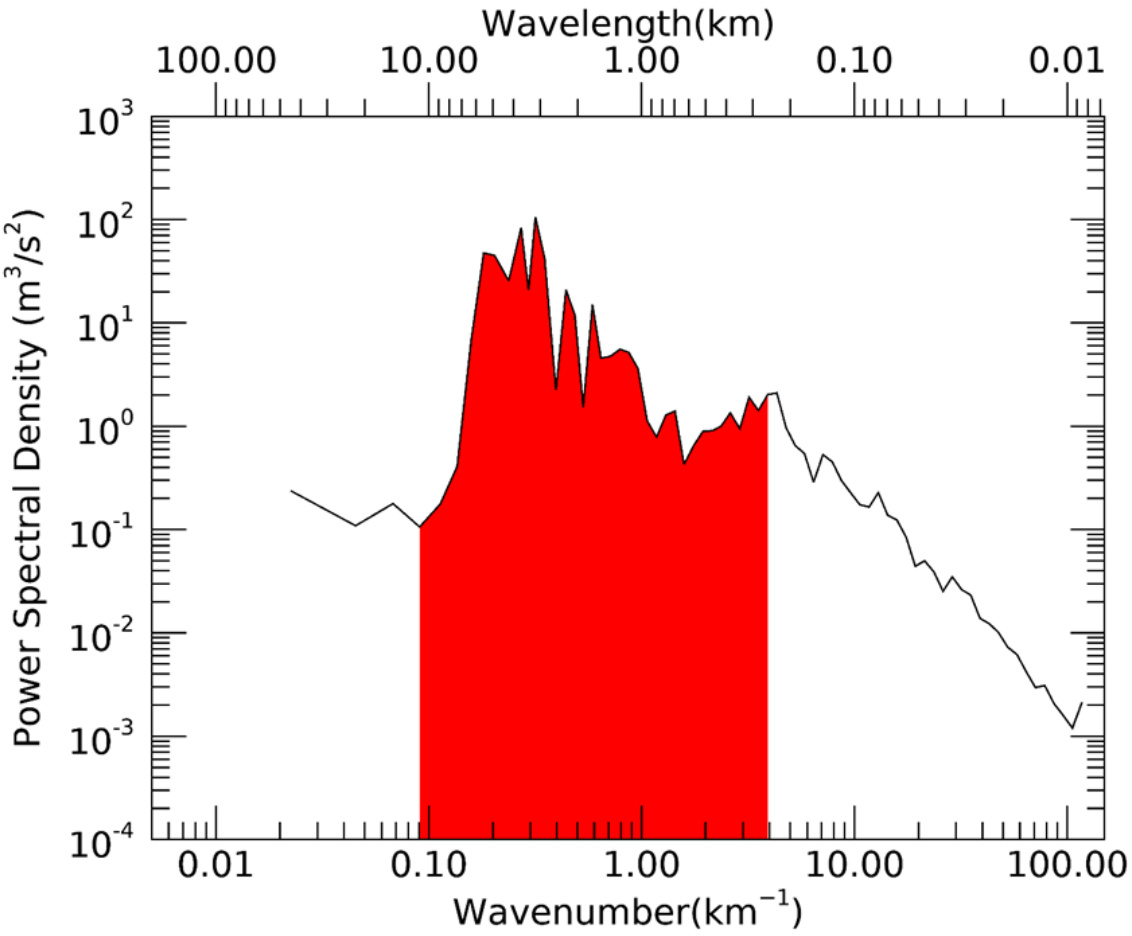

Figure 4.32: The PSD of vertical wind fluctuations, flight leg 11. The area representing the integral of the PSD across all coherent structure scales has been coloured red.

The coherent structure kinetic energy for flight leg 11 was 0.015 m^2/s^2 between the wavelength scales of approximately 250 m and 10 km. Coherent structure energy increased between the altitudes of flight leg 3 (12.56 km) and flight leg 11 (11.04 km).

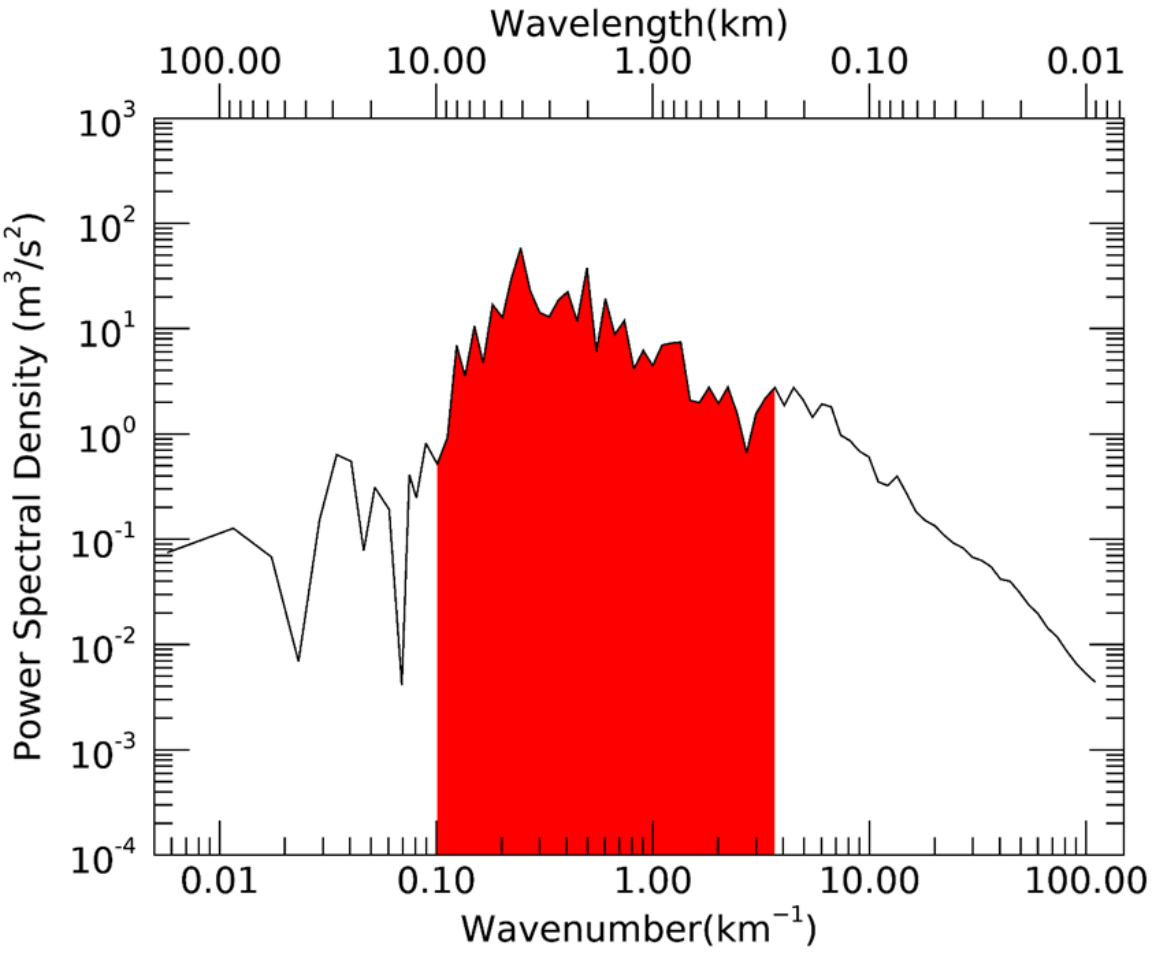

Figure 4.33: The PSD of vertical wind fluctuations, flight leg 2. The area representing the integral of the PSD across all coherent structure scales has been coloured red.

The coherent structure kinetic energy for flight leg 2 was 1.28 x 10^{-3} m^2/s^2 between the wavelength scales of approximately 250 m and 10 km. There is a decrease in energy between the altitudes of flight leg 11 (11.04 km) and flight leg 2 (10.37 km). Flight leg 2 had the lowest coherent structure kinetic energy out of all the flight legs.

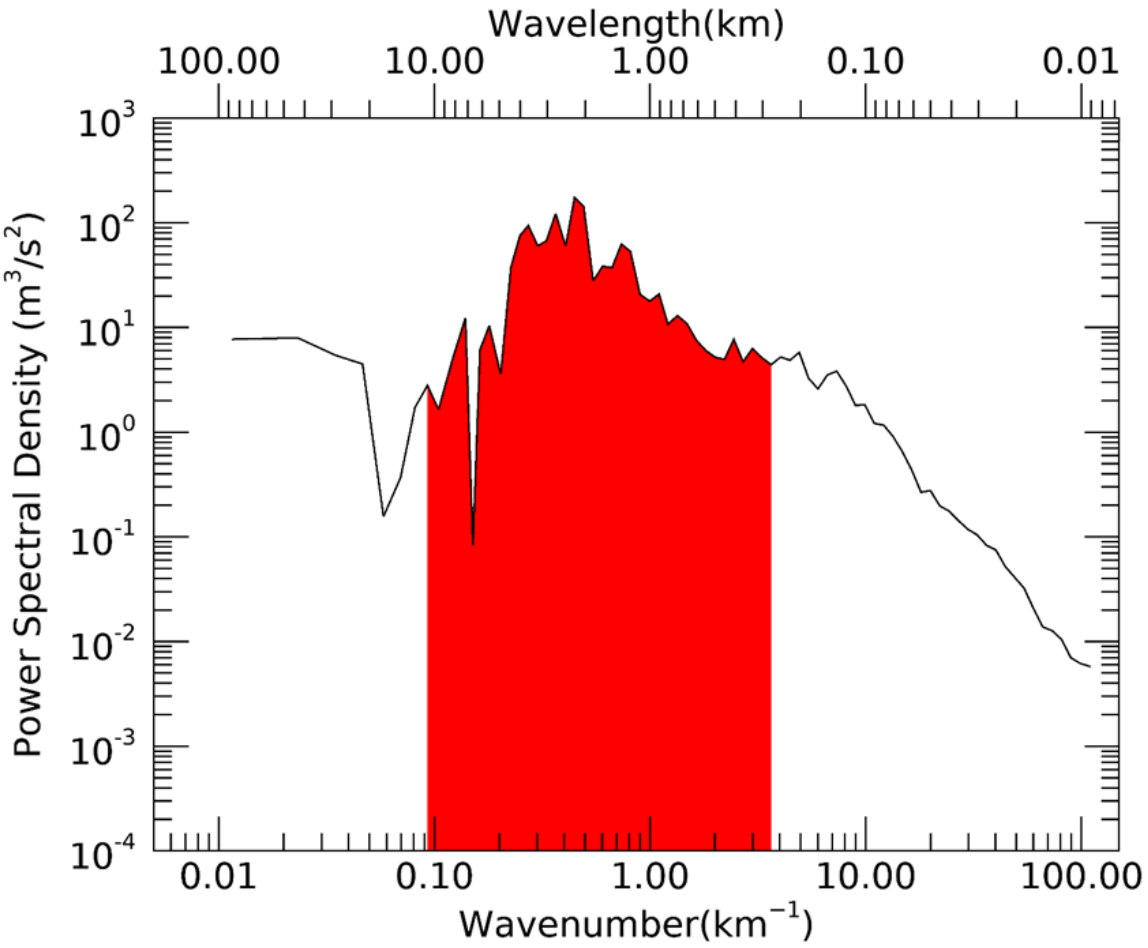

Figure 4.34: The PSD of vertical wind fluctuations, flight leg 10. The area representing the integral of the PSD across all coherent structure scales has been coloured red.

The coherent structure kinetic energy for flight leg 10 was 0.028 m^2/s^2 between the wavelength scales of approximately 250 m and 10 km. Coherent structure energy increases significantly when descending from the altitude of flight leg 2 (10.37 km) to the altitude of flight leg 10 (9.11 km).

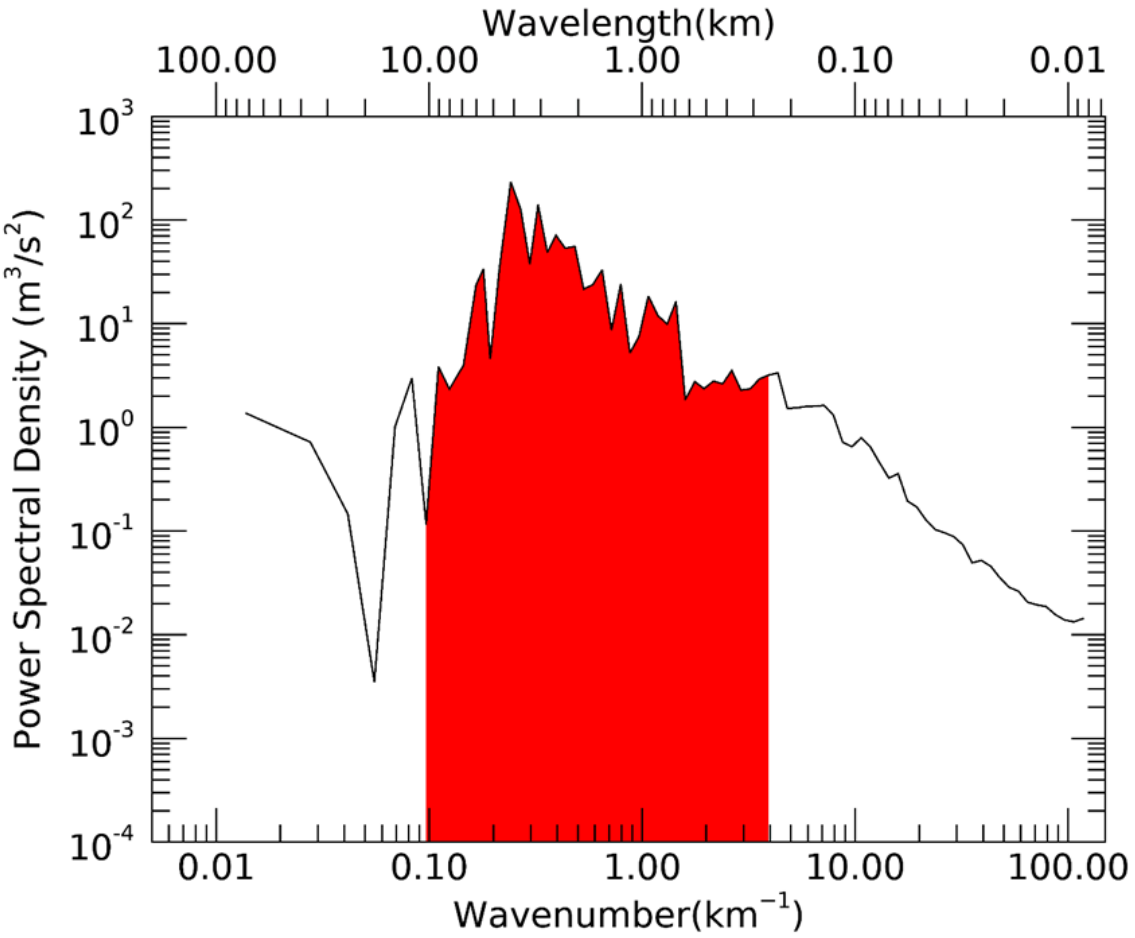

Figure 4.35: The PSD of vertical wind fluctuations, flight leg 4. The area representing the integral of the PSD across all coherent structure scales has been coloured red.

The coherent structure kinetic energy for flight leg 4 was 0.0286 m^2/s^2 between the wavelength scales of approximately 250 m and 10 km. Coherent structure kinetic energy continues to increase when descending from the altitude of flight leg 10 (9.11 km) and the altitude of flight leg 4 (9.09 km).

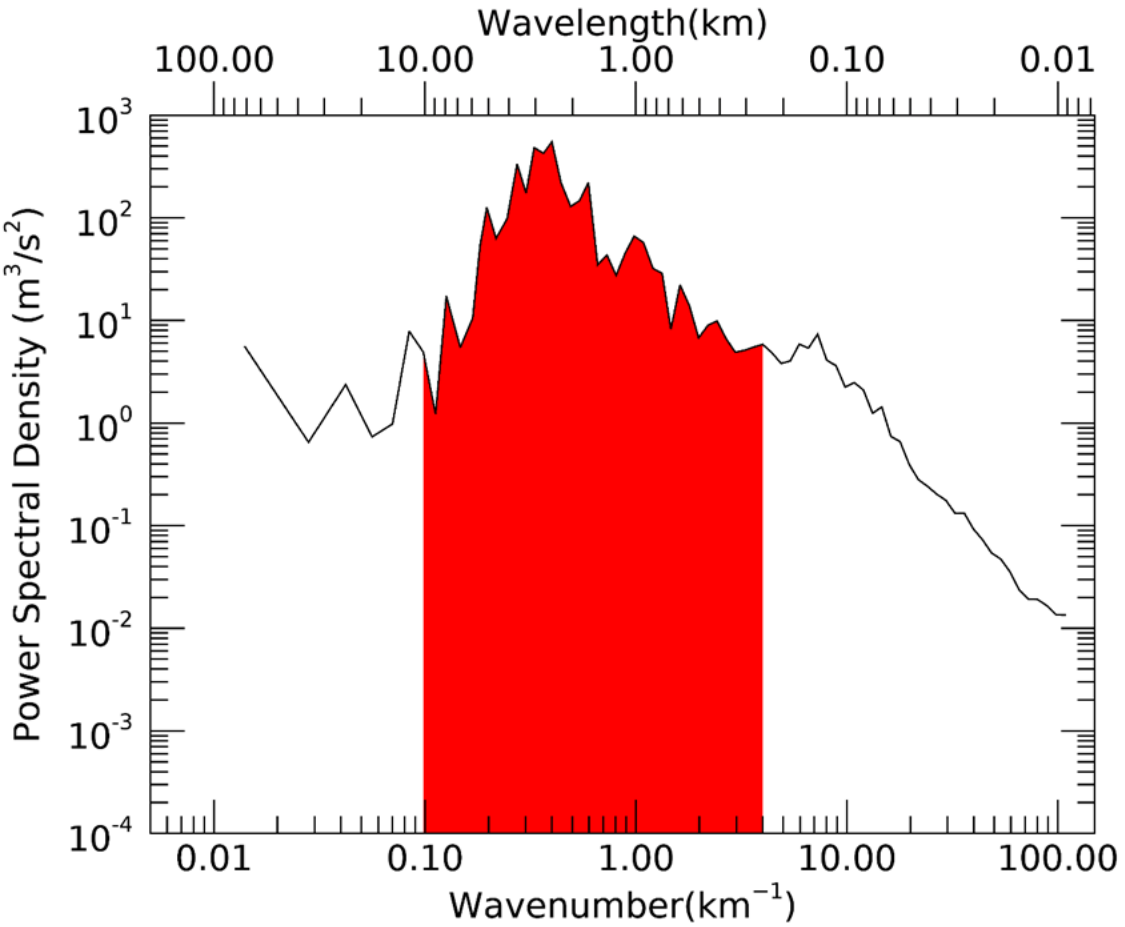

Figure 4.36: The PSD of vertical wind fluctuations, flight leg 5. The area representing the integral of the PSD across all coherent structure scales has been coloured red.

The coherent structure kinetic energy for flight leg 5 was 0.104 m^2/s^2 between the wavelength scales of approximately 250 m and 10 km. The coherent structure kinetic energy increases significantly when descending from the altitude of flight leg 4 (9.09 km) to the altitude of flight leg 5 (8.06 km). Flight leg 5 is the peak for coherent structure kinetic energy.

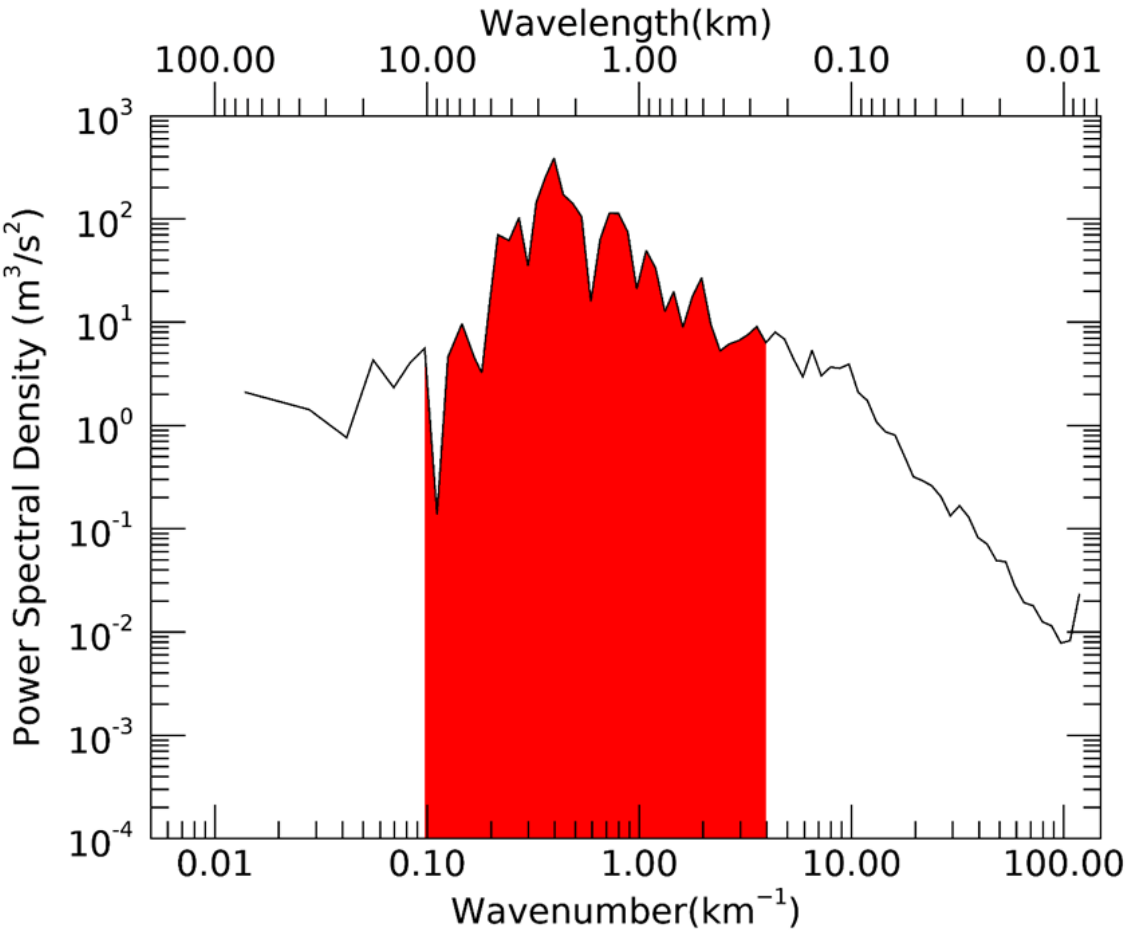

Figure 4.37: The PSD of vertical wind fluctuations, flight leg 6. The area representing the integral of the PSD across all coherent structure scales has been coloured red.

The coherent structure kinetic energy for flight leg 6 was 0.057 m^2/s^2 between the wavelength scales of approximately 250 m and 10 km. Coherent structure energy decreases on descent from the altitude of flight leg 5 (8.06 km) to the altitude of flight leg 6 (7.44 km).

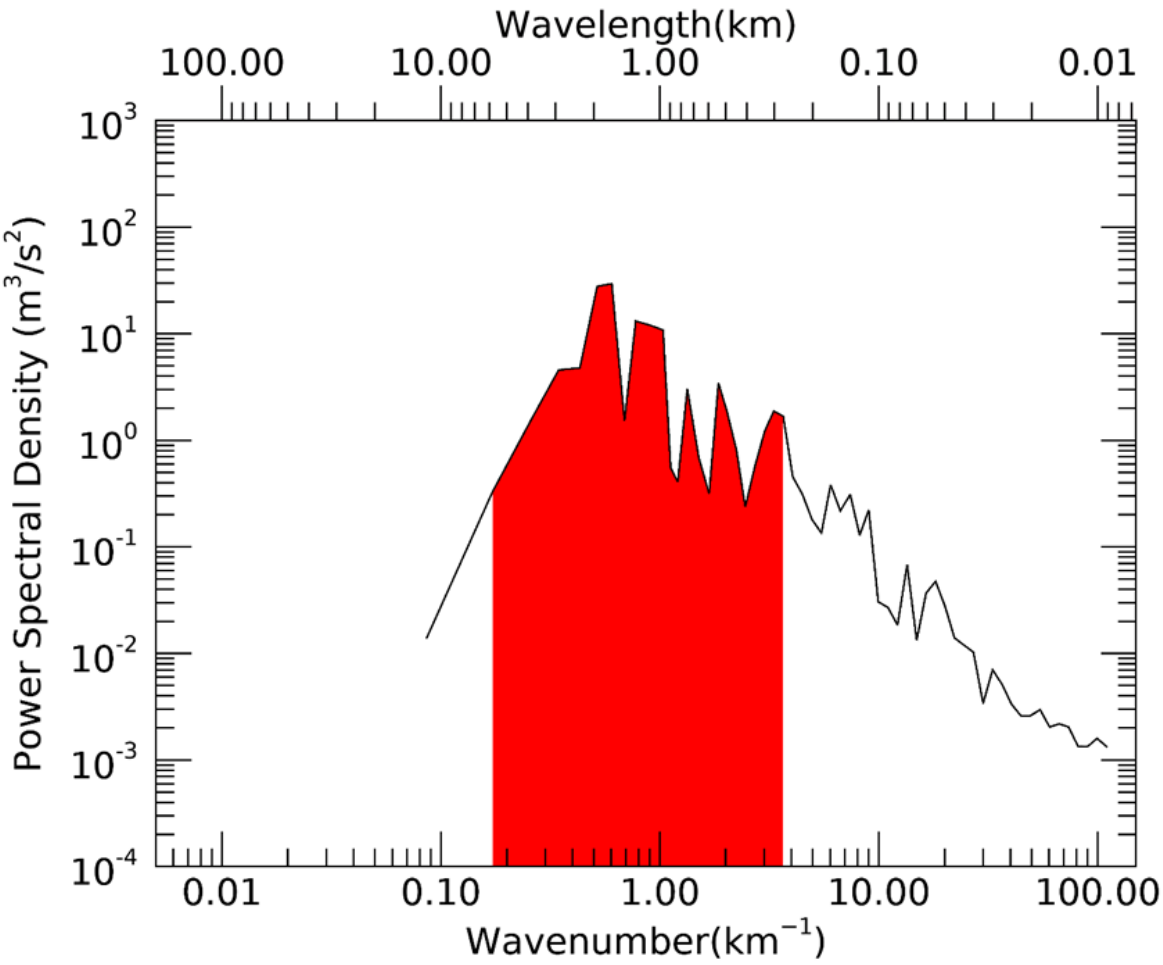

Figure 4.38: The PSD of vertical wind fluctuations, flight leg 7. The area representing the integral of the PSD across all coherent structure scales has been coloured red.

The coherent structure kinetic energy for flight leg 7 was 0.012 m^2/s^2 between the wavelength scales of approximately 250 m and 10 km. The coherent structure energy decreases when descending from the altitude of flight leg 6 (7.44 km) to flight leg 7 (7.12 km).

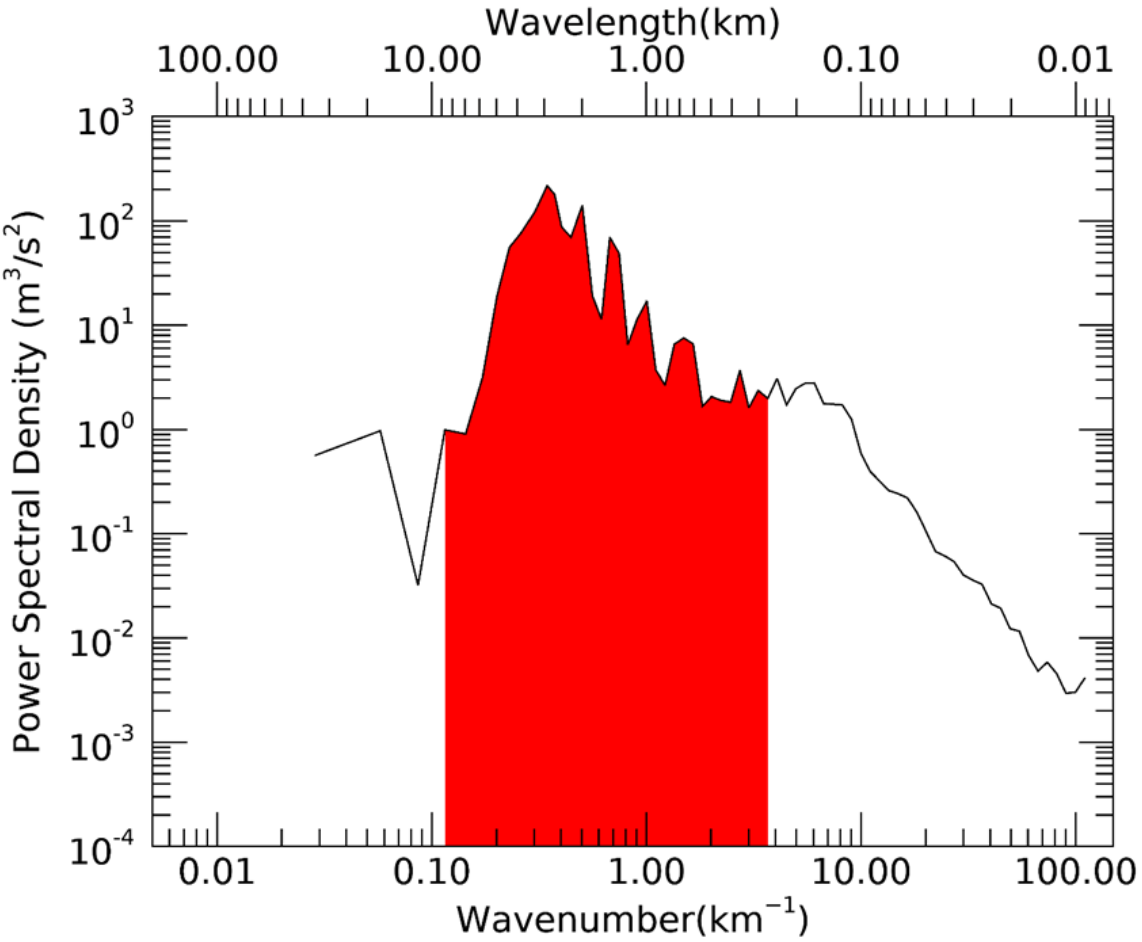

Figure 4.39: The PSD of vertical wind fluctuations, flight leg 9. The area representing the integral of the PSD across all coherent structure scales has been coloured red.

The coherent structure kinetic energy for flight leg 9 was 0.05 m^2/s^2 between the wavelength scales of approximately 250 m and 10 km. The coherent structure energy increases when descending from the altitude of flight leg 7 (7.12 km) to the altitude of flight leg 9 (6.97 km).

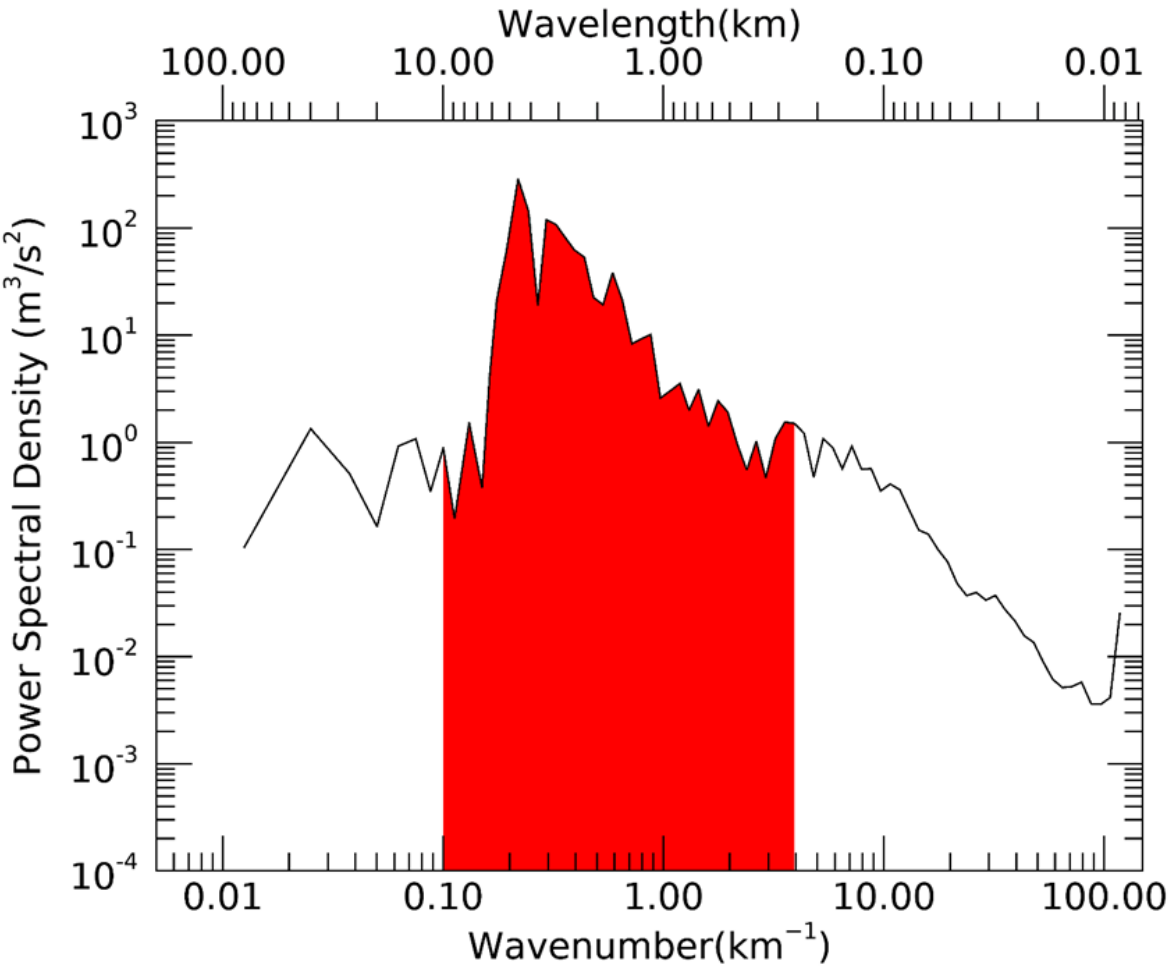

Figure 4.40: The PSD of vertical wind fluctuations, flight leg 8. The area representing the integral of the PSD across all coherent structure scales has been coloured red.

The coherent structure kinetic energy for flight leg 8 was 0.029 m^2/s^2 between the wavelength scales of approximately 250 m and 10 km. The kinetic energy at along flight leg 8 (6.96 km) is lower than the kinetic energy along flight leg 9 (6.97 km).

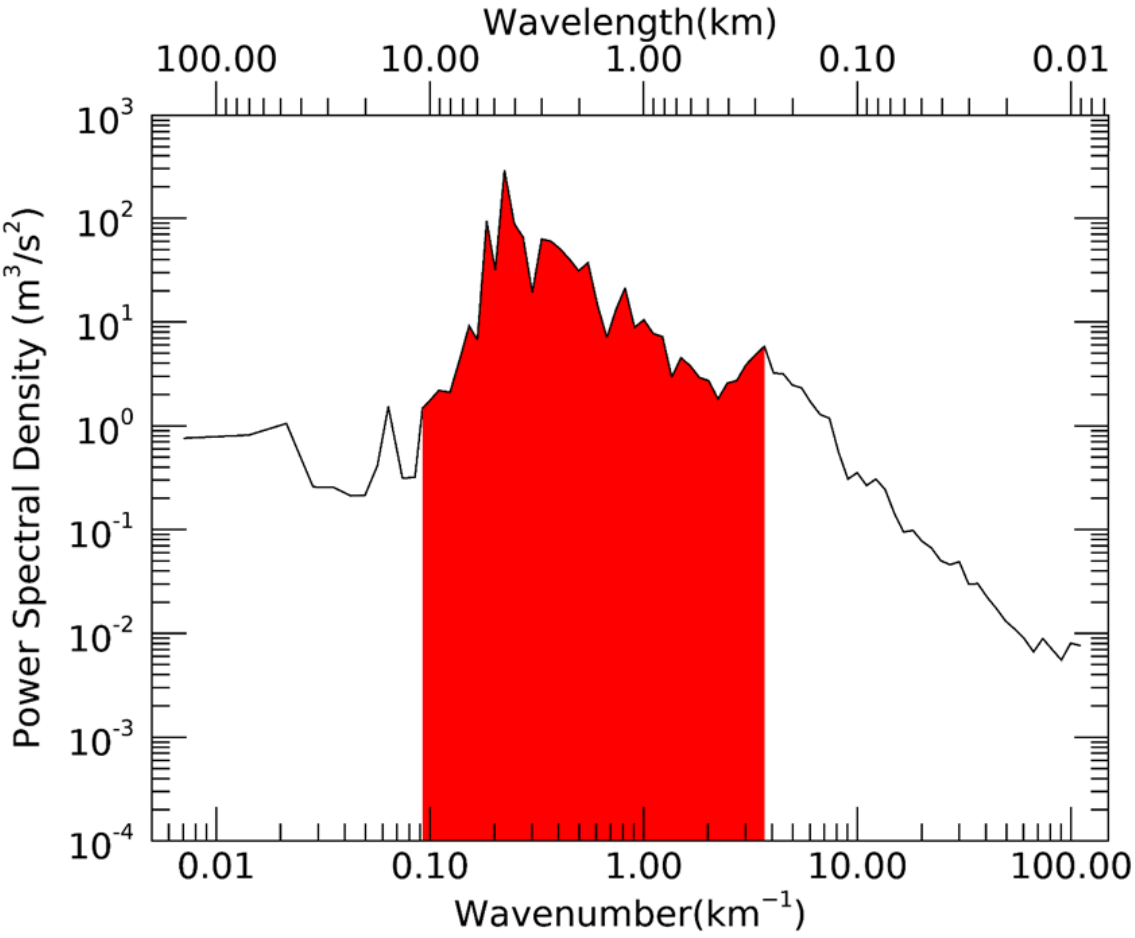

Figure 4.41: The PSD of vertical wind fluctuations, flight leg 1. The area representing the integral of the PSD across all coherent structure scales has been coloured red.

The coherent structure kinetic energy for flight leg 1 was 0.014 m^2/s^2 between the wavelength scales of approximately 250 m and 10 km. The coherent structure kinetic energy decreases when descending from the altitude of flight leg 8 (6.96 km) and the altitude of flight leg 1 (5.00 km).

4.3.2 - Momentum Fluxes

As the gravity waves propagate vertically they end up transporting horizontal momentum vertically. In this case momentum from the thunderstorm outflow is being transported vertically by the gravity waves. It should be noted that there is significant

uncertainty in the momentum fluxes since the fluctuations contain all resolved scales. Turbulence, Kelvin-Helmholtz waves and rolls will contribute to the momentum flux in addition to vertically propagating gravity waves. The vertical advection of horizontal shear will contribute to the momentum flux as well. These results will provide an estimate of the vertical flux of momentum that is caused by vertically propagating gravity waves. Figure 4.42 is the vertical profile of the vertical flux of zonal momentum in the environment of the mammatus clouds.

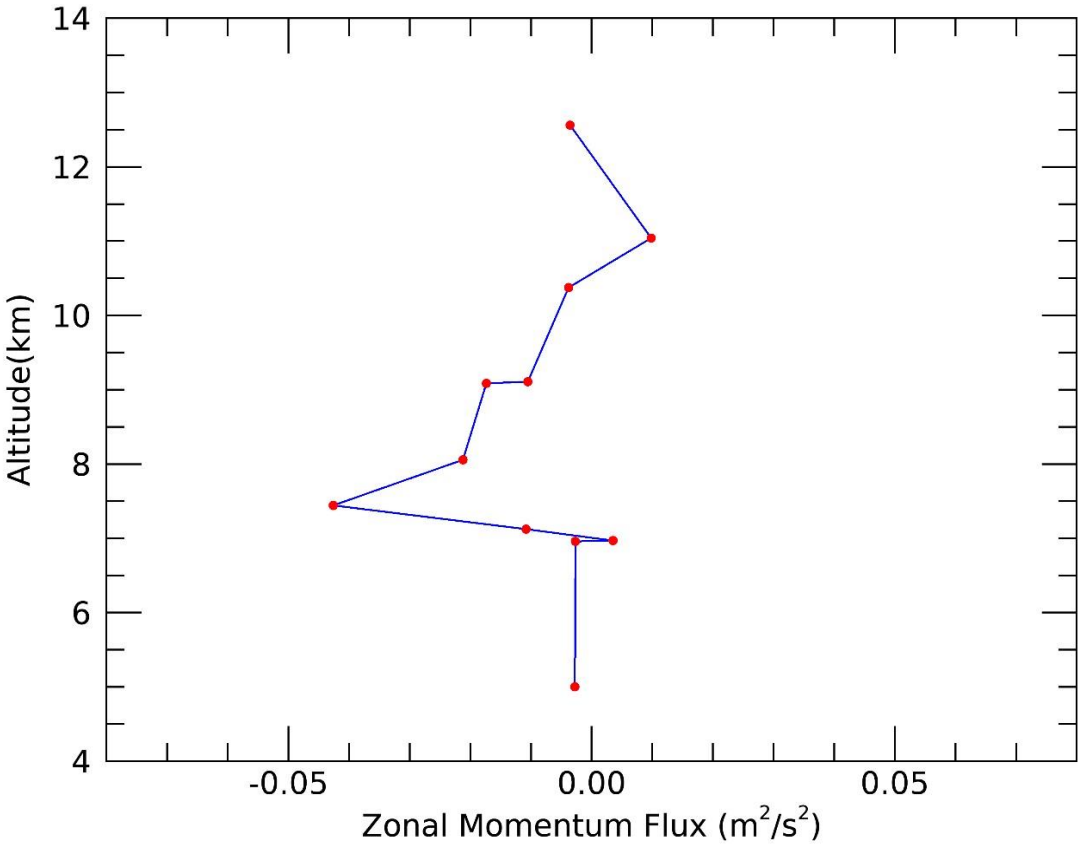

Figure 4.42: Vertical profile of the vertical flux of zonal momentum for all 11 flight legs on December 2nd, 2002.

The points at 5 km, 6.9 km and 7 km are treated as being effectively 0 due to the amount of uncertainty, there is essentially no zonal momentum flux occurring below 7 km. From an altitude of 7.4 km up to 10.5 km there is a negative momentum flux which corresponds to either an upward flux of westward momentum, or a downward flux of eastward momentum. Figure 4.43 is the vertical profile of the meridional momentum flux for the environment where the Mammatus clouds developed.

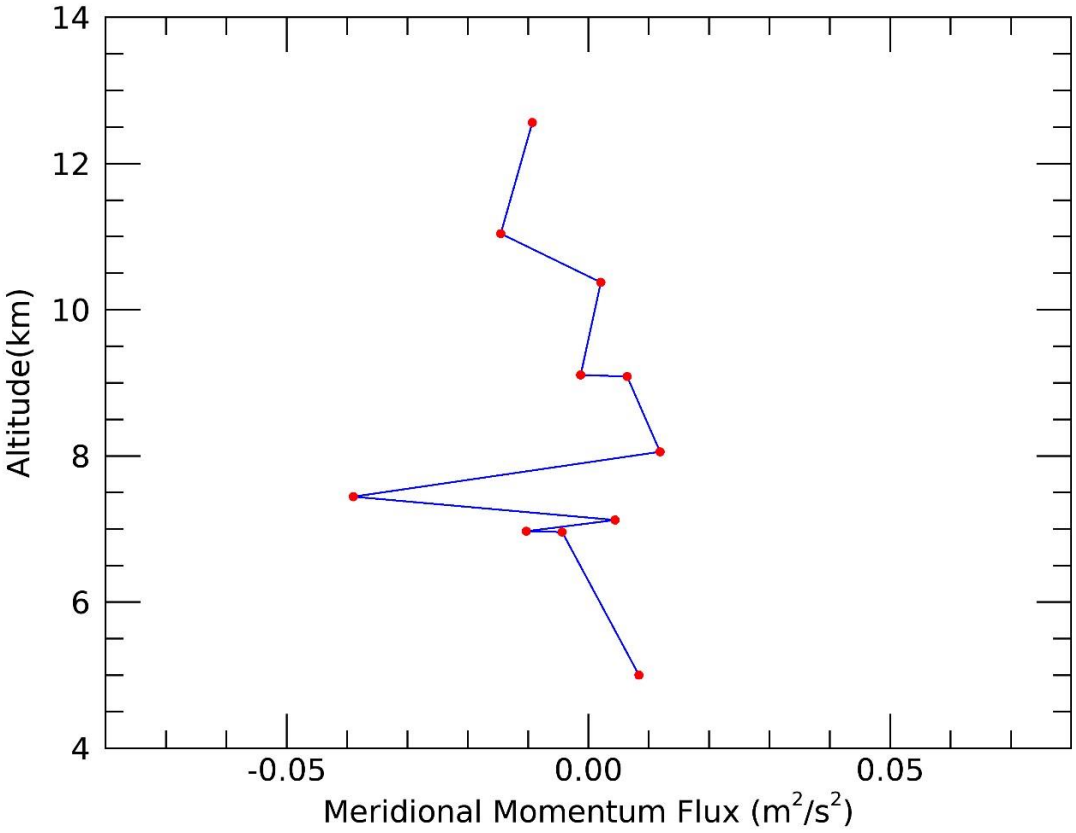

Figure 4.43: Vertical profile of the vertical flux of meridional momentum for all 11 flight legs on December 2nd, 2002.

The meridional momentum flux is essentially zero between the altitudes of 5 km and 7 km. The vertical motion of gravity waves in this part of the atmosphere is negligible. The meridional momentum flux is -0.039 m^2/s^2 at 7.4km and switches to 0.012 m^2/s^2 at the next

point above which is around 8.1 km. This means that gravity waves are generated at around 7km and propagate upwards and towards the south or they propagate downwards and towards the north. At 8.1 km the meridional momentum flux changed sign from negative to positive so gravity waves are propagating upwards and towards the north or downwards and towards the south. The meridional momentum flux is positive from an altitude of 8.1 km up to 9.11 km and then it is essentially 0 between the altitudes of 9.11 km and 10.47 km. Above 10.47 km the meridional momentum flux is negative. Overall the zonal and meridional momentum fluxes indicate that gravity waves are generated and confined between the altitudes of 7 km and 9.1 km.

4.3.3 - Scorer Parameter

The Scorer parameter is used to find where gravity waves could have been trapped or ducted. Figure 4.44 is the vertical profile of the squared Scorer parameter for the environment where the mammatus clouds developed. The Scorer parameter in the following figure is based on equation 2.29. In order to use that equation the phase speed of the wave (c) is needed. It was assumed that the waves were generated at the cloud base and the phase speed of the wave is equal to the average zonal wind speed at the altitude of the cloud base.

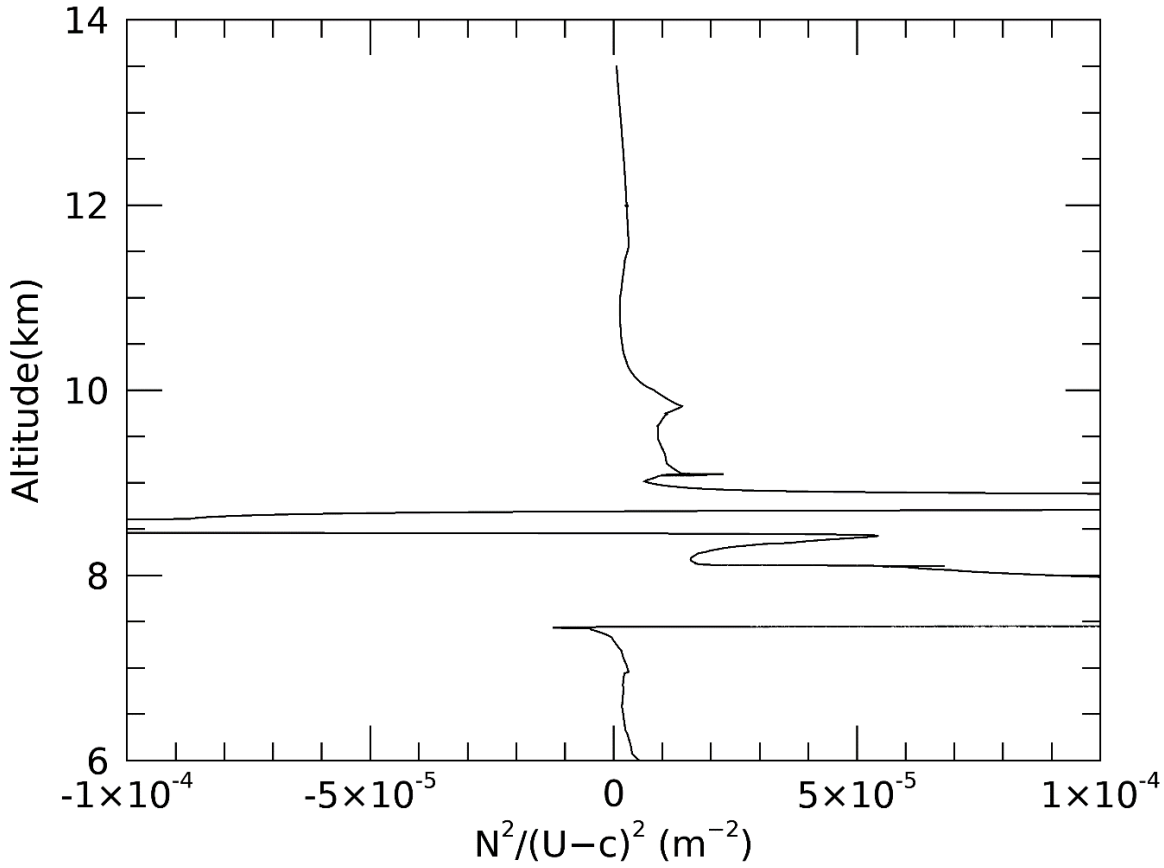

Figure 4.44: The vertical profile of the Scorer parameter squared for the environment in the anvil outflow region of the Hector thunderstorm based on the EMERALD-2 data from December 2nd, 2002 over Darwin Australia.

The results show that vertically propagating gravity waves with a phase speed equal to the wind speed at the cloud base could be trapped between heights around the cloud base in the height range between 7.45 km and 8 km where the Scorer parameter drops sharply with increasing or decreasing height. The spike in the Scorer parameter at 7.4 km is caused by the estimation of the phase speed of the wave. The zonal wind speed at an altitude of 7.4 km is very close to the phase speed estimation and the value of the Scorer parameter is large at this altitude.

The Scorer parameter can be analyzed using equation 2.30 to see if there is any consistency with the results in the previous figure. In this case the phase speed of the wave relative to the ground is assumed to be zero. If the results are consistent this would provide stronger evidence of a wave duct. Figure 4.45 is the vertical profile of the squared Scorer parameter when it is calculated using equation 2.30.

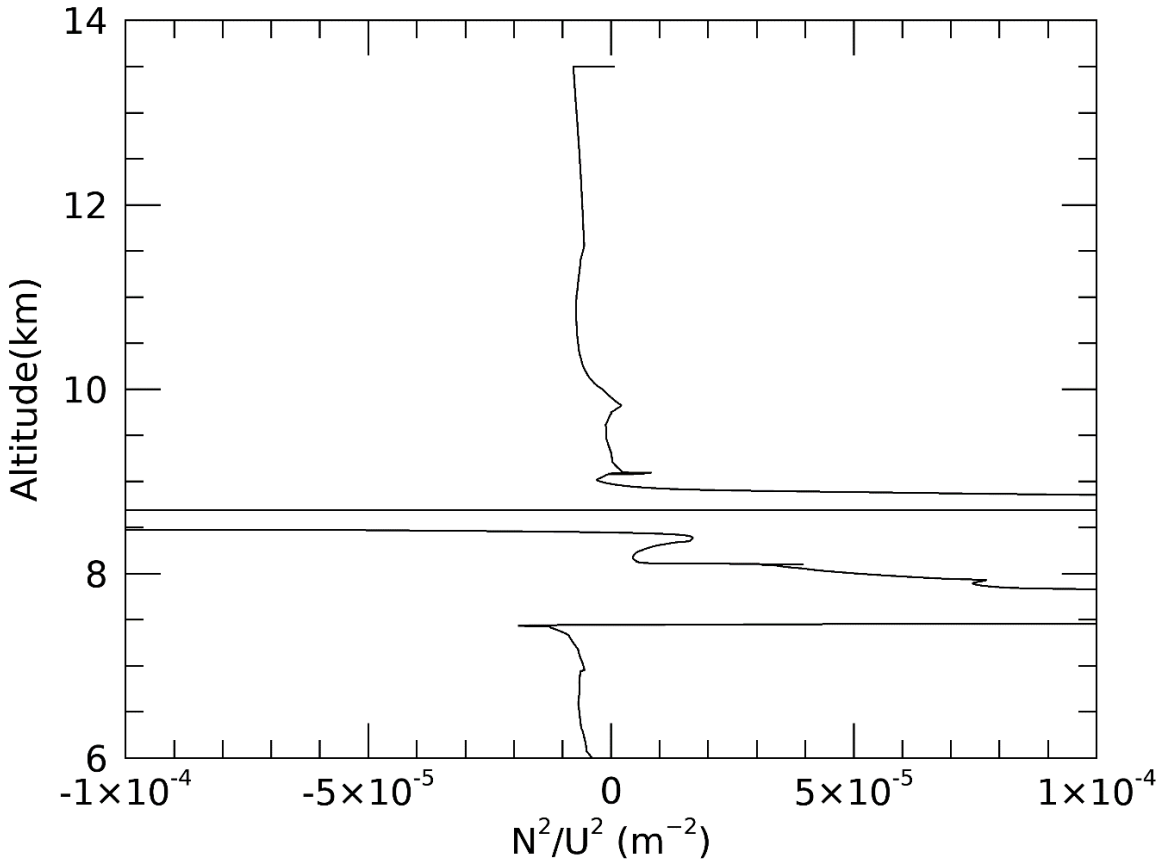

Figure 4.45: Vertical profile of the Scorer parameter squared using the approximation of N^2/U^2 where U is assumed to be the zonal wind speed.

The results in the figure show that vertically propagating gravity waves would be trapped just below an altitude of 8 km where the Scorer parameter is decreasing sharply with height. This is a good sign that there is a wave duct near the cloud base. Each

approximation of the Scorer parameter shows that the base of the Mammatus clouds sits in a gravity wave duct. Vertically propagating gravity waves become trapped at an altitude of approximately 8 km. This suggests that the base of the cloud is inside of a wave duct. These findings are based on the assumption that gravity waves are generated at the cloud base and the phase speed of these waves is equal to the zonal wind speed at the cloud base.

The results of the Scorer parameter show that vertically propagating gravity waves can be reflected close to the altitude of the cloud base and they are reflected again at some point above the cloud base. The Scorer parameter indicates reflecting layers at an altitude of 7.4 km and at an altitude of 8 km. Wave ducting and interference from gravity waves that propagate vertically can create standing gravity waves close to the base of the anvil cloud. Figure 4.46 is a schematic of the movement of gravity waves along the outflow of the thunderstorm.

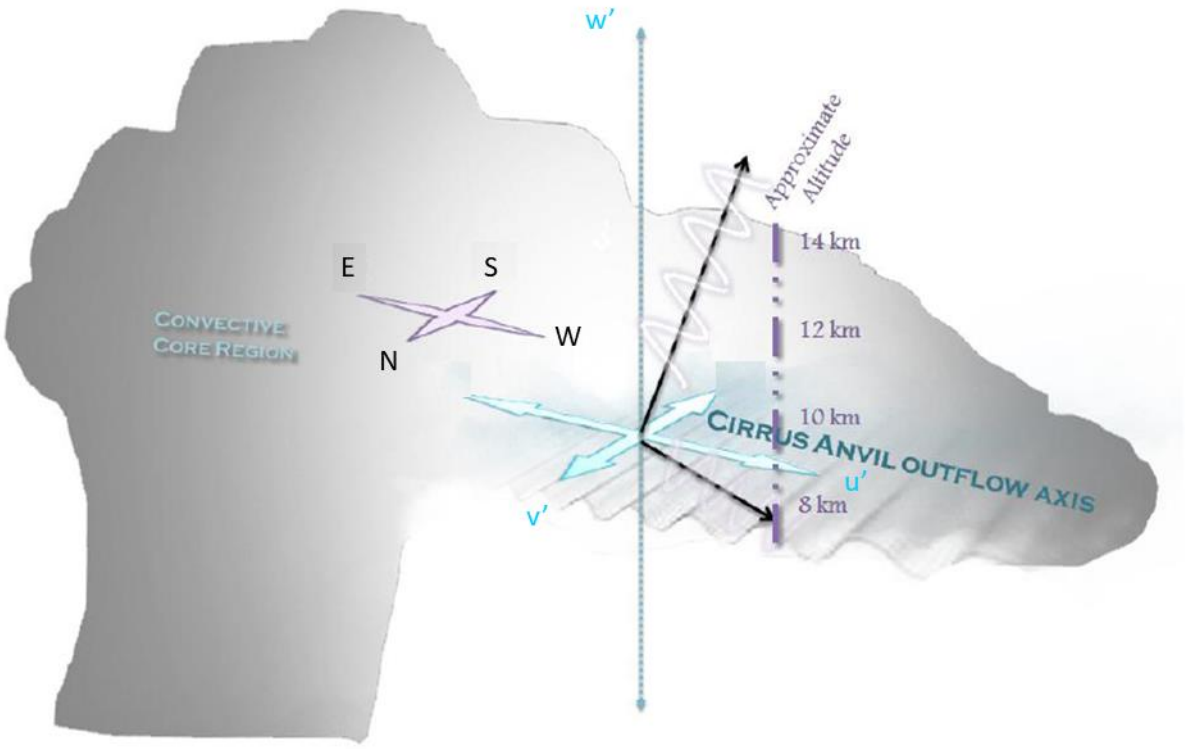

Figure 4.46: Vertical gravity waves propagating away from the cloud bases towards the west while standing gravity waves propagate horizontally along the bottom of the anvil cloud.

The results presented in figures 4.44 and 4.45 can be compared to the work of Trier and Sharman (2018). Vertical profiles of the Scorer parameter squared were created for a thunderstorm that had developed on 3-4 June, 2015 during the Plains Elevated Convection at Night (PECAN) field experiment in Kansas, United States. Two of the vertical profiles were created using data that came from the anvil outflow region of the thunderstorm. Figure 4.47 contains these vertical profiles for the Scorer parameter squared as well as the vertical profiles for horizontal wavenumber squared (k^2), Brunt-Väisälä frequency (N^2), and the wind speed in the direction of wave propagation (U). The data for figure 4.47(a) comes from the core of the anvil outflow region and the data for figure 4.47(b) comes from the edge of the anvil outflow region. This comparison will focus on the Scorer parameter squared and wave ducting in the anvil outflow region.

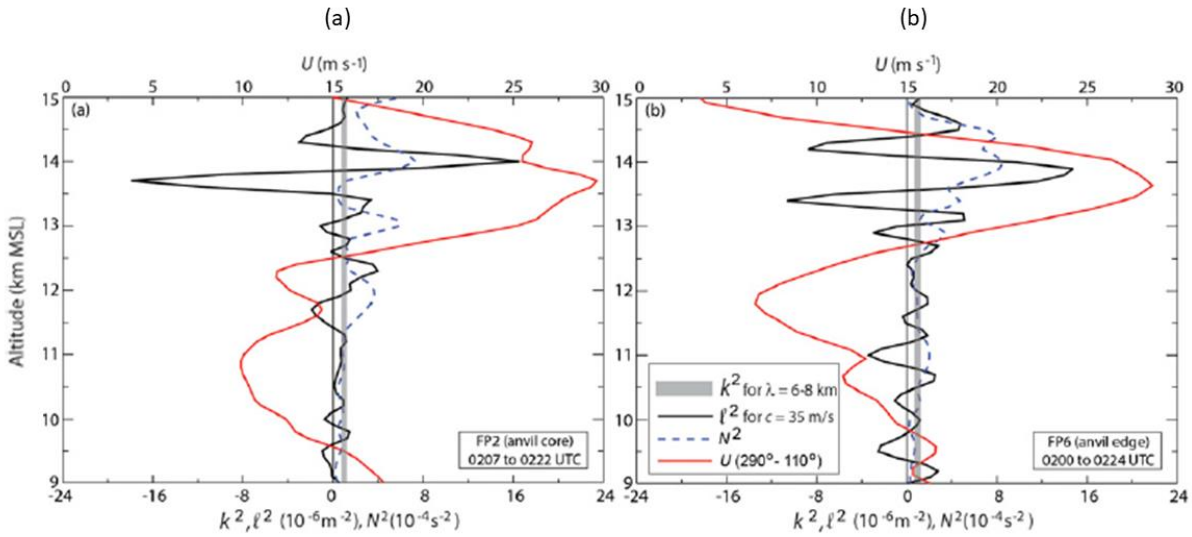

Figure 4.47: UTLS vertical profiles of the Scorer parameter squared (ℓ^2) using c = 35m/s, the Brunt-Väisälä frequency (N^2), and the horizontal wind (U) within the approximate plane of horizontal wave propagation from the (a) FP2 0130 UTC 4 Jun and (b) FP6 0130 UTC 4 Jun 2015 PECAN radiosonde launches. The gray shading in each panel indicates the square of the horizontal wavenumber for λ = 6-8 km waves. Vertical profiles that represent conditions close to (a) upwind deep convection in the anvil and (b) at the downstream anvil edge. Taken from Trier & Sharman, 2018.

It was found that the most significant wave ducting for the PECAN thunderstorm occurs in the upper part of the anvil cloud between the altitudes of 13.3 km and 14.5 km. At altitudes below 13 km the fluctuations in the Scorer parameter are smaller and the magnitude is closer to zero. This is different from what was observed during Hector. Most of the wave ducting occurred in the lower part of the anvil outflow at altitudes between 7.4 km and 9 km. At altitudes above 9 km the Scorer parameter was very close to 0. In both cases significant wave ducting occurs at altitudes where the wind shear is strong. In the case of the PECAN thunderstorm strong wave ducting began at altitudes that were below the jet stream maxima where the magnitude of the wind shear increases significantly with height (Trier & Sharman, 2018). The wave ducting that occurred in the anvil outflow of Hector was associated with an area where the zonal wind speed (figure 4.26) changed significantly with height. There is a local maximum in the wind shear at an altitude of 7.4 km (figure 4.28).

4.3.4 - Wave Breaking

The energy cascade which was discussed in section 2.5.2 demonstrates that energy breaks down from large scales into smaller scales until the energy completely dissipates. Typically energy is transferred from the background flow into gravity waves, then the gravity waves break down into turbulence and from there the turbulence dissipated into molecular diffusion. Atmospheric waves such as gravity waves and Kelvin-Helmholtz waves break and overturn before breaking down into turbulence. The turbulence that is generated by a breaking wave is strong enough to cause vertical mixing in the atmosphere (Whiteway et al., 2003; Whiteway et al., 2004b). The signal for a breaking gravity wave was observed in the vertical wind along flight leg 8 at 34 km into the flight. Figure 4.48 is a plot of the vertical wind fluctuations along flight leg 8. The wave that could be in the process of breaking has been outlined in the red box.

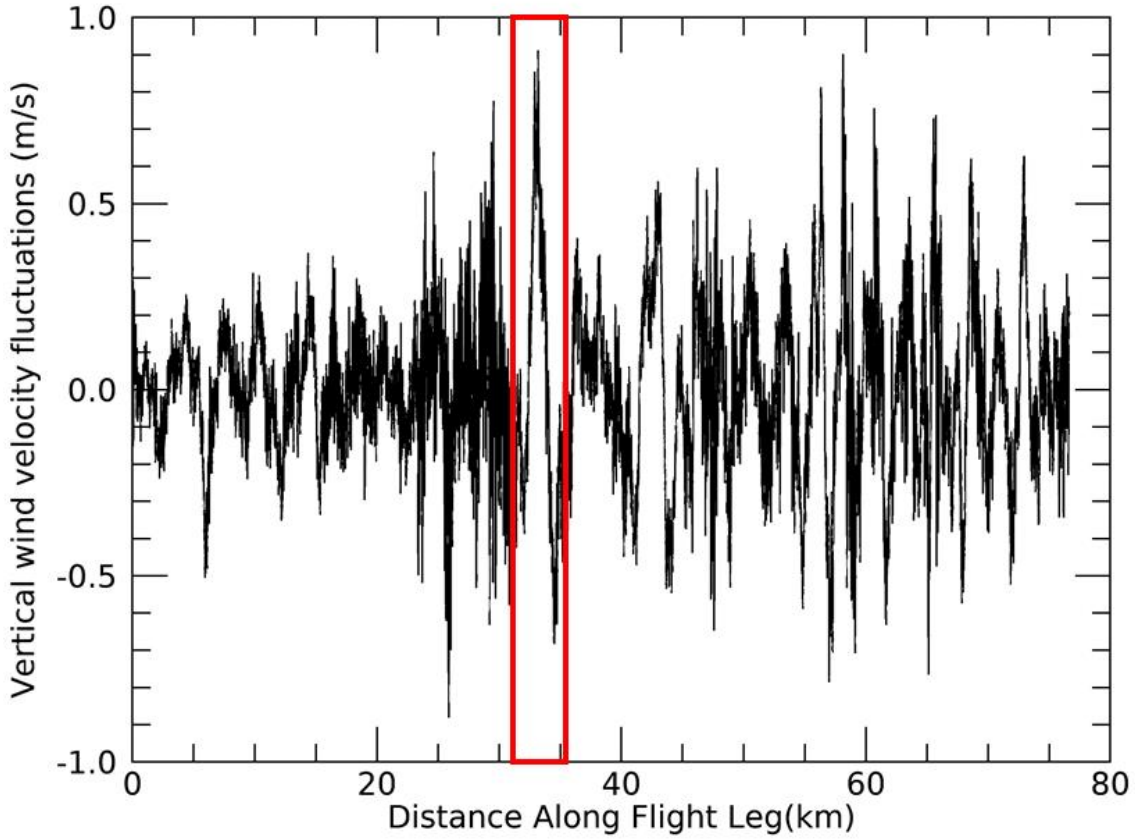

Figure 4.48: Vertical wind fluctuations plotted along flight leg 8, the breaking wave is outlined in the red box approximately 34 km into the flight.

Next it needs to be known if the wave is overturning. A wave is breaking and overturning if it is shown that the wave is inducing a convectively unstable temperature gradient. (Whiteway et al., 2003) The induced temperature gradient should be less than or equal to -9.8ºC/km. The breaking wave would induce a negative vertical potential temperature gradient. Figure 4.49 displays the vertical wind, vertical displacement, potential temperature and zonal wind in the location where the singular wave is located along flight leg 8. Vertical displacement was calculated by integrating vertical wind velocity in the

direction of the background wind. The background wind was blowing towards the west along the flight leg.

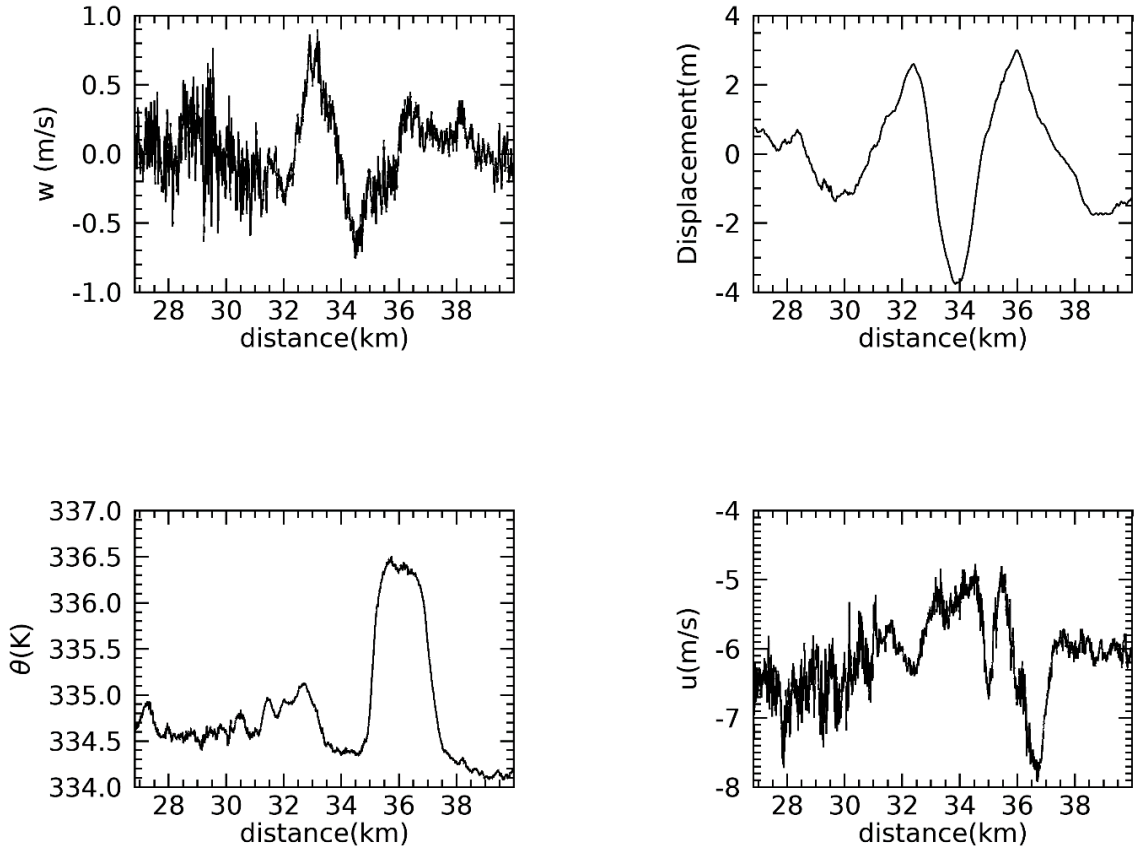

Figure 4.49: Vertical wind, vertical displacement, potential temperature and zonal wind in the vicinity of the breaking wave that was observed along flight leg 8.

The wave was observed along flight leg 8 between the 32.5 km and 36 km mark. The potential temperature decreased from about 335 K to 334.5 K from the 32 km to the 35 km mark. Once the air started to sink, potential temperature increased from 334.5 K to about 336.5 K this occurred between 35 km and 37.5 km into the flight. The results show that the wave is causing potential temperature to increase but there needs to be further analysis to figure out if the wave is inducing a convectively unstable temperature gradient.

Using the method from Whiteway et al. (2003) the lapse rate that is induced by the wave is given by the following equation

$$\Gamma_{ind} = \frac{A2\pi}{\lambda} \quad (4.1)$$

where *A* is the temperature perturbation amplitude, λ is the vertical wavelength. The vertical wavelength was determined by first calculating the vertical wavenumber with the following equation

$$m = -\frac{u'}{w'}k \quad (4.2)$$

where *m* is the vertical wavenumber, *k* is the horizontal wavenumber, *u'* is the zonal wind fluctuations and *w'* is the vertical wind fluctuations. The values for *w'* and *u'* were taken from the point where *w'* peaks due to the wave. The horizontal wavelength is 3.5 km so the corresponding horizontal wavenumber is 1.795 km^{-1}.

$$m = -\frac{0.91\ m/s}{0.80\ m/s}(1.795\ km^{-1}) = \text{-}2.042\ \text{km}^{-1}$$

The magnitude of the vertical wavenumber is 2.042 km^{-1} and the corresponding vertical wavelength is 3.077 km. Next, equation 4.1 was used to calculate the induced lapse rate. The temperature amplitude (A) is 1.00^{o}C and the vertical wavelength λ is 3.077 km.

$$\Gamma_{ind} = \frac{(1.00℃)2\pi}{3.077\ km} = 2.04℃/km$$

The maximum induced temperature gradient is -2.04^{o}C/km. The wave induced temperature gradient is added to the background temperature gradient to get the total temperature gradient that is caused by the wave. Figure 4.50 is the vertical profile of the background temperature in the vicinity of flight leg 8. The background temperature profile

comes from flight leg 1 where the Egrett is descending below the western edge of the anvil cloud.

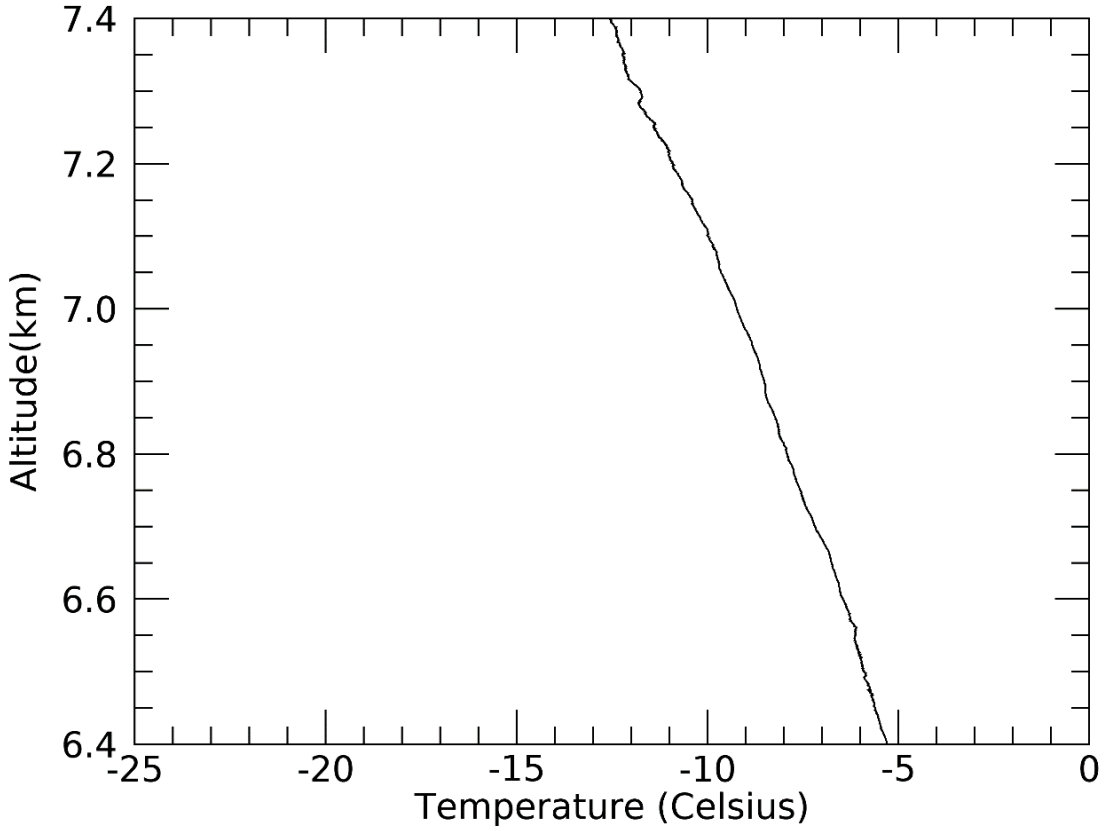

Figure 4.50: Vertical temperature profile in the neighbourhood of flight leg 8. The altitude of flight leg 8 is 6.96 km.

The average background temperature gradient is -5.8ºC/km at an altitude of 6.96 km so the overall induced temperature gradient is -7.84ºC/km. The temperature gradient would need to be -9.8ºC/km to satisfy the criteria for convective instability. At this point the wave is growing in amplitude and it has not yet reached the point where it will break and overturn.

The amplitude of a vertically propagating gravity wave grows exponentially with height. The amplitude grows according to the following equation which is based on the work of Campos (1983)

$$A = A_0 e^{\frac{z}{2L}} \text{ (4.3)}$$

where A_0 is the initial amplitude of the wave, *z* is the vertical distance that the wave has travelled, and *L* is the scale height for the earth's atmosphere which is approximately 8 km. The induced temperature gradient would need to be -4.0 ^{o}C/km (induced lapse rate of 4.0 ^{o}C/km) in order for the wave to induce a convectively unstable temperature gradient. First the new amplitude of the wave was determined by solving equation 4.1 for amplitude.

$$\frac{\Gamma_{ind}\lambda}{2\pi} = A \text{ (4.4)}$$

$$A = \frac{(4.00℃/km)(3.077km)}{2\pi} = 1.96℃$$

The vertical distance the wave had to travel to reach this amplitude was determined by solving equation 4.3 for *z*. 1.0^{o}C was the initial amplitude (A_0) in this case.

$$z = 2L \ln\left(\frac{A}{A_0}\right) \text{ (4.5)}$$

$$z = 2(8km) \ln\left(\frac{1.9589℃}{1.0℃}\right) = 10.76\text{km}$$

This particular gravity wave would have to travel upward for 10.76km to induce a convective unstable temperature gradient. Given that the wave was observed at an altitude of 6.96 km the wave would break at an altitude of 17.72km.

4.3.5 - Eddy Dissipation Rate Profile

The eddy dissipation rate describes how quickly energy is being dissipated from large scale eddies into smaller scale eddies. The eddy dissipation rate is used as a measure of the intensity of turbulence. Figure 4.51 is a vertical profile of the total eddy dissipation rate for each flight leg. The eddy dissipation rate has been plotted at the average height of the flight leg.

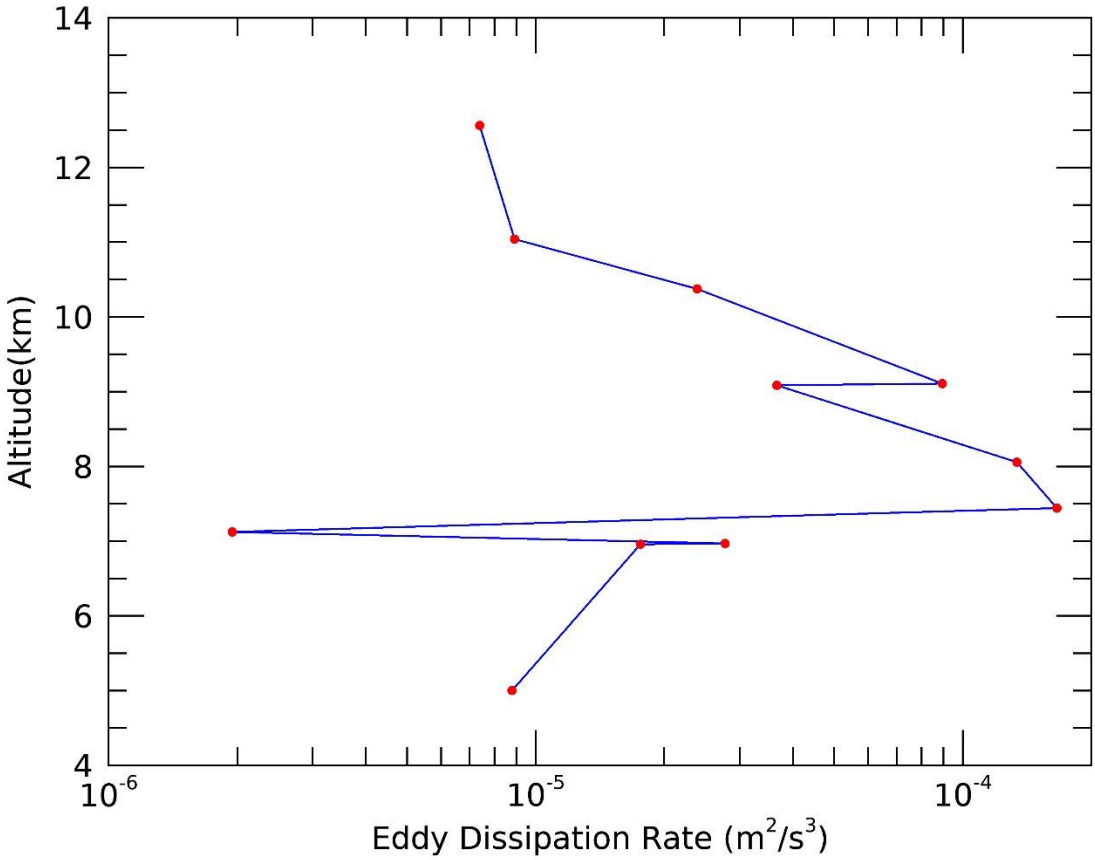

Figure 4.51: Vertical profile of eddy dissipation rate for all 11 flight legs on December 2nd, 2002.

The eddy dissipation rate is maximized right around the height of the height of the mammatus cloud base. The eddy dissipation rate is 1.8×10^{-4} m^2/s^3 at an altitude of 7.4 km. This means that the most intense turbulence in this anvil outflow was found at the altitude of the mammatus clouds. The turbulence is a reflection on the convective and shear instability that was found in the vicinity of the cloud base, based on the vertical profiles of temperature, potential temperature and equivalent potential temperature. The air at the base of the mammatus clouds is in constant fluctuation from turbulence and waves and this can allow mixing to occur between the dry sub cloud air and the saturated air in the anvil cloud.

4.4 - Mammatus Formation

In this section the results of the state of the atmosphere and the phenomena that are occurring are compared to the expected state of the atmosphere and phenomena in each of the mammatus cloud formation theories. There is a description of the established mammatus formation theories in section 2.7.

4.4.1 - Density Overhang

The EMERALD campaign differs from other studies in its unique capabilities to observe the vertical temperature profile and the cloud structure at the same time. This has allowed for the proposal of a new formation mechanism that is based on the potential temperature profile and LIDAR observations. It is known that in the environment of the anvil outflow there was a cloudy layer with cold potential temperatures on top of a layer of

dry air with relatively warm potential temperature. Cloudy air parcels that fall into the air below will continue to sink until they reach their level of neutral buoyancy.

Figure 4.52 (a) is the LIDAR signal plot for the mammatus clouds that were found along flight leg 5. Figure 4.52(b) is a vertical profile of the potential temperature and equivalent potential temperature in the vicinity of the mammatus clouds.

a)

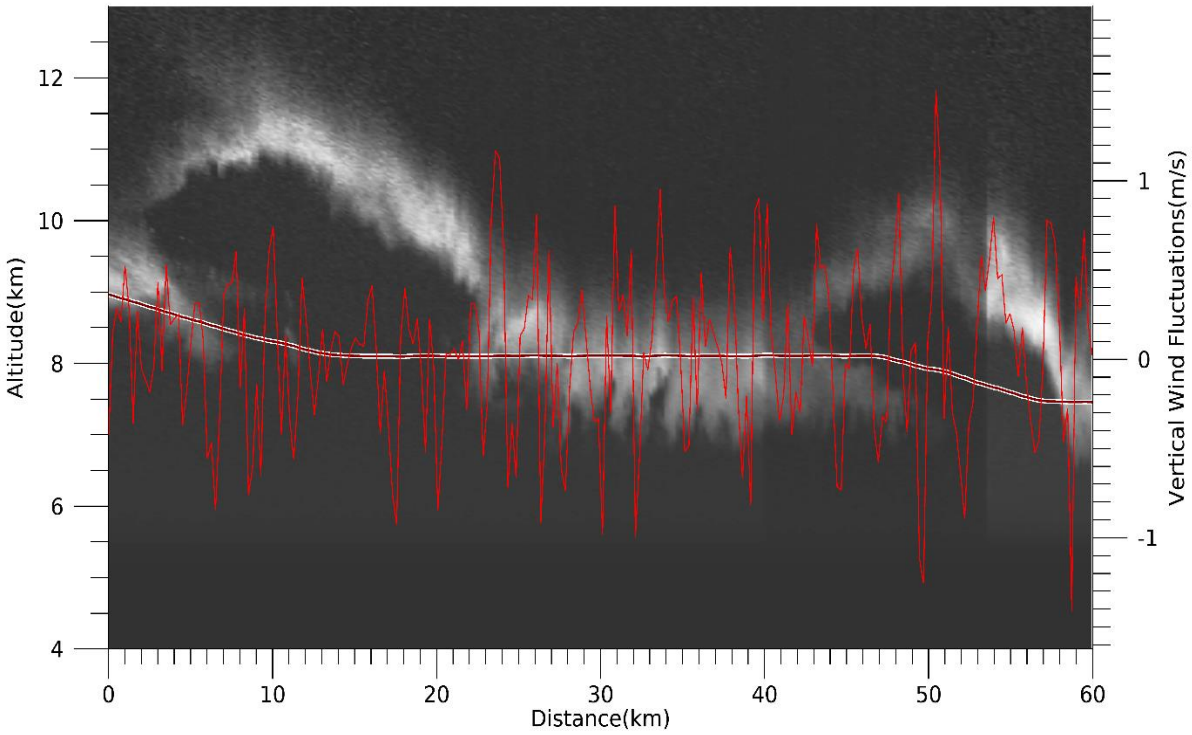

b)

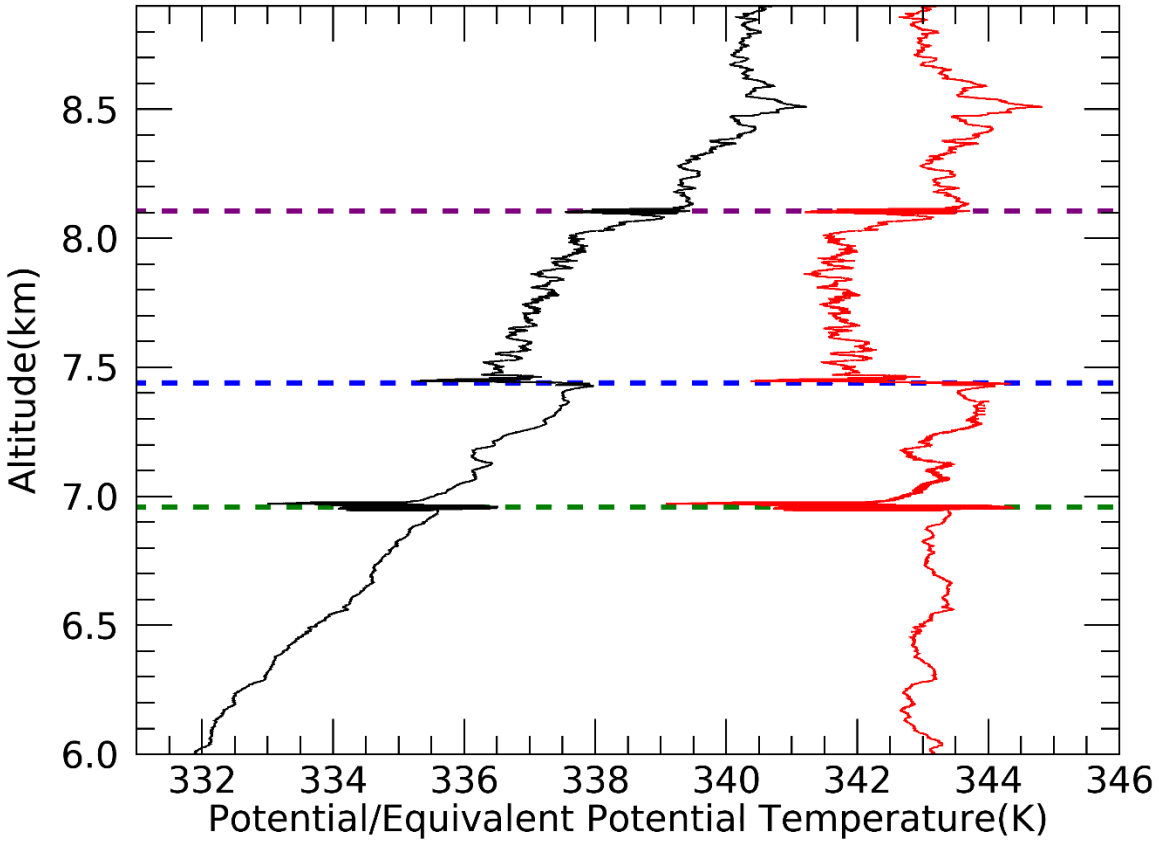

Figure 4.52: (a) The LIDAR for flight leg 5 with vertical wind fluctuations plotted on top of the LIDAR in red. The flight track has been plotted on top of the LIDAR in maroon. (b) Vertical potential temperature profile (black) and the vertical equivalent potential temperature profile (red). Flight leg 5 is represented by the purple dashed line, flight leg 6 is represented by the blue dashed line and flight legs 8 & 9 are represented by the green dashed line.

The vertical profiles of potential temperature and equivalent potential temperature exhibited similar behaviour at approximately 7.4 km. The average potential temperature that was observed at the cloud base matches the potential temperature that was observed close to 500 m below the base of the cloud. The minimum potential temperature that was observed at the cloud base matches the potential temperature about 550 m above the base of the cloud. Cloudy air parcels can fall below the cloud base until they reach the level of neutral buoyancy. The falling parcels of cloudy air are then capable of creating the lobes of the mammatus clouds.

4.4.2 - Evidence of Cloud Base Detrainment Instability

The relative humidity profile in section 4.2.2 shows there is a layer of dry air underneath the base of the anvil cloud. Relative humidity in this layer of air is about 30% right under the base of the mammatus clouds which is at a height of around 7.45 km. At altitudes that are higher than 7.45 km the air is saturated and relative humidity is approximately 100%. The potential temperature profile in section 4.2.1 has a local maximum of 339 K right at the cloud base and the potential temperature drops to 335 K through the base of the cloud. There is a layer of potentially cold and saturated air sitting on top of a potentially warm and dry sub-cloud layer. The atmosphere is unstable at the base of the anvil cloud.

There are a wide range of potential temperature values that are observed as the Egrett moves horizontally along the bottom of the mammatus clouds. This serves as evidence of vertical motion since it can be shown that the lowest potential temperature observed at the cloud base matches the potential temperature measured at an altitude below the cloud base, this suggests that air parcels moved up towards the base of the cloud which is at 7.45 km. The maximum potential temperature observed at the cloud base matches the potential temperature at an altitude above the cloud base which shows that air parcels moved down to the base of the cloud. The vertical motion that was observed may be due to waves or turbulence in the flow. It is known that the atmosphere is unstable, so the waves and turbulence may help to release some of the instability in the atmosphere. This appears to be an environment where cloud base detrainment instability is able to occur.

The criteria for cloud base detrainment instability can be quantified by calculating the liquid water static energy (equation 2.41) and deriving a vertical profile for the environment of

the anvil outflow. The conditions for cloud base detrainment instability have been satisfied if the liquid water static energy of the air under the cloud is higher than the liquid water static energy of the air inside of the cloud (Emanuel, 1981). For this case, ice static energy (equation 2.42) is used for the static energy of the environment in the vicinity of the anvil cloud. Figure 4.53 is the vertical profile of the ice static energy at the cloud base.

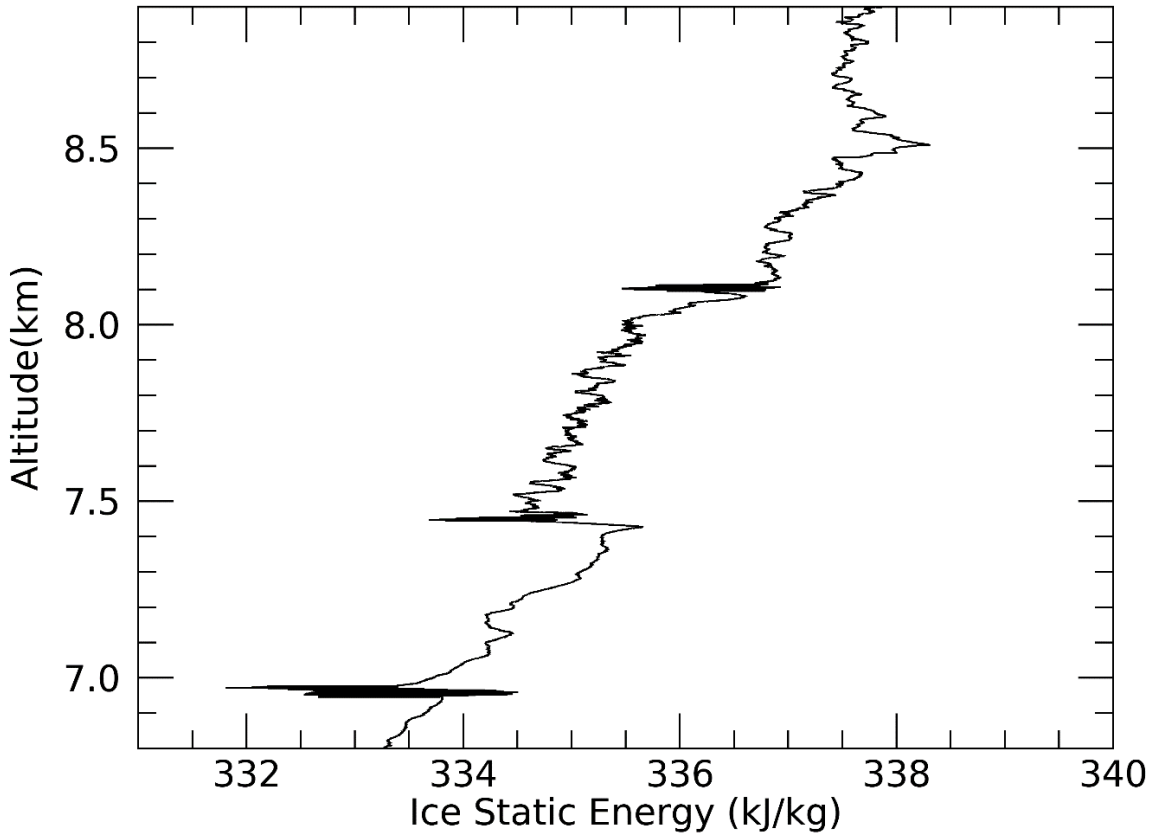

Figure 4.53: The vertical profile of ice static energy in the vicinity of the mammatus cloud base.

The ice water static energy is higher in the dry sub cloud air than it is in the saturated air that makes up the anvil cloud. The atmospheric conditions are favourable for

cloud base detrainment instability. Even though the conditions are favourable another phenomena is required for the cloudy air and the dry air to mix together.

This is where the gravity waves and Kelvin-Helmholtz waves play an important role. Gravity waves and Kelvin-Helmholtz waves have been considered a possible formation mechanism for mammatus clouds but it was noted that the mammatus lobes are usually not the same scale as the gravity waves (Kollias et al., 2005). Mammatus lobes can be roughly the same scale as Kelvin-Helmholtz waves but mammatus clouds often do not appear in long organized rows the same way billow clouds appear (Stull, 2020).

Gravity waves and Kelvin-Helmholtz waves break and overturn which generates intense turbulence in the environment (Whiteway et al., 2003; Whiteway et al., 2004b). This turbulence is able to cause mixing between the anvil cloud and the dry air below. Dry sub-cloud air mixes with the saturated air in the anvil cloud and some ice crystals in the air parcel sublimate. When the ice crystals sublimate latent heat is transferred from the air parcel to the ice crystals as they change state from solid ice to water vapour. Heat is taken away from the air molecules so the temperature of the air parcel decreases. The air parcel sinks because it is colder than its environment, it continues to sink until it reaches its level of neutral buoyancy. Some of the air may sink past the level of neutral buoyancy so it rises upwards around the edge of the mammatus cloud to create the round shape and the upward return flow that is observed.

4.4.3 – The Other Proposed Mechanisms

Cloud base detrainment instability is the most relevant formation mechanism that contributes to the formation of the mammatus clouds which were observed near Darwin, Australia on December 2nd, 2002. In order for cloud base detrainment instability to lead to mammatus clouds, sub cloud evaporation/sublimation must occur and there needs to be a mechanism that is able to produce mixing and overturning at the cloud base, this is able to occur with turbulence which can be generated by wind shear or convective instability. Coherent structures such as gravity waves and Kelvin-Helmholtz may play a role in the generation of turbulence. The anvil subsidence mechanism results in the generation of turbulence due to convection. Convection may occur in the vicinity of the cloud base when IR emissions are exchanged between the base of the anvil cloud and the surface.

Vertical wind measurements from the Egrett provide evidence of turbulence and coherent structures in the anvil outflow of the thunderstorm. This is supported by analyzing other quantities such as the coherent structure kinetic energy, momentum fluxes, and the Richardson number. In the vicinity of the cloud base the Richardson number was less than 0.25 and it was negative at an altitude of 7.42 km. Which shows that shear instability and convective instability is generating turbulence at the cloud base. Coherent structures such as gravity waves and Kelvin-Helmholtz waves can be generated in the shear layer and produce turbulence if they break and overturn in the vicinity of the cloud base. Convective instability occurs at the base of the anvil cloud. The potential temperature and equivalent potential temperature profiles suggests it is the result of the potentially cold anvil cloud being advected over the potentially warm sub-cloud air. It is unclear if radiative effects

caused any warming of the cloud base, this would require knowledge of the heating/cooling rate at the cloud base. It is also unclear if anvil subsidence played a role in the convective instability at the cloud base. A study on the anvil subsidence mechanism would require observations of a fixed point on the anvil cloud base.

Sublimation in the sub-cloud layer plays a role in the cloud base detrainment instability mechanism. The vertical profiles of relative humidity and water vapour mixing ratio show that the air underneath the anvil cloud is fairly dry. Relative humidity values in this air mass are between 7.1% and 63.6%. Ice crystals that fall into the sub-cloud layer will sublimate. The original sub-cloud sublimation theory states that hydrometeors would fall into the sub cloud air below but Emmanuel (1981) found that the evaporation/sublimation of falling hydrometeors would not cause enough latent cooling for mixed air parcels to sink. A large amount of ice crystals need to be mixed into the dry air and this will allow for more latent cooling in the mixed parcel which will sink and create a mammatus cloud.

There are a few mechanisms that do not seem to be possible based on the measurements. This includes Rayleigh-Taylor instability, Rayleigh-Bernard like convection, and the melting mechanism. The melting mechanism can only occur in an environment where the air temperature near the mammatus clouds is very close to $0^{o}C$ (Knight et al, 2004). Based on figure 4.18 the air temperature inside the mammatus clouds are between $-18.7^{o}C$ and $-12^{o}C$, this is significantly colder than $0^{o}C$ and no melting of ice crystals would be expected at these temperatures. This shows that the melting mechanism is not occurring in this case.

Rayleigh – Taylor instability is not possible because the atmosphere would need to have a lapse rate that is $32^{o}C/km$ or higher in the vicinity of the cloud base. The

hydrometeor mixing ratio would need to increase at a rate of 100 g kg^{-1} km^{-1}. Assuming the density of the air increases with height, these conditions would be necessary for the development of Rayleigh- Taylor instability at the base of the anvil cloud (Schultz et al, 2006). A lapse rate of 32^{o}C/km cannot occur in the free atmosphere since convection would occur automatically when the atmosphere becomes convectively unstable. The convection would cause the air to mix and this cause the atmosphere to maintain a lapse rate that is close to dry adiabatic (Rogers & Yau, 1989).

Finally, Rayleigh – Bernard like convection is not occurring since there are no results that show the cloudy air and the sub-cloud air are at the same temperature (Schaefer & Day, 1981). The vertical profiles for temperature, potential temperature and equivalent potential temperature show a strong temperature gradient at the cloud base (Figure 4.18- Figure 4.21).

Chapter 5: Summary & Conclusions

In-situ measurements of wind velocity, temperature, moisture and pressure were gathered on December 2nd, 2002 on research flights that originated from Darwin, Australia. The purpose of these research flights was to study the dynamics that occur inside of the anvil outflow region of tropical deep convection. These research flights were part of the EMERALD-2 research campaign which used two aircraft, the Egrett and the King Air to gather the data that was used in this thesis. The Egrett would gather the in-situ measurements while the King Air would fly about 5 km below the Egrett and gather LIDAR data that was used to map out the structure of the cloud. The deep convective event that was studied was a large thunderstorm that occurs regularly over the Tiwi Islands just off the coast of Darwin. Locals refer to the thunderstorm as Hector, it develops almost every day during the pre-monsoon season (November-December).

Mammatus clouds were observed along the base of the anvil cloud that was associated with the Hector thunderstorm. Measurements of temperature and moisture were combined with measurements of wind velocity in order to understand the state of the atmosphere and the dynamics that were present in the vicinity of the mammatus cloud. These findings were compared to mammatus cloud formation theories that had been previously established to see if the atmospheric conditions and dynamics in any of the theories matched the observations.

1). Observations of the vertical wind fluctuations and dissipation rate along each flight leg showed that there was light turbulent flow throughout the entire anvil outflow region. The dynamical structures that were observed in the anvil outflow include isotropic turbulence and coherent structures such as waves. It was noted that the highest dissipation rates in the outflow region were observed in the vicinity of the mammatus clouds.

2). The vertical profiles of temperature, potential temperature, equivalent potential temperature and moisture showed that there is a relatively cold and saturated layer of air sitting on top of a relatively warm and dry layer of air. The cold and saturated layer of air constitutes the anvil cloud while the warm and dry layer of air is the environment underneath the base of the cloud. The average values for potential temperature and equivalent potential temperature drop sharply with increasing altitude between the sub-cloud air and the anvil cloud. So the air underneath the cloud has a higher potential temperature than the air that is inside of the anvil cloud. At the cloud base the atmosphere is convectively unstable. The vertical profile of the zonal wind showed evidence of some notable wind shear close to the altitude of the cloud base. The Richardson number picked up on both the shear instability and convective instability that were present close to the base of the anvil cloud.

There is evidence that air is moving vertically between the anvil cloud and the dry air underneath. The potential temperature of the air inside of the anvil cloud was observed at the cloud base and the potential temperature of the air below the cloud base was observed at the altitude of the cloud base. This means that air inside the cloud is being moved down towards the cloud base and parcels of dry air are being moved up towards the bottom of anvil cloud. This vertical motion may be caused by the movement of air due to waves or it may be caused by turbulence.

3). Vertically propagating gravity waves are generated by the storm close to the base of the anvil cloud and they are confined between the altitudes of 7.4 km and 9.1 km. The vertical profiles of the coherent structure kinetic energy and eddy dissipation rate have relatively high values between 7.4 km and 9.1 km which would indicate an increase in the movement of waves and turbulence through that part of the anvil outflow. The Scorer parameter indicates there are

layers that reflect gravity waves at the altitudes of 7.4km and 8.0km. There is a gravity wave duct in between these two altitudes. The interference of vertically propagating gravity waves inside of the wave duct can create a standing gravity wave. This standing wave would be close to the altitude of the mammatus clouds. Some of the vertically propagating gravity waves break and start to overturn. One particular breaking wave was observed along flight leg 8. At the time the wave was analyzed it was not yet overturning. The amplitude of the wave would continue to grow until it reaches its critical level. At this point the wave will overturn and break down into turbulence that is strong enough to cause vertical mixing. Vertical mixing between the anvil cloud and the dry air underneath the cloud may be aiding the development of the mammatus clouds.

4). It was found that atmospheric conditions were suitable for cloud base detrainment instability. The average potential temperature is lower inside of the mammatus clouds than it is in the dry air below the cloud base. There is a layer of moist air with a lower potential temperature sitting on top of a layer of dry air with a higher potential temperature. In the vicinity of the cloud base it was found that the ice static energy of the sub-cloud air was higher than the ice static energy of the anvil cloud. These are the conditions for cloud base detrainment instability according to the theory.

Atmospheric conditions were favourable for cloud base detrainment instability but another mechanism is required in order to mix the cloudy air and the dry air underneath. Intense turbulence is able to generate vertical mixing between the anvil cloud and the sub-cloud air. Shear instability and convective instability were generated close to the base of the anvil cloud. This instability will lead to the development of turbulence in the lower part of the anvil outflow. In addition to this, a wave that is breaking and overturning will create turbulence. Dry air from

underneath the anvil cloud gets mixed into cloudy air parcels in the lower part of the cloud and some ice crystals sublimate. The temperature of the cloudy air parcel decreases because of the transfer of latent heat from the air molecules to the ice crystals as they change state from solid ice to water vapour. Heat is taken away from the air molecules so the temperature of the air parcel decreases. The cloudy air parcel sinks because it is colder than its environment. The cloudy air parcels that sink below the base of the anvil cloud form the lobes of the mammatus cloud.

5). A new mechanism may explain the formation of mammatus clouds in the anvil outflow of Hector. This mechanism is possible in an environment where the potential temperature of the anvil cloud is lower than the potential temperature of the air immediately underneath it. In this environment some air parcels at the bottom of the anvil cloud are at a lower potential temperature than their surrounding environment so they sink until they reach the point where the potential temperature of the parcel is equal to the potential temperature of the environment. The sinking parcels of cloudy air become the lobes of the mammatus cloud. This is essentially what happens with regular convection but in this case the air parcel is travelling downward instead of upward.

The results that were presented in this thesis offer a look into the way that mammatus clouds developed along the base of an anvil cloud. The combination of high frequency pressure, temperature, moisture, wind velocity, and LIDAR measurements of the cloud structure offered a unique perspective on the study of mammatus clouds. The results also provide more insight into the dynamics that are occurring inside of the anvil outflow of tropical thunderstorms such as Hector. There is room to expand this research into other convective events to see if there is any consistency in the way that mammatus clouds develop around the world. In addition to the

equipment that was used, cloud radar can be employed in future studies to get more information on the wind velocity and particle sizes throughout the anvil cloud.

References

Agee, E. M., (1975), Some inferences of eddy viscosity associated with instabilities in the atmosphere. *J. Atmos. Sci.,* **32,** 642–646.

Ahrens, C. D. (2009), *Meteorology today*. Belmont, CA: Brooks/Cole.

AMS. (2012), Liquid water static energy. Retrieved from https://glossary.ametsoc.org/wiki/Liquid_water_static_energy

Allaerts, Dries. (2016), Large-eddy Simulation of Wind Farms in Conventionally Neutral and Stable Atmospheric Boundary Layers.

Birner. (2010), Residual Circulation and Tropopause Structure. Journal of the Atmospheric Sciences, ***67***(8), 2582–2600. https://doi.org/10.1175/2010JAS3287.1

Bosart, L. F., and F. Sanders. (1991), An early-season coastal storm: Conceptual success and model failure. *Mon. Wea. Rev.,* **119,** 2831–2851.

Bridgman H.A. (1998), Australia: Climate and water resources. In: Encyclopedia of Hydrology and Lakes. Encyclopedia of Earth Science. Springer, Dordrecht. https://doi.org/10.1007/1-4020-4497-6_27

Brigham, E. Oran. (1988), The Fast Fourier Transform and its Applications. Prentice-Hall

Buck, A. L. (1981), New Equations for Computing Vapor Pressure and Enhancement Factor, *Journal of Applied Meteorology and Climatology*, ***20***(12), 1527-1532. Retrieved Dec 5, 2021, from https://journals.ametsoc.org/view/journals/apme/20/12/1520-0450_1981_020_1527_nefcvp_2_0_co_2.xml

Campos, L.M.B.C. (1983), On Three-Dimensional Acoustic Gravity Waves in Model Non-Isothermal Atmospheres. Wave Motion, **5**, 1-14. http://dx.doi.org/10.1016/0165-2125(83)900021

Carbone, Wilson, J. W., Keenan, T. D., & Hacker, J. M. (2000), Tropical island convection in the absence of significant topography. Part I: Life cycle of diurnally forced convection. *Monthly Weather Review*, ***128***(10), 3459–3480. https://doi.org/10.1175/1520-0493(2000)128<3459:TICITA>2.0.CO;2

Connolly, P., T. Choularton, M. Gallagher, K. Bower, M. Flynn, J. Whiteway. (2006), Cloud resolving simulations of intense tropical, hector thunderstorms: Implications for aerosol cloud interactions**.** *Quarterly Journal of the Royal Meteorological Society*, vol. 132, pages 3079 - 3106

Crawford, T.L., Dobosy, R.J. (1992), A sensitive fast-response probe to measure turbulence and heat flux from any airplane. *Boundary-Layer Meteorology* **59,** 257–278 https://doi.org/10.1007/BF00119816

Crawford, T., and R. Dobsy (1997), Pieces to a puzzle: air surface exchange and climate, *GPS World,* November.

Deardorff, J. W., (1980), Cloud top entrainment instability. *J. Atmos.Sci.,* **37,** 131–147.

Dobosy, R., Dumas, E. J., Senn, D. L., Baker, B., Sayres, D. S., Witinski, M. F., Healy, C., Munster, J., & Anderson, J. G. (2013), Calibration and Quality Assurance of an Airborne Turbulence Probe in an Aeronautical Wind Tunnel, *Journal of Atmospheric and Oceanic Technology*, ***30***(2), 182-196. Retrieved from, https://journals.ametsoc.org/view/journals/atot/30/2/jtech-d-11-00206_1.xml

Doering, Charles. (2020), Turning up the heat in turbulent thermal convection. Proceedings of the National Academy of Sciences. 117. 202004239. 10.1073/pnas.2004239117.

Doyle, Kate. (2019), Monsoon: The complex weather phenomenon that comes and goes. Retrieved from, https://www.abc.net.au/news/2019-01-18/monsoon-explaining-the-complex-weather-phenomenon/10722716

Emanuel, K. A., (1981), A similarity theory for unsaturated downdrafts within clouds. *J. Atmos. Sci.*, **38,** 1541–1557.

Emanuel, K. A., (1994), *Atmospheric Convection.* Oxford University Press, 580 pp.

Findeisen, W., (1940), Die Entstehung der 0°-Isothermie und die Fraktocumulus-Bildung unter Nimbostratus (The origin of 0°C isothermal layers and of fractocumulus beneath nimbostratus). *Meteor. Z.*, **57,** 49–54.

Frierson, D. M., Lu, J., & Chen, G. (2007), Width of the Hadley cell in simple and comprehensive general circulation models. *Geophysical Research Letters*, ***34***(18).

Garrett, T. J., and Coauthors, (2005), Evolution of a Florida cirrus anvil. *J. Atmos. Sci.*, **62,** 2352–2372.

Gasparini B., Blossey, P. N., Hartmann, D. L., Lin, G., & Fan, J. (2019), What drives the life cycle of tropical anvil clouds? *Journal of Advances in Modeling EarthSystems*, ***11***, 2586–2605. https://doi.org/10.1029/2019MS001736

Ghosh, D. (2021), Rayleigh-Taylor instability in geodynamics. Retrieved from https://blogs.egu.eu/divisions/gd/2021/02/17/rayleigh-taylor-instability-in-geodynamics/

Gossard, E. E., and W. B. Sweezy, (1974), Dispersion and spectra of gravity waves in the atmosphere. *J. Atmos. Sci.*, **31,** 1540–1548.

Hall, E. G., Jordan, A. F., Hurst, D. F., Oltmans, S. J., Vömel, H., Kühnreich, B., & Ebert, V. (2016), Advancements, measurement uncertainties, and recent comparisons of the NOAA frost point hygrometer. Atmospheric measurement techniques, ***9***(9), 4295–4310. https://doi.org/10.5194/amt-9-4295-2016

Hartmann, D.L (2007), The Atmospheric General Circulation and Its Variability, Journal of the Meteorological Society of Japan. Ser. II, 2007, Volume 85B, Pages 123-143, Released October 26, 2007, https://doi.org/10.2151/jmsj.85B.123, https://www.jstage.jst.go.jp/article/jmsj/85B/0/85B_0_123/_article/-char/en,

Hines, C. O. (1971), Generalizations of the Richardson criterion for the onset of atmospheric turbulence. *Quarterly Journal of the Royal Meteorological Society*, ***97***(414), 429–439. https://doi.org/10.1002/qj.49709741405

Hlad, C. J., Jr., (1944), Stability-tendency and mammatocumulus clouds. *Bull. Amer. Meteor. Soc.*, **25,** 327–331.

Jo, I., B. A. Albrecht, and P. Kollias, (2003), 94-GHz Doppler radar observations of mammatus in tropical anvils during CRYSTAL-FACE. Preprints, *31st Int. Conf. on Radar Meteorology*, Seattle, WA, Amer. Meteor. Soc., 197–199.

Kain, J. S., S. M. Goss, and M. E. Baldwin, (2000), The melting effect as a factor in precipitation-type forecasting. *Wea. Forecasting*,**15,** 700–714.

Kanak, Katharine M, et al. (2008), Numerical Simulation of Mammatus. *Journal of the Atmospheric Sciences*, vol. 65, no. 5, 2008, pp. 1606–1621., https://doi.org/10.1175/2007JAS2469.1.

Keenan T.D., Morton B.R., Zhang X.S. and K. Nyguen, (1990), Some characteristics of thunderstorms over Bathurst and Melville Islands near Darwin, Australia. *Quarterly Journal of the Royal Meteorological Society* **116,** 1153–1172

Keshtgar, B., Alizadeh-Choobari, O. & Irannejad, P. (2020), Seasonal and interannual variations of the intertropical convergence zone over the Indian Ocean based on an energetic perspective. *Clim Dyn* **54,** 3627–3639, https://doi.org/10.1007/s00382-020-05195-5

Knight, C. A., L. J. Miller, and W. D. Hall, (2004), Deep convection and "first echoes" within anvil precipitation. *Mon. Wea. Rev.*,**132,** 1877–1890.

Kollias, P., I. Jo, and B. A. Albrecht, (2005), High-resolution observations of mammatus in tropical anvils. *Mon. Wea. Rev.*,**133,** 2105–2112.

Kolmogorov, A. N. (1941), The local structure of turbulence in incompressible viscous fluid for very large Reynolds numbers. Dokl. Akad. Nauk SSSR **30**, 301-305, 1941.

Korotcenkov. (2018), Handbook of Humidity Measurement, Volume 1: Spectroscopic Methods of Humidity Measurement. CRC Press. https://doi.org/10.1201/b22369

Krider, P.E. (1998), Thunderstorm. *Britannica Encyclopedia*. Retrieved from, https://www.britannica.com/science/thunderstorm

Kuttippurath, Jayanarayanan, (2005), Study of stratospheric composition using airborne submillimeter radiometry and a chemical transport model. http://elib.suub.uni-bremen.de/diss/docs/E-Diss1362_jaythes_suub.pdf.

Lane, T.P and R.D. Sharman, (2014), Intensity of thunderstorm-generated turbulence as revealed by large-eddy simulation. Geophys. Res. Lett., **41**, 2221–2227, https://doi.org/10.1002/2014GL059299.

Lederman, Jerusha Isabel., (2015), "Dynamics in the Anvil Outflow of Tropical Convection."

Letzmann, J., (1930), Cumulus-Pulsationen (Cumulus pulsations).*Meteor. Z.*, **47,** 236–238.

Levya, S. (nd), Atmospheric Circulation. *The Geophile Pages*. Retrieved from: http://geophile.net/Lessons/atmosphere/atm_circulation_04.html#

Lilly, D. (1983), Stratified turbulence and the mesoscale variability of the atmosphere. *J. Atmos. Sci.*, **40**, 749-761.

Lilly, D. K., (1988), Cirrus outflow dynamics. *J. Atmos. Sci.,* **45,**1594–1605.

Ludlam, F. H., (1948), The forms of ice clouds. *Quart. J. Roy. Meteor.Soc.,* **74,** 39–56.

Ludlam F.H and R. S. Scorer, (1953), Convection in the atmosphere. *Quart. J. Roy. Meteor. Soc.,* **79,** 317–341.

Maccready, P.B. (1953), Structure of Atmospheric Turbulence. *Journal of Meteorology*, ***10***, 434-449.

Markowski. (2007), An Overview of Atmospheric Convection. In *Atmospheric Convection: Research and Operational Forecasting Aspects* (pp. 1–6). Springer Vienna. https://doi.org/10.1007/978-3-211-69291-2_1

Martner, B. E., (1995), Doppler radar observations of mammatus. *Mon. Wea. Rev.*, **123,** 3115–3121.

Nappo. (2013), An introduction to atmospheric gravity waves (2nd ed.). Academic Press/Elsevier.

Nugent, A. DeCou, D, (2019). Atmospheric Science. University of Hawai'i at Manoa.

Pandya, R. E., and D. R. Durran, (1996), The influence of convectively generated thermal forcing on the mesoscale circulation around squall lines. *J. Atmos. Sci.,* **53,** 2924–2951.

Petre, J. M., and J. Verlinde, (2004), Cloud radar observations of Kelvin–Helmholtz instability in a Florida anvil. *Mon. Wea. Rev.,* **132,** 2520–2523.

Plank, V. G., D. Atlas, and W. H. Paulsen, (1955), The nature and detectability of clouds and precipitation as determined by 1.25-centimeter radar. *J. Meteor.,* **12,** 358–378.

Platt, C. M. R., R. T. Austin, S. A. Young, and A. J. Heymsfield, (2002), LIRAD observations of tropical cirrus clouds in MCTEX. Part II: Optical properties and base cooling in dissipating storm anvil clouds. *J. Atmos. Sci.,* **59,** 3163–3177.

Rafiq, S., Pattiaratchi, C., & Janeković, I. (2020), Dynamics of the Land–Sea Breeze System and the Surface Current Response in South-West Australia. *Journal of Marine Science and Engineering*, ***8***(11), 931. MDPI AG. Retrieved from http://dx.doi.org/10.3390/jmse8110931

Randall, D. A., (1980), Conditional instability of the first kind upside-down. *J. Atmos. Sci.,* **37,** 125–130.

Rogers, R.R., Yau, M. K (1989), A Short Course in Cloud Physics (3rd ed). Elsevier Science

Schaefer, V. J., and Day, J. A., (1981), A Field Guide to the Atmosphere. Houghton Mifflin Co., 359 pp.

Schultz, Kanak, K. M., Lilly, D. K., Straka, J. M., Trapp, R. J., Gordon, B. A., Zrnic, D. S., Bryan, G. H., Durant, A. J., Garrett, T. J., & Klein, P. M. (2006), The mysteries of mammatus clouds : Observations and formation mechanisms. *Journal of the Atmospheric Sciences*, ***63***(10), 2409–2435. https://doi.org/10.1175/JAS3758.1

Scorer. (1949), Theory of waves in the lee of mountains. *Quarterly Journal of the Royal Meteorological Society*, ***75***(323), 41–56. https://doi.org/10.1002/qj.49707532308

Scorer, R. S., (1958), The dynamics of mamma. *Sci. Prog.*, **46,** 75–82.

Scorer, R. S., (1972), *Clouds of the World.* Stackpole Books, 176 pp.

Sinha, N. (2013), Towards RANS Parameterization of Vertical Mixing by Langmuir Turbulence in Shallow Coastal Shelves. ProQuest Dissertations Publishing.

Stewart, R. E., (1984), Deep 0°C isothermal layers within precipitation bands over southern Ontario. *J. Geophys. Res.*, **89,** 2567–2572.

Stull, R. (2016), Practical Meteorology an Algebra Based Survey of Atmospheric Science. AVP International, University of British Columbia.

Stull, R. (2020), Special Clouds > Billow Clouds. UBC ATSC 113 Weather for Sailing, Flying and Snow Sports. Retrieved from: https://www.eoas.ubc.ca/courses/atsc113/flying/met_concepts/01-met_concepts/01b-special-clouds/billow.html

Tennekes, & Lumley, J. L. (1972), A first course in turbulence. MIT Press.

Trier, S. B., Sharman, R. D., Fovell, R. G., & Frehlich, R. G. (2010), Numerical Simulation of Radial Cloud Bands within the Upper-Level Outflow of an Observed Mesoscale Convective System, *Journal of the Atmospheric Sciences*, *67*(9), 2990-2999. Retrieved Mar 4, 2022, from https://journals.ametsoc.org/view/journals/atsc/67/9/2010jas3531.

Trier, S. B., & Sharman, R. D. (2018), Trapped Gravity Waves and Their Association with Turbulence in a Large Thunderstorm Anvil during PECAN, *Monthly Weather Review*, ***146***(9), 3031-3052.

Troeger, H. (1922), Die Häufigkeit der Mammatus-Formen (The frequency of the mammatus). Meteor. Z., **39**, 122–123.

Wagner, F., (1948), Mammatusform als Anzeichen für Absinkbewegung in Wolkenluft (The shape of mammatus as an indicator for subsidence in cloudy air). Ann. Meteor., **1,** 336–340.

Whiteway, J.A., (1999), Enhanced and inhibited gravity wave spectra. Journal of the Atmospheric Sciences, **56**(10), 1344–1352.

Whiteway, J. & Pavelin, Edward & Busen, Reinhold & Hacker, Jorg & Vosper, Simon. (2003), Airborne Measurements of Gravity Wave Breaking at the Tropopause. Geophysical Research Letters. 30. ASC11-1. 10.1029/2003GL018207.

Whiteway, J et al., (2004a), Anatomy of cirrus clouds: Results from the Emerald airborne campaigns, Geophys. Res. Lett.,31, L24102, doi:10.1029/2004GL021201.

Whiteway, J. A., G. P. Klaassen, N. G. Bradshaw, and J. Hacker (2004b), Transition to Turbulence in Shear above the Tropopause, Geophys. Res. Lett., 31, L02118, doi:10.1029/2003GL018509.

Wiederhold. (1997), Water Vapor Measurement: Methods and Instrumentation. Taylor & Francis Group.

Wood, R. (2012), Stratocumulus Clouds, *Monthly Weather Review*, ***140***(8), 2373-2423.

WMO (1957), Definition of the tropopause, WMO Bull., **6**, 136.

Wroblewski, D. E., Coté, O. R., Hacker, J. M., & Dobosy, R. J. (2010), Velocity and Temperature Structure Functions in the Upper Troposphere and Lower Stratosphere from High-Resolution Aircraft Measurements, Journal of the Atmospheric Sciences, ***67***(4), 1157-1170. Retrieved Jan 21, 2022, from https://journals-ametsoc-org.ezproxy.library.yorku.ca/view/journals/atsc/67/4/2009jas3108.

Wüst, S., Bittner, M., Yee, J.-H., Mlynczak, M. G., & Russell III, J. M. (2017), Variability of the Brunt–Väisälä frequency at the OH layer height. *Atmospheric Measurement Techniques*, ***10***(12), 4895–4903. https://doi.org/10.5194/amt-10-4895-2017

Yang, M.-J., and R. A. Houze Jr., (1995), Multicell squall-line structure as a manifestation of vertically trapped gravity waves. *Mon. Wea. Rev.*, **123,** 641–661.